0 0 0 0 4 7 0 2 3 4 1

LBL-5763
c.1

SINTERING OF Al_2O_3 POWDER COMPACT BY HOT STAGE SCANNING ELECTRON MICROSCOPY

David Nin-Kuo Wang
(Ph. D. thesis)

December 1976

Prepared for the U. S. Energy Research and Development Administration under Contract W-7405-ENG-48

For Reference

Not to be taken from this room

LAWRENCE BERKELEY LABORATORY
UNIVERSITY OF CALIFORNIA
BERKELEY

LBL-5763
c.1

LEGAL NOTICE

This report was prepared as an account of work sponsored by the United States Government. Neither the United States nor the United States Energy Research and Development Administration, nor any of their employees, nor any of their contractors, subcontractors, or their employees, makes any warranty, express or implied, or assumes any legal liability or responsibility for the accuracy, completeness or usefulness of any information, apparatus, product or process disclosed, or represents that its use would not infringe privately owned rights.

0 0 0 0 4 7 0 0 2 3 5 2

SINTERING OF Al_2O_3 POWDER COMPACT BY HOT STAGE SCANNING ELECTRON MICROSCOPY

Contents

ABSTRACT

I. Introduction 1

II. Experimental 12

A. Apparatus 12

1. Hot Stage Scanning Electron Microscope 12

2. Temperature Calibration Device 14

B. Material and Sample Preparation 19

C. Shrinkage Measurements 21

D. Microstructure Study 25

1. Sample Preparation 25

2. Polishing and Etching 25

3. Photography 26

4. Grain Size Measurement 26

III. Results and Discussion 28

A. Description of the Green State 28

B. Initial Stage Sintering 44

C. Post Initial Stage Sintering 62

1. Densification Kinetics 62

2. Grain Growth Kinetics 91

3. Correlation 116

IV. Conclusions 132

Acknowledgment

References

0 0 0 0 0 1 4 7 0 0 1 2 5 5 6 3

SINTERING OF Al_2O_3 POWDER COMPACT BY HOT STAGE SCANNING ELECTRON MICROSCOPY

David Nin-Kuo Wang

Materials and Molecular Research Division, Lawrence Berkeley Laboratory
and Department of Materials Science and Engineering
University of California, Berkeley, California 94720

ABSTRACT

Previous sintering studies on Al_2O_3 powder compacts have concentrated on the use of isothermal techniques. A complete analysis of sintering kinetics is unattainable due to uncertainties involved in the initial heating period. This work has used a constant heating rate technique to study MgO-doped and undoped Al_2O_3 powder compacts with variations in green density. Hot stage scanning electron microscopy was used to monitor continuously the linear dimensional change of a powder compact throughout the densification process at various constant heating rates.

Extensive studies on the microstructural evolution were made and correlated with the densification and grain growth kinetics. The maximum densification rate was found to occur at a critical density which was independent of the heating rate as long as the green density remained constant. Microstructural evolution has been correlated with the densification rate to explain the occurrence of the maximum rate of densification. The effect of MgO dopant on the densification and grain growth of Al_2O_3 compacts was also studied. It was found that there is no effect of MgO dopant on either process until the critical density is reached. Before the attainment of the critical density, the grain

growth kinetics is characterized by grain boundary self-diffusion. After the critical density, the densification kinetics and grain growth kinetics are inter-dependent and characterized by the same activation energy. The grain growth rate is limited by the pore phase and obeys Zener's criterion.

In accordance with the porosity changes, the sintering process can be divided into four stages.

0 0 0 0 0 4 7 0 2 3 7 4

I. INTRODUCTION

The sintering of powder compacts is an important processing step in the production of ceramic materials. Solid state sintering, in particular, is characterized by having no liquid phase present during the heat treatment. During the sintering process, mass transport occurs when the compact is heated to a suitable temperature below the melting point. The compact shrinks, and much of the void volume, which had resulted from the initial misfit of the powder particles, is eliminated.

According to sintering models, the microstructural evolution during the sintering process has generally been divided into three stages. The initial stage of sintering can be defined as the interval from the beginning of the heat treatment to the point at which the necks between particles impinge upon each other. Subsequently, as sintering proceeds, the growing necks merge and the so-called intermediate stage of sintering begins. In this stage, pores are continuous and all pores are intersected by grain boundaries. Many concurrent phenomena govern the microstructural evolution. Grain boundary migration, and resulting grain growth, can begin when the porosity becomes sufficiently low. Depending on the relative rates of densification and grain growth, pores may migrate along with the advancing boundaries and, therefore, the average pore size may increase through pore coalescence. Surface diffusion may increase the average pore size by locally redistributing material from regions of convex curvature to regions of concave curvature. Ultimately, during the final stage of sintering, the pore space is broken-up into isolated pores. These pores may all remain on grain boundaries, or alternatively they can become isolated from the grain

boundaries during discontinuous grain growth.

During the past 30 years, a large number of studies have been made in an attempt to provide a better general understanding of the sintering process. Aluminum oxide has been one of the most widely used materials for these investigations. The influence of surface energy as the driving force for sintering, the importance of diffusion processes for mass transport (Frenkel,[1] Pines,[2] Kuczynski[3]), and the role of grain boundaries as material sources (Kingery and Berg,[4] Alexander and Baluffi[5]) seem well established for the polycrystalline solid state system. However, attampts to develop a quantitative theory that can predict the time dependence of densification of a powder compact have not been very successful. This situation is due primarily to the difficulties in precisely defining the geometrical changes that evolve during the sintering process.

In general, six different transport processes have been considered as contributing to the observed geometrical changes - viscous flow, plastic flow, evaporation-condensation, volume diffusion, grain boundary diffusion, and surface diffusion. Since the internal geometry of actual compacts can not be defined precisely, attempts to establish the mechanism of transport have usually been based on a consideration of idealized model systems of simple geometry. The first demonstration of mass flow by volume diffusion was provided by Kuczynski[3,6] in studying metallic systems. He was able to derive an equation relating the growth of the neck between a sphere and a plate (Fig. 1) to time, t, at constant temperature. The well-known relationships between the radii, x, of the neck, and, R, of the sphere, time, t, and temperature, T, can be

0 0 0 0 0 4 7 0 0 1 2 3 3 3 5

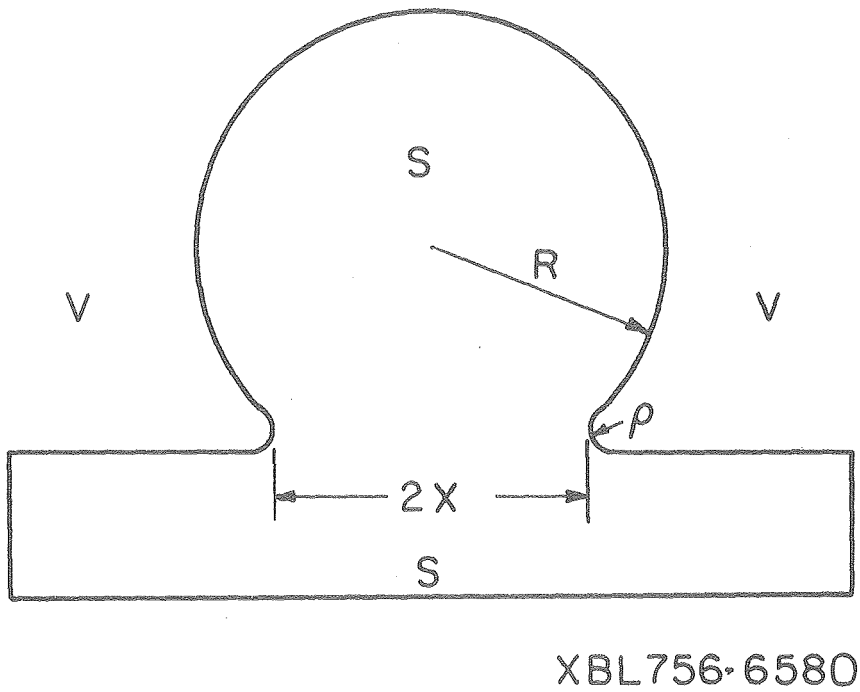

Fig. 1. Kuczynski's model for neck growth between a sphere and a plate ; R = radius of sphere, 2X = diameter of neck, and ρ = radius of neck.

described by one general equation

$$X^n/_R{}^m = F(T)t \qquad (1)$$

where F(T) is a function of temperature only. The dominant flow mechanism is determined by exponents n and m. Thus

n = 2 m = 1	for viscous flow
n = 3 m = 1	for evaporation - condensation
n = 5 m = 2	for volume diffusion
n = 7 m = 3	for surface diffusion

Kuczynski's model for neck growth between the sphere and the plate by volume diffusion was based on the assumption that vacancy diffusion occurred radially from the concave surface of the neck to sinks on the surface of the sphere. From experimental observations made on copper and silver, he observed that neck growth occurred primarily by volume diffusion. However, surface diffusion also played an important role in the early stages, especially when the spheres were small.

Later, Kingery and Berg[4] proposed a model consisting of two spherical particles with a grain boundary between them which was considered to act as the vacancy sink. Atoms would then diffuse radially from the grain boundary to the surface of the neck, causing neck growth, while at the same time, the removal of material from the grain boundary would cause the distance between the particle centers to decrease. Figure 2A shows that neck growth may occur by mass transport from the particle surfaces to the neck region while retaining the separation between the centers of the original particles. This could occur by an evaporation-condensation mechanism, volume diffusion from the convex surfaces, or by a surface diffusion mechanism. This process will

0 0 0 0 0 0 0 4 4 7 7 0 0 4 0 2 5 5 3 9 6

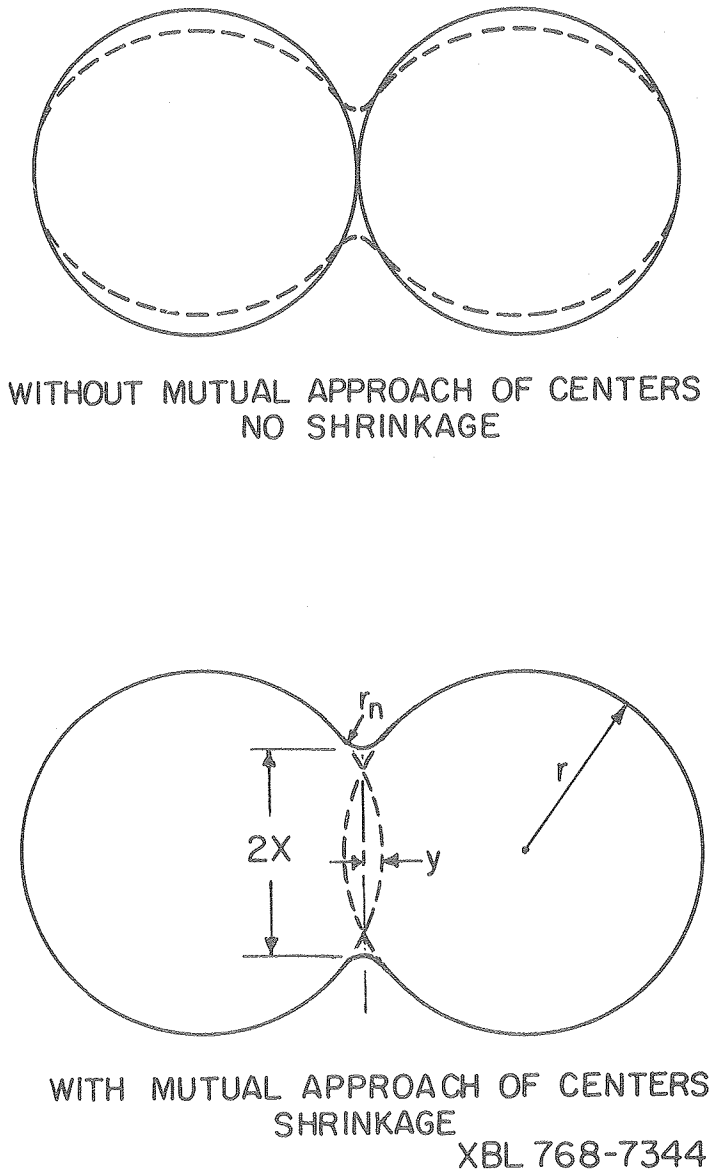

Fig. 2. Two models for initial stage of sintering of spheres.

produce particle joining, but no shrinkage. Figure 2B shows the joining of particles with the mutual approach of centers. In principle, this can occur by plastic flow or by volume diffusion. Matter in the region of overlap is transported to the neck region by diffusional transport of individual atoms or ions through the bulk of the material or along the grain boundary. By extending this simple geometry, Kingery and Berg[4] and Coble[7] were able to derive an expression in terms of linear shrinkage of the powder compact. All the results can be put in the form

$$\frac{\Delta L}{L_o} = \left(\frac{KD\gamma\Omega t}{kTr^n}\right)^m \qquad (2)$$

where K is a constant whose magnitude depends on the geometry selected and D is the volume diffusion coefficient. The value of m ranged between 0.4 and 0.5 and that of n is usually 3.

Johnson and Cutler[8] have proposed that grain boundary diffusion, rather than volume diffusion, contributes significantly to neck growth in the initial stage. They analyzed the initial shrinkage of aluminum oxide and concluded that it is controlled by grain boundary diffusion. In all models, mentioned above, a single mechanism of material transport was assumed to be predominant. More recently, Johnson[9] has analyzed a situation, using sphere-to-sphere and sphere-to-plate contacts, in which it is assumed that surface diffusion, lattice diffusion and grain boundary diffusion all take place simultaneously.

For all the above models, neither particle shape nor particle size distribution was taken into account. Bannister[10] proposed a modification to Johnson's model (based on concurrent operation of volume diffusion and grain boundary diffusion) by calculating particle shape effects. His

0000 0047700 4023 4307

work accounts for variations in particle contact due to shape. Other initial stage modeling by Coble[11] has considered particle size distribution effects in volume and grain boundary diffusion models. Of various possible three-dimensional arrays of interest, only a linear array of particles with different randomly distributed sizes has been quantitatively handled.

Based on the volume diffusion mechanism and simplified geometry for pores and grains, Coble[12] has developed diffusion models for the intermediate and final stage sintering. In these models, he assumed all grains have the same size and shape. The shape was that of a tetrakaidecahedron, a space-filling polyhedron, all of whose edges have the same length. The pores were likewise assumed to be of the same size. In the intermediate stage, pores of cylindrical shape lying along all grain edges were assumed and, in the final stage, spherical pores at the four grain corners were assumed. Considering that the vacancy flow is by volume diffusion from a single pore to the boundaries of the adjacent grains, he obtained the following equation for the rate of change of density, ρ, for both stages:

$$\frac{d\rho}{dt} = \frac{N\gamma D\Omega}{l^3 kT} \tag{3}$$

where N is a numerical constant, l is the edge length of a grain, and D is the volume diffusion coefficient.

Kingery and Francois,[13] working with UO_2, observed an increase in pore diameter if the material was annealed long enough at high temperature. They proposed that pore growth results from coalescence due to pore migration which accompanies grain growth. Coble[14] conceded that

the evolution assumed in his intermediate stage model is not valid because of pore growth. To understand completely the mechanisms of intermediate and final stage sintering, one must take into account changes in pore size, location, and geometry.

Kuczynski[15] argued that pore growth was caused by a volume diffusion process by which large pores grow at the expense of small ones. Therefore, he concluded that the phenomenon of pore shrinkage is always accompanied by Ostwald ripening. He took a statistical approach in which a distribution of pore radii was allowed and not all edges of the grains had to contain pores. Similarly, no restriction was placed on the size and shape of the grains. Assuming a single volume diffusion mechanism and cylindrical and spherical shaped pores for the two respective stages, he was able to formulate a relationship between grain size and porosity and an equation for the time dependence of the densification process.

In most polycrystalline materials, at high temperature, grain boundary migration eliminates some grains and increases the average grain size. In a system where sintering kinetics is determined by a diffusion mechanism, maintaining a small grain size can increase densification rates by maximizing the concentration gradient of vacancies between pores and grain boundaries. The importance of grain growth during sintering was first demonstrated by the work of Burke[16] on aluminum oxide which showed that, when exaggerated grain growth occurred, some pores were trapped in the grains far from grain boundaries, resulting in residual porosity. Coble[17] first demonstrated that the addition of small amounts of MgO (below the solubility limit) would prevent exaggerated grain growth in aluminum oxide and thus would permit sintering to

0000 0047700423431 8

proceed to theoretical density provided there is proper control of the sintering atmosphere. Since the MgO also considerably increased the rate of densification, Coble suggested that its action was to promote rapid densification through the critical porosity range in which discontinuous grain growth occurred.

Further work on the effect of MgO on Al_2O_3 has been done by Jorgensen and Westbrook.[18] They suggested that inhibition of grain growth is accomplished by the segregation of dissolved MgO to grain boundaries, causing a decrease in grain boundary mobility. However, this segregation theory has been denied by Johnson and Stein[19] through their interfacial chemical analysis using an Auger electron spectroscopy technique. Instead, they proposed that the presence of a nonstoichiometric spinel was responsible for the retardation of grain growth. More recently, Peelen[20] also proved that there is no significant concentration of MgO in the grain boundary. He found that the essential action of MgO was to enhance the pore removal rate. At higher dopant levels, when second phase particles are present, grain growth is slowed but the densification is negatively influenced.

With the "exaggerated grain growth inhibitor", the study of grain growth kinetics was made possible. Coble,[17] Jorgensen,[21] and Bruch[22] have found, during their sintering studies with MgO doped Al_2O_3, that the grain growth kinetics followed a cubic law. Bruch[22] also observed that the rate of grain growth was independent of the initial density of the compact. Greskovich and Lay[23] found that grain growth occurred even in a very porous aluminum oxide compact. They have proposed that the mechanism which governs grain growth is that of surface diffusion

for neck formation. The grain boundary then moved through the particle. Several rate laws have been suggested for grain growth in oxide ceramics,[24,25,26] and several mechanisms have been proposed by which the rate of grain growth is limited to the observed values.[27, 28, 29] Because of incompletely understood complexities, such as the impurity effect, sintering atmosphere, and pore-grain boundary interaction, our knowledge of this subject is still on an empirical basis.

In spite of the extensive research activity on the theory of sintering, there has been little translation of theory to practical application. Mechanistic studies have relied heavily on simple models. However, in a real powder system, particles rarely have regular forms and they are never simply distributed. In addition, there are fluctuations in density originating from powder agglomeration and uneven compaction. At this point in time it seems unlikely that a precise prediction of a density - time - temperature relationship can be achieved for the whole course of the sintering process. Therefore, a thorough phenomeno-logical study of the densification kinetics and the microstructural evolution kinetics as well as their correlations from the start to the completion of the sintering process is important.

Previous sintering studies have concentrated on the use of isothermal techniques. A complete analysis of sintering kinetics is unattainable due to uncertainties involved in the initial heating period. The type of heating program that can be treated analytically and which approaches practical application is a constant rate of heating. This work has used a constant heating rate technique to obtain a detailed analysis of the kinetics of sintering aluminum oxide powder compacts.

0090004477004023 4329

Kinetics of both densification and microstructural evolution were studied with variations in Al_2O_3 powders and in initial compact density. Correlations between the two kinetics were made and the validity of various existing theories was examined. It is hoped that the work will assist in developing a better theory for sintering of powder compacts.

II. EXPERIMENTAL

A. Apparatus

1. Hot Stage Scanning Electron Microscope

A commercial hot stage for the JEOL JSM-U3 was modified to give a device capable of magnifications from 50 to 4,000X and long-time operations at temperatures up to 1750°C. The design changes centered around the construction of a reliable heater, increased radiation shielding, and modification of the thermal electron suppression grid to allow a shorter working distance and, hence, greater resolution. A turbo molecular pump was used in place of an oil diffusion pump for the vacuum system. This change greatly reduced the surface contamination of the specimen during high temperature operation. A detailed description of the principles of operation of this instrument has been reported by Fulrath.[30]

Hot stage scanning electron microscopy has been successfully used for the studies of both solid state[31,32] and liquid phase sintering.[33,34] This technique has several advantages when compared with other methods: (1) It provides a means to monitor continuously the dimensional changes of a specimen during the sintering process. (2) The temperature gradient across the specimen is negligible during heating because of the small size of the specimen. (3) It makes possible a statistical analysis of the densification results. A limitation exists, however, in that there is a necessity for a vacuum environment (about 3×10^{-5} torr) in the operation of the SEM.

The specimen stage carrier for the scanning electron microscope is shown in Fig. 3. The heater was made by winding a 15 mil thoriated tungsten wire on a high purity threaded aluminum oxide core. A slotted

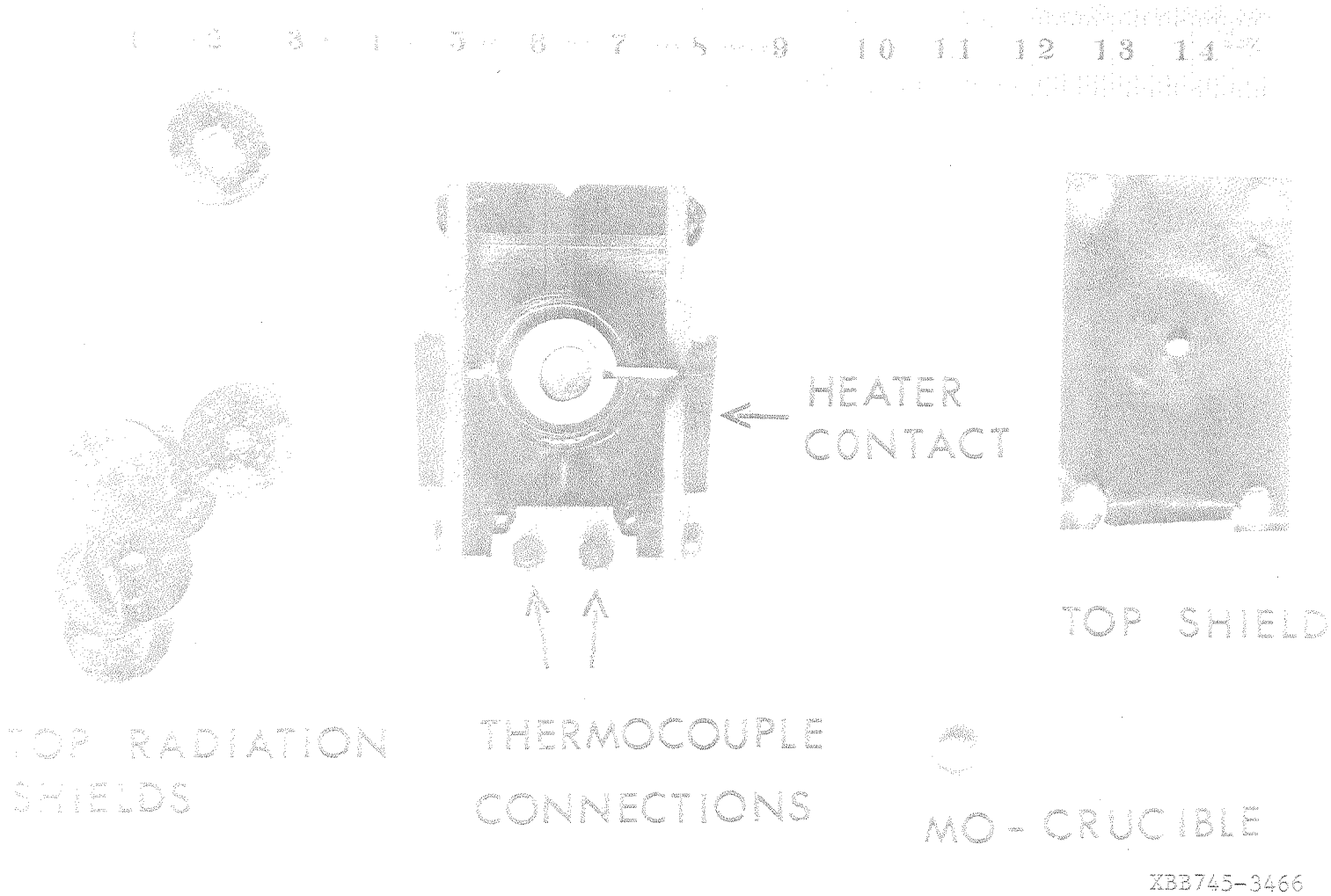

Fig. 3. Hot-stage specimen carrier.

0004107 0004 7 0 0 0 0 4 3 2 8 4 1 3 0

aluminum oxide sleeve was jacketed over the core to hold the tungsten wire in position during high temperature operation. The molybdenum crucible was supported within the heating element by a molybdenum stand. The temperature measurements were obtained with a 5 mil, W5%Re-W26%Re thermocouple spot welded to the bottom of the stand. Molybdenum radiation shields surrounding the heating element and placed above the specimen allowed increased temperature capability. The electrical connections for the heater and thermocouple were isolated from the metal frame by aluminum oxide plates.

2. Temperature Calibration Device

Since the thermocouple wire was not positioned closely enough to the specimen being heated, the thermocouple temperature was calibrated to give the true specimen temperature. The set-up shown in Fig. 4 was used to accomplish this purpose. During the operation, the stage was placed in a vacuum chamber that had the same environment as the column of the microscope except for the absence of an electron beam. A calibrated optical pyrometer was used to record the specimen temperature by viewing the specimen surface through the hole in the top radiation shields. For each optical pyrometer reading, the thermocouple temperature and the power input to the heating element were also recorded. Figure 5 shows the heater power input-thermocouple temperature relationship for four rates of heating. It shows that approximately 80 watts were required to heat the specimen to 1700°C, and this power was independent of the heating rate. Figure 6 gives the temperature calibration curves. The specimen temperature was always higher than the thermocouple temperature and the temperature difference changed with changing

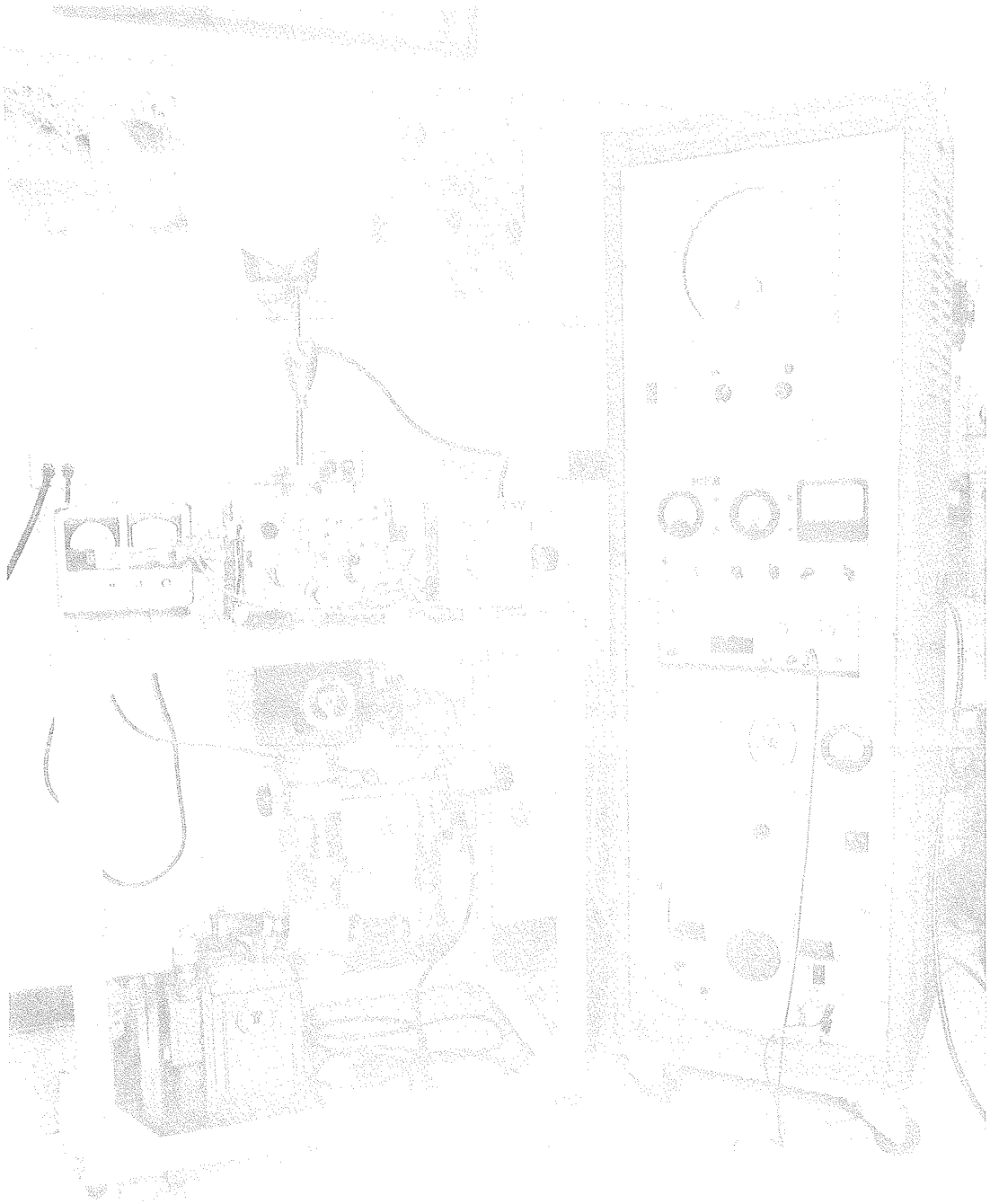

XBB763-2421

Fig. 4. Temperature calibration device

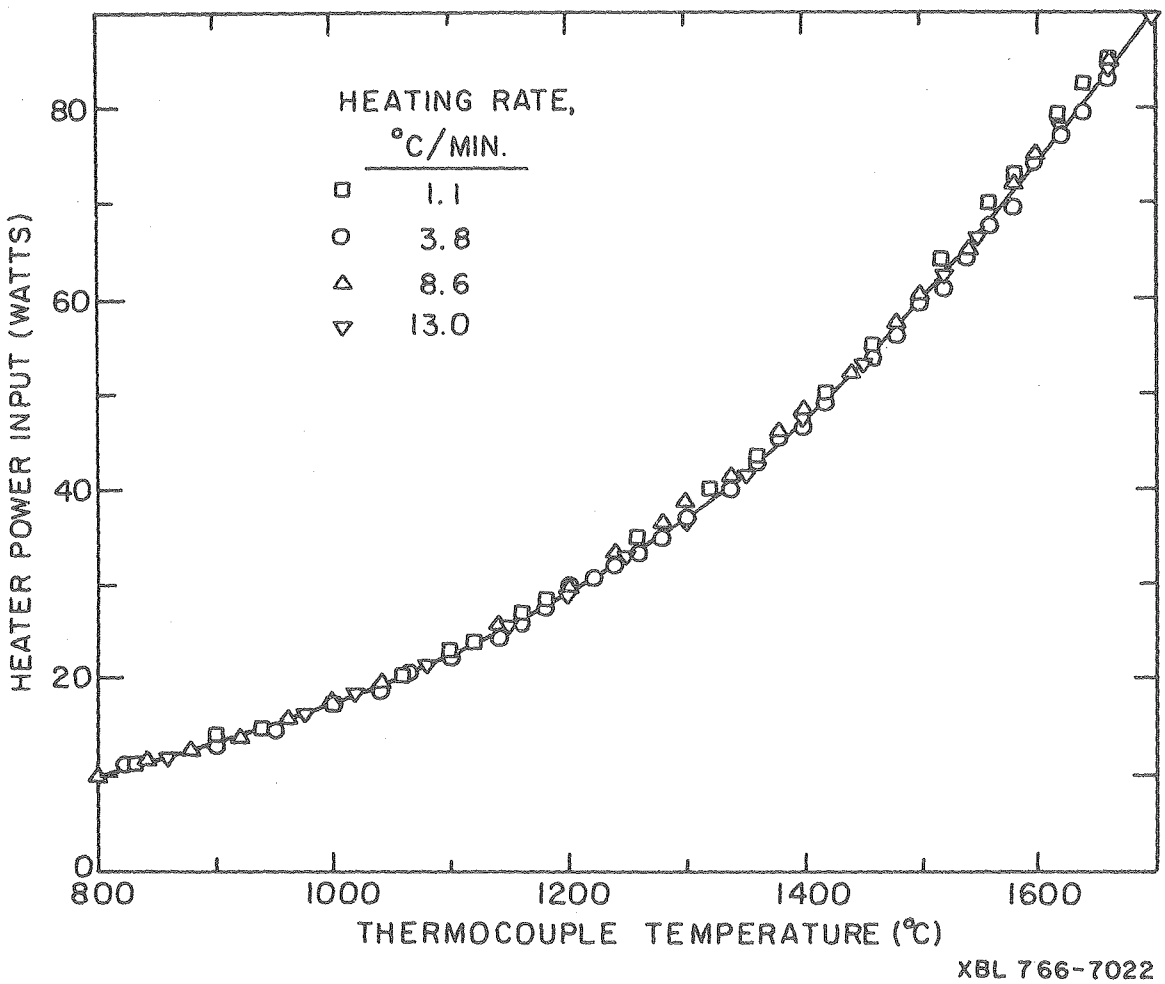

Fig. 5. Heater power input - thermocouple temperature relationship.

0 0 0 0 4 7 0 4 3 4 3

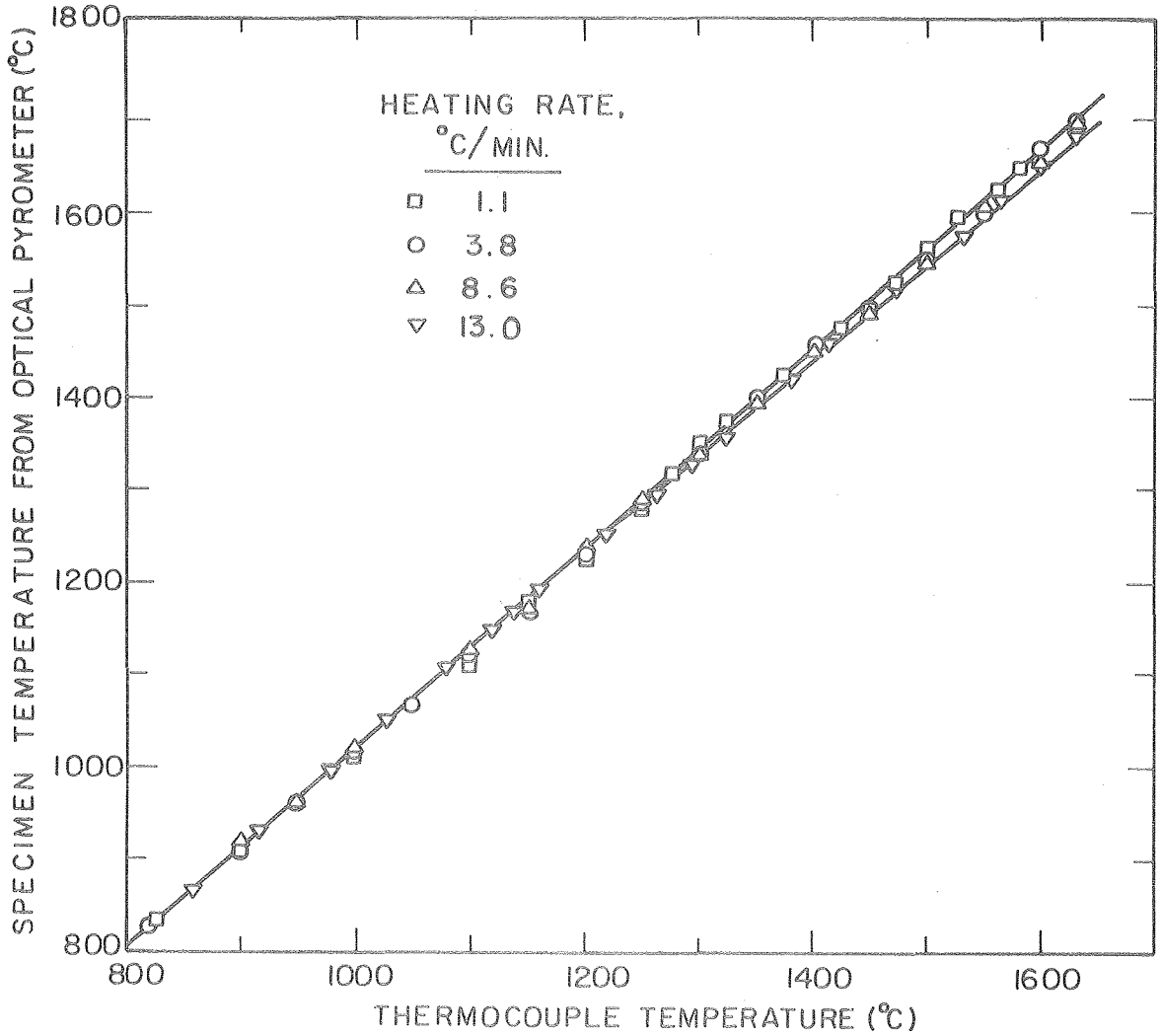

XBL 766-7023

Fig. 6. Specimen temperature from optical pyrometer vs. thermocouple temperature.

temperature. For example, at thermocouple temperatures of 1200°C and 1600°C, the specimen temperatures were 1230°C and 1660°C, respectively. The greater deviation at higher temperature apparently resulted from conduction heat loss through the thermocouple wires at the junction. The deviation of the 13°C/min heating rate curve from those of lower heating rates is thought to be caused by thermal non-equilibrium of the specimen when heated at this fast rate. Hereafter, all the reported temperatures will be based on the corrected (i.e. calibrated) specimen temperatures.

B. Material and Sample Preparation

Four different types of aluminum oxide powders were used in this study. The material that was used for most of this work was autoclaved high purity aluminum oxide. This material was obtained from the General Electric Company in the form of plates with a diameter of 2 inches and a thickness of 0.125 inch. The compact was made by cold pressing submicron alumina particles (0.2μm), to which 0.1 wt% of MgO and 8 wt% of an organic binder were added. This compact was prefired at 650°C in air for one hour to decompose the organic binder. After this treatment, the outer and central portions of the compact were discarded and the rest of it was broken into pieces of approximately one centimeter square. Specimens used for the sintering experiments were then cut and shaped from these pieces. The green density was determined for each piece by mercury displacement. This method of specimen preparation minimized the variations in the green density caused by any pressure gradients during powder compaction. All the specimens had a diameter of 0.2 inch and a thickness of 0.125 inch with the same green density of 40% of theoretical.

The other three types of aluminum oxide were processed and formed into compacts from powders in this laboratory. Alcoa A-14 alumina powder was wet ground for 16 hours with isopropyl alcohol as the milling medium and sapphire balls as the grinding media in a high purity (99.98%) alumina lined rotating steel mill. This procedure was used to break up agglomerates. The wet ground A-14 material had an average particle size of 2.5μm and a very narrow size distribution as determined by scanning electron microscopy. Union Carbide Linde-A alumina (0.3μm) powder

(Lot No. 1006) and W. R. Grace & Co. high purity alumina (0.1 m) doped with 0.1 wt% of MgO (Lot No. 2156A-52) were used as received.

Each of these three powders was mixed with isopropyl alcohol and a polyvinyl alcohol-saturated water solution in the alumina lined mill for 12 hours. This was done to ensure a uniform distribution of PVA binder in the final compact. The amount of PVA added depended on the surface area of the powders. It ranged from 1 wt% to 8 wt%. In the study of MgO doped alumina, the appropriate amount of Mallinckrodt A-R grade magnesium nitrate was dissolved in distilled water and added to yield 0.1 wt% MgO in the alumina powders. The slurry after the mixing process was dried, screened through a 44μm sieve and cold pressed in a steel die. To obtain variations in green densities, the powders were compacted in steel dies at various pressures, but the bulk specimen volume was kept constant by adjusting the amount of powder used.

In most cases, isostatic pressing in rubber tubes was subsequently used. All the pressed specimens had approximately a 0.2 inch diameter and a 0.1 inch thickness. The green densities of the specimens were determined after the prefiring treatment at 650°C in air for 1 hour.

To study the linear dimensional change of the specimen during sintering experiments, tungsten microspheres (10-20μm) were placed on the specimen surface to serve as reference points. This was done by lightly tapping a small spatula, on which a small number of tungsten spheres were held, over the specimen surface. A random distribution of the spheres was obtained. A glass slide was lightly pressed on the microspheres to ensure their stability on the surface. The specimen was then placed in the crucible of the stage carrier and inserted into the SEM.

0 0 0 0 0 4 7 0 0 2 3 4 4

C. Shrinkage Measurements

The specimens were heated rapidly to 800°C in the SEM and held at that temperature. The central area of the specimen was located and brought into focus. 100X magnification was used in order to cover a large area of the specimen surface to give better statistical shrinkage measurements. The specimen was kept in focus during dimensional changes by raising and lowering the specimen stage to keep the working distance constant. This technique eliminated any magnification changes accompanying focal adjustments.

Constant heating rates, ranging from 1° to 13°C/min were used. In some cases, specimens were heated with a constant heating rate to temperature and held at temperature for a period of time to obtain isothermal densification results. During the sintering runs, a 16 mm movie camera monitoring the TV screen was used to record continuously the movement of the tungsten markers. Images obtained from the time lapse films were projected on a paper through a reflecting mirror system. From these images, linear dimensional changes were obtained by measuring distances between specific microspheres. At least seven measurements at each temperature were used to provide an average shrinkage. Figure 7 illustrates how these dimensional changes between microspheres provide a measure of specimen shrinkage. The lower left corner of the TV monitor shows the temperature in degrees centigrade and the right corner shows the time in minutes. Since the fractional shrinkage $\left(\frac{L_o - L}{L_o}\right)$ at all temperatures were determined with the same low temperature value of L_o, a thermal expansion[35] correction was made for each of

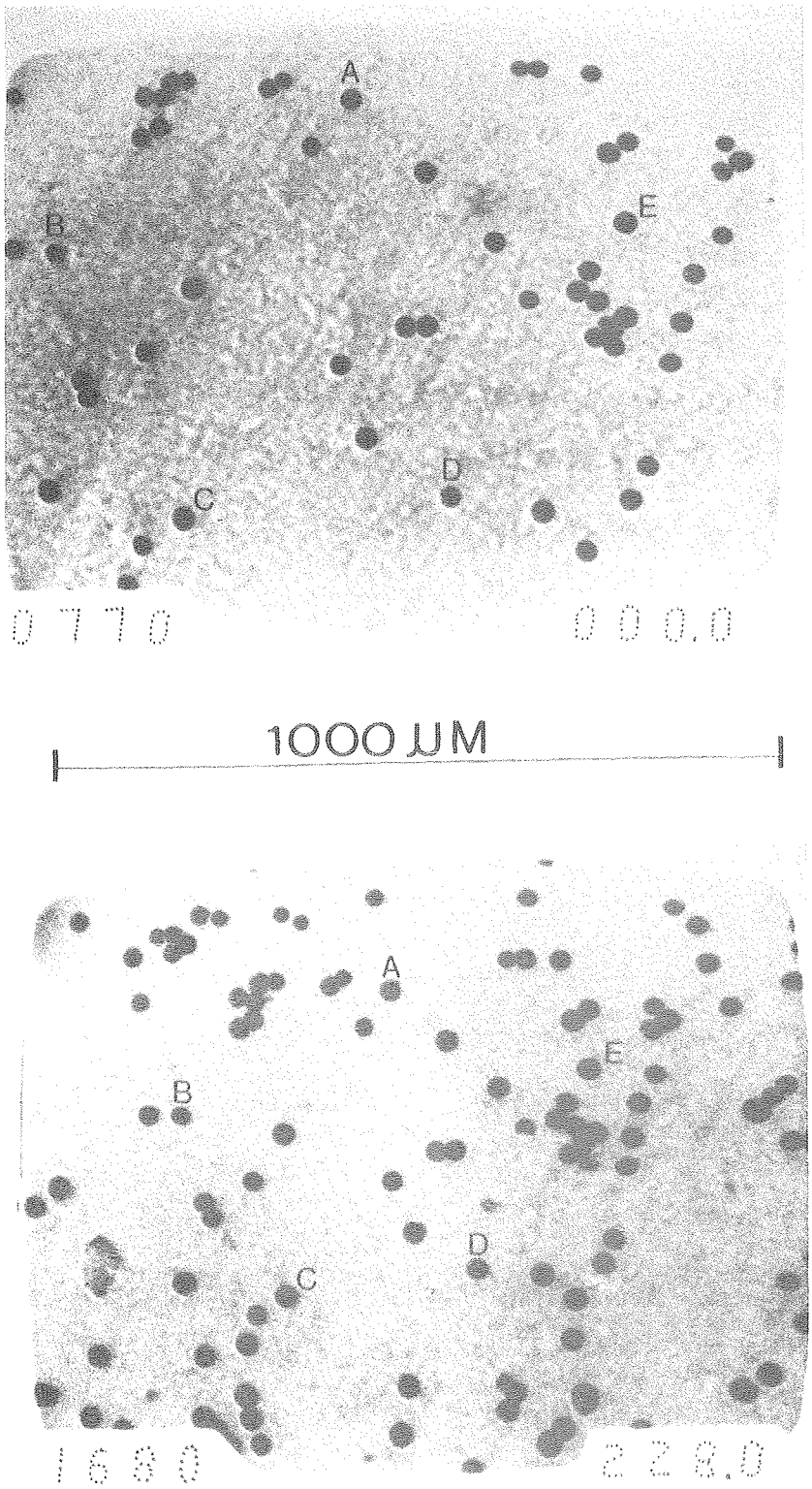

XBB768-7120

Fig. 7. Tungsten microspheres on the compact surface as seen on the TV monitor before and after sintering. Temperature in °C is indicated in the lower left corner and elapsed time in minute is indicated in the lower right corner.

the measurements. In the analysis of experimental results, most data were presented as relative density (ρ) instead of as fractional shrinkage ($\Delta L/L_o$). In order to make this conversion, let us consider an aggregate of powder particles of arbitrary shape, size, size distribution, and stacking. Select a macroscopic sample from this aggregate that is cubic in shape. Let the weight of this sample be W, its volume V_o, its density ρ_o, and its edge length L_o, where

$$V_o = L_o^3 \tag{4}$$

After undergoing a certain degree of sintering, its volume decreases to some value V_i, its density increases to ρ_i, its weight does not change. If shrinkage is macroscopically isotropic the sample is still cubic in shape, although its edges have shrunk in length to some value L_i, where

$$V_i = L_i^3 \tag{5}$$

$$\frac{L_i^3}{L_o^3} = \frac{V_i}{V_o} = \left(\frac{W}{V_o}\right) \Big/ \left(\frac{W}{V_i}\right) = \frac{\rho_o}{\rho_i} \tag{6}$$

The density is therefore given by

$$\rho_i = \frac{\rho_o}{L_i^3 / L_o^3} = \frac{\rho_o}{\left(1 - \frac{\Delta L}{L_o}\right)_i^3} \tag{7}$$

Since n measurements were taken for each temperature or time, the relative density value used in this study was actually

$$\rho = \frac{\sum_i^n \rho_o / \left(1 - \frac{\Delta L}{L_o}\right)_i^3}{n} \tag{8}$$

where ρ = average density at any time or temperature.

ρ_o = green density of the specimen

$\frac{\Delta L}{L_o}$ = fraction shrinkage in each measurement after thermal expansion correction at any time or temperature.

n = number of measurements at any time or temperature.

D. Microstructure Study

1. Sample Preparation

Compacts of the different types of powders with varying green densities were heated in the hot stage at programmed heating cycles to desired densities and cooled by quenching. The sample density was determined by the same procedure as described in Section II-C. These samples were used to study the microstructural evolution during the sintering process and to correlate it with densification kinetics. Samples used to study the effect of firing atmosphere on the final microstructure were obtained by heating in a Brew furnace. Static hydrogen at 0.8 atmospheres and 10^{-6} torr were used. The compacts were heated to 1200°C slowly and then brought to 1750°C in approximately 20 minutes. Holding times of one hour and ten hours were used at this temperature.

2. Polishing and Etching

In order to avoid grain pull-outs, uneven polishing, and entrapment of polishing media in pores, a sulfur impregnation technique was applied to all low density samples ($\leq$95% theoretical). Rough polishing with a series of SiC powders from 240 to 1000 grit was followed by vibratory polishing with a series of diamond pastes (6, 1, and 1/4μm) on a Syntron machine.

After being polished, samples were removed from their plastic mounts and the impregnated sulfur was sublimed. Samples were thermally etched in air at temperatures from 1100°C to 1250°C for various periods of time up to two hours depending on the sample density. Temperature and time were selected to avoid any additional microstructural changes induced by excessive firing during the etching process.

3. Photography

Cold pressed, fractured and polished surfaces were examined and photographed by either optical or scanning electron microscopy. Due to careful preparation, no tilting of the samples was required to give sharp images of grain boundaries and pore morphology when examined in the SEM.

Pressed and fractured surfaces were examined for the characterization of the green compacts. Polished surfaces were used for studies of porosity distribution and grain size evolution. Due to the inhomogeneous nature of the microstructure and the fine size of grains, both low and high magnification pictures were required. Low magnification pictures, from 500X to 2,000X, were taken for a qualitative study of porosity distribution. High magnification pictures, from 10,000X to 20,000X, were taken for a quantitative study of grain growth. Since higher magnification pictures cover too small an area to obtain an average quantitative value, several pictures were taken in different areas of each sample. Optical photomicrographs at 1,000X or less were used for samples of large grain size.

4. Grain Size Measurement

In order to determine an average grain size for porous samples, photographs were placed underneath a transparent plastic sheet, on which parallel lines had been drawn. Segments of lines, formed by the interceptions of grain edges with those parallel lines, were measured individually and 500 to 800 of these segments were averaged to yield a preliminary value. This value was then corrected for magnification factors and multiplied by 1.5 to give an average grain size.[36] For samples

having densities $\geq$95% theoretical, grain size was obtained by counting the number of grain boundaries intercepting straight lines of known length. Magnification and statistical (multiplication by 1.5) corrections were also made.

III. RESULTS AND DISCUSSION

A. Description of the Green State

In order to increase the sinterability, ceramic powders of submicron size are commonly used. The higher total surface area and shorter distances for the mass transport provided by submicron size powders is considered to increase sintering rates. In contrast, increased agglomeration of particles may reduce the sinterability by causing undesirable residual porosity in the final microstructure.

Particles formed from a salt solution may agglomerate at some point during the decomposition-calcination process.[37,38] If agglomeration does not occur during powder formation, pre-compaction granulation may cause agglomeration of particles. Granulation is an essential step for increasing the pressed density and improving the homogeneity of the compact by improving the inherently poor flow properties of fine particles.

Since voids contained in a green compact are determined by the packing of particles, the presence of agglomerates will make the pore size, location and distribution more complex than assumed in models. A profound influence would be expected on both the rate of sintering and, more importantly, the residual porosity. Therefore, a complete understanding of the green state should be emphasized.

Scanning electron fractographs of a prefired green compact at different magnifications are shown in Fig. 8. This type of compact, having an initial density of 40% of theoretical, was used for most of the present work. As seen in Fig. 8A, agglomerates of about 40 microns in diameter resulted from the granulation operation. The average agglomerate size was determined by measuring nearly 300 individual

Fig. 8. Remaining vitreous fractograph of prefired [illegible] alumina powder compact with a green density of 60% of theoretical taken at three different magnifications.

agglomerates from photographs of the pressed compact surfaces. (See Fig. 9A). The distribution histograms are shown in Fig. 10. These results can be used to deduce information about the size and distribution of the inter-agglomerate voids. In this work, no quantitative measurements have been made.

The details of particle packing can be seen in higher magnification photographs, Figs. 8B and 8C. In addition to the large agglomerates (granules), Fig. 8C shows that there are numerous small agglomerates formed by several individual particles. These clusters of particles are generally close packed and contain very fine pores of nearly uniform size. However, the inter-cluster pores are not uniformly distributed in size, shape, and location. Whittemore and Sipe[39] used mercury porosimetry to measure the pore size distribution of Linde A alumina compacts which were pressed isostatically without the addition of binders. They observed a bimodal pore distribution and found that this bimodal characteristic was independent of the compaction pressure. In the present work, quantitative measurement of pore size distribution was not made. However, from the photomicrographs, one can see with confidence that the pore size distribution in the compact is at least bimodal and probably trimodal. This is further illustrated by Fig. 9C which is taken from a pressed compact surface.

Figure 11 shows the fractographs of three different green density compacts. Their densities are 32%, 38% and 48% of theoretical for A, B, and C, respectively. The inter-particle packing is very similar for all these specimens. It appears that the difference in density results mainly from the size and number of the inter-agglomerate pores.

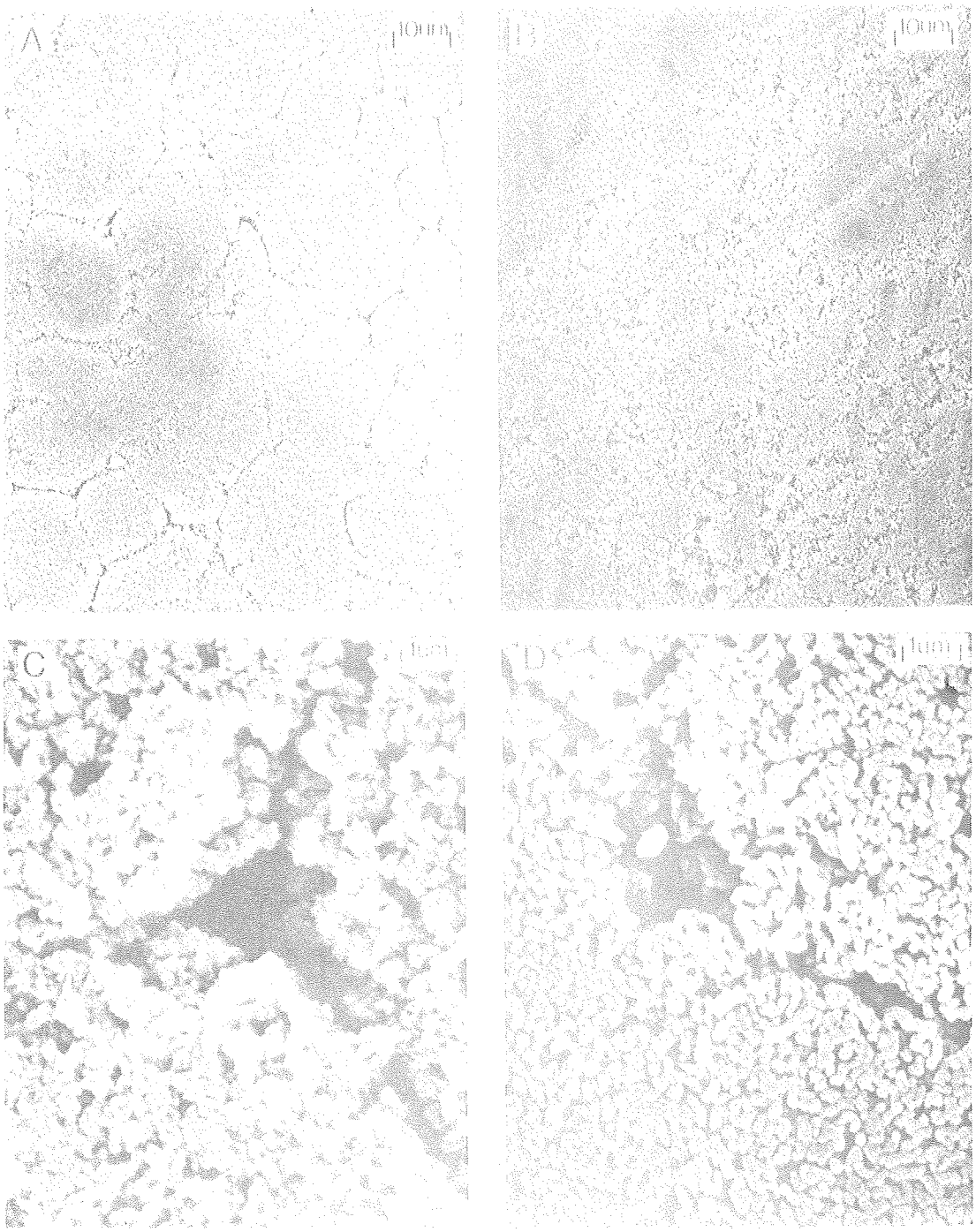

XBB768-7110

Fig. 9. Scanning electron micrographs taken from pressed compact surfaces (A and C, G. E. powder; B and D, Union Carbide powder).

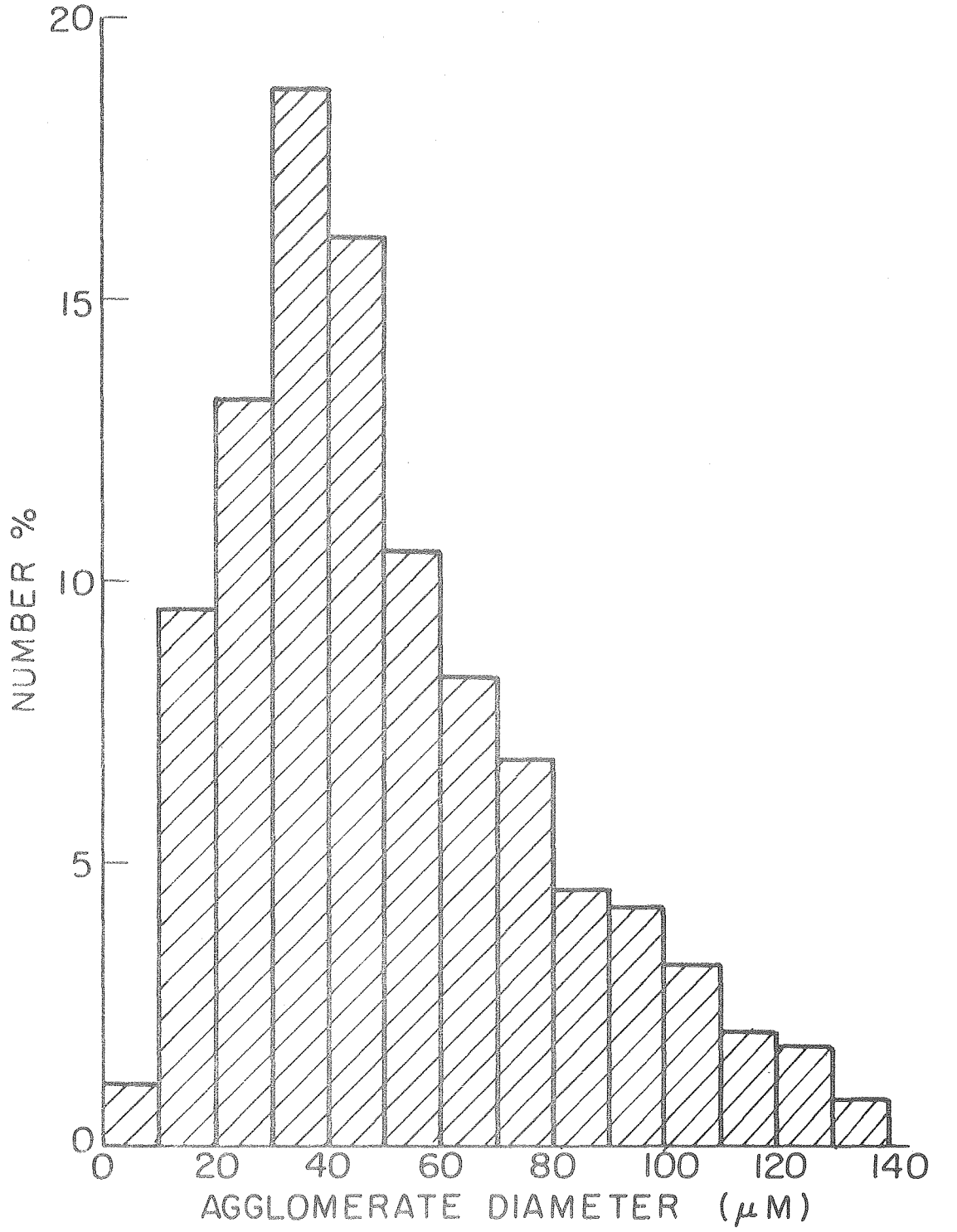

XBL764-6776

Fig. 10. Agglomerate size distribution for G. E. powder compact.

0 0 1 0 4 7 0 0 3 5 0

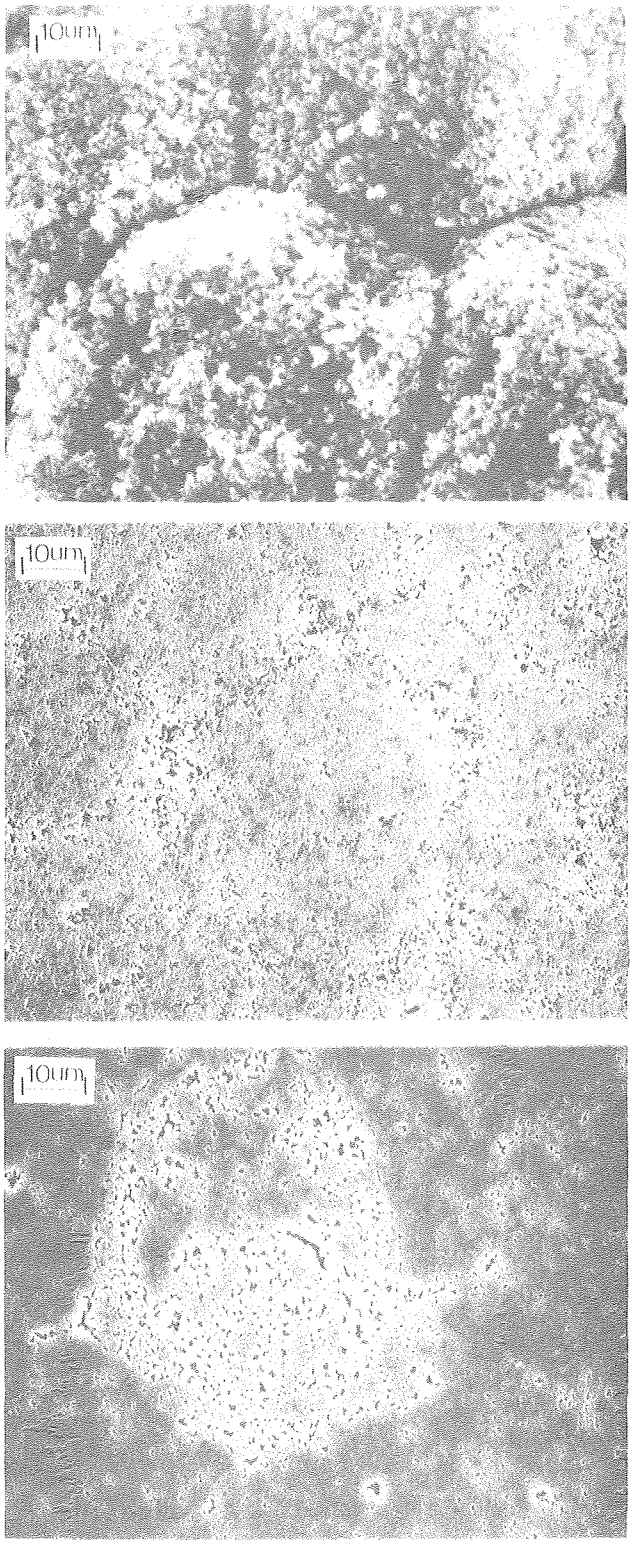

XBB761-826

Fig. 12. Evolution of inter-agglomerate porosity at different degrees of sintering for G. E. Al_2O_3 powder compact. Top to bottom: Green compact (40%), 85%, and 90% relative density.

powder, but must also take into account the particle packing which affects pore size, shape and distribution.

Figure 9 gives the comparisons of green compact microstructures formed from two different powders. Figures A and C are formed from powders which have been granulated as described previously. Figures B and C are formed from powders which have been granulated as described previously. Figures B and D are Union Carbide Linde A alumina. This powder was granulated by screening through a 44 micron sieve after mixing with PVA binder and drying. Because the binder and powder were different, granules formed from the Union Carbide powder did not survive the compaction operation. Though the fact is not as clear as with the G. E. powder, the granules still keep their identity, as seen from the green compact (Figs. 9B and D) and as seen in the microstructure of the final product (Fig. 13). Figure 13 shows essentially the same microstructures as seen in Fig. 12. It should be noted that in Fig. 13C, the area focused upon is a white spot on the polished surface of a translucent sintered compact. White spots frequently have been observed in densely sintered ceramic oxides, such as MgO and Al_2O_3. Greskovick and Woods[40] have found that pore clusters entrapped inside grains of ThO_2-doped Y_2O_3 ceramics profoundly reduce the optical quality of this material. Their observation of pore clusters can be explained by the present work in terms of the presence of agglomerates in the green compact. If the microstructure shown in Fig. 13C is annealed for a long time at high temperature, the grain growth rate will be increased. The pores which resulted from the initial agglomeration of particles will finally become entrapped inside the grains, forming the same type of

0 0 0 0 0 3 4 7 0 0 4 5 3 0 1

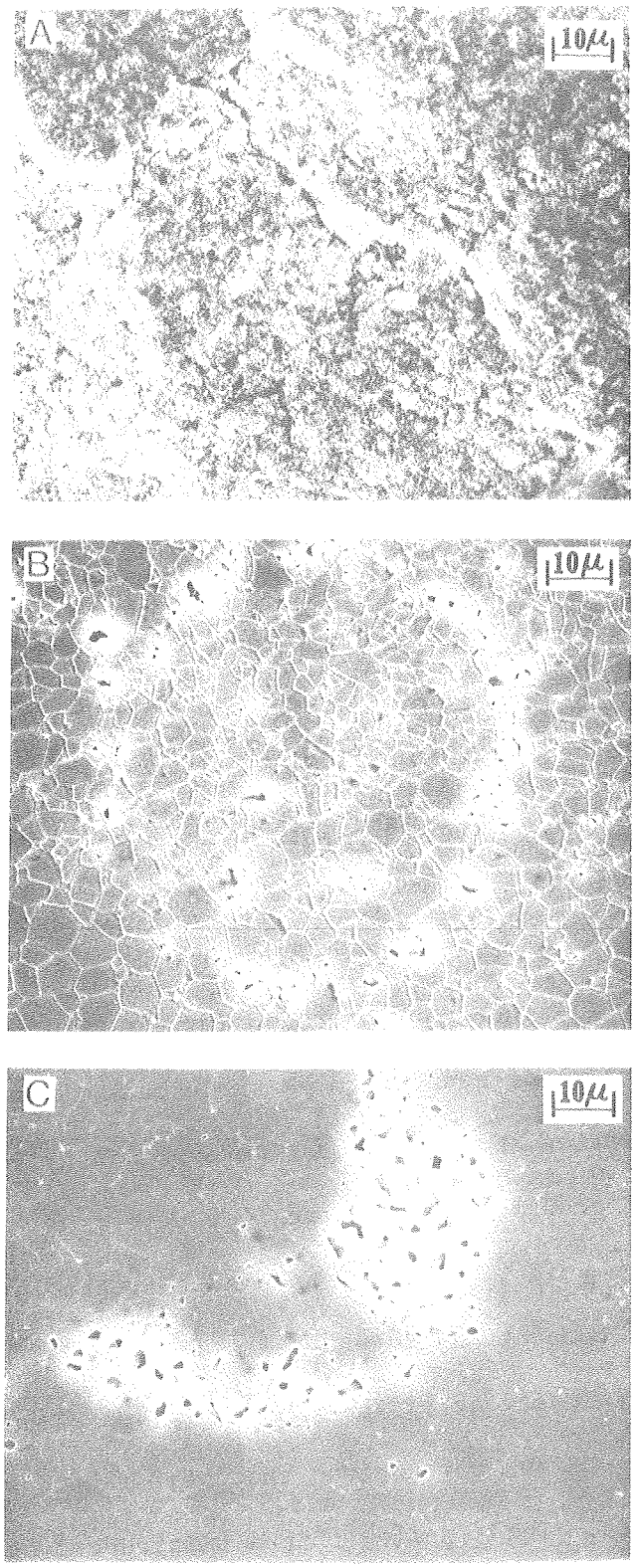

XBB768-7111

Fig. 13. Evolution of inter-agglomerate porosity at different degrees of sintering for Union Carbide Al_2O_3 powder compact. (A) green compact (40%), (B) 96%, and (C) 99+% relative density.

microstructure as observed by Greskovick.

Figure 14 consists of a series of pictures which show the evolution of an inter-agglomerate pore during the sintering process. The micrographs were not taken from the same area of one compact. However, since the powder processing was well standardized, they are considered to be representative for the evolution of a single inter-agglomerate pore. Two points of speculation should be considered. Firstly, the final pore geometry seems to be determined by the agglomerate packing in the original compact and, therefore, the complex pore shape can not be approximated as spherical as assumed in common models. Secondly, inter-agglomerate pores persist much longer than inter-particle pores. Starting with a particle size of 0.3 micron alumina, Coble[17] found pores having a diameter of 5-10 microns at the onset of the final stages of sintering. Using 0.05 micron UO_2, Kingery[13] observed pores of 3-5 microns at the onset of the final stages of sintering. There are at least two explanations: (1) that many of these large pores existed in the original compact because of nonuniform particle packing and bridging between particle agglomerates and/or (2) that pore growth by volume diffusion or coalescence occurs. The phenomena of pore growth will be discussed later. At this point, it can be assumed that the large pores existing in the original compact may not be the sole cause of their observation, but it is at least one of the causes.

Figure 15 shows the various pore shapes that were randomly selected from high density compacts. This implies that a simple derivation of vacancy concentration from the average pore size would be impossible.

0 0 0 0 4 7 0 4 2 5 1

microstructure as observed by Greskovick.

Figure 14 consists of a series of pictures which show the evolution of an inter-agglomerate pore during the sintering process. The micrographs were not taken from the same area of one compact. However, since the powder processing was well standardized, they are considered to be representative for the evolution of a single inter-agglomerate pore. Two points of speculation should be considered. Firstly, the final pore geometry seems to be determined by the agglomerate packing in the original compact and, therefore, the complex pore shape can not be approximated as spherical as assumed in common models. Secondly, inter-agglomerate pores persist much longer than inter-particle pores. Starting with a particle size of 0.3 micron alumina, Coble[17] found pores having a diameter of 5-10 microns at the onset of the final stages of sintering. Using 0.05 micron UO_2, Kingery[13] observed pores of 3-5 microns at the onset of the final stages of sintering. There are at least two explanations: (1) that many of these large pores existed in the original compact because of nonuniform particle packing and bridging between particle agglomerates and/or (2) that pore growth by volume diffusion or coalescence occurs. The phenomena of pore growth will be discussed later. At this point, it can be assumed that the large pores existing in the original compact may not be the sole cause of their observation, but it is at least one of the causes.

Figure 15 shows the various pore shapes that were randomly selected from high density compacts. This implies that a simple derivation of vacancy concentration from the average pore size would be impossible.

0 0 0 0 0 1 4 7 0 0 1 2 5 5 2 2

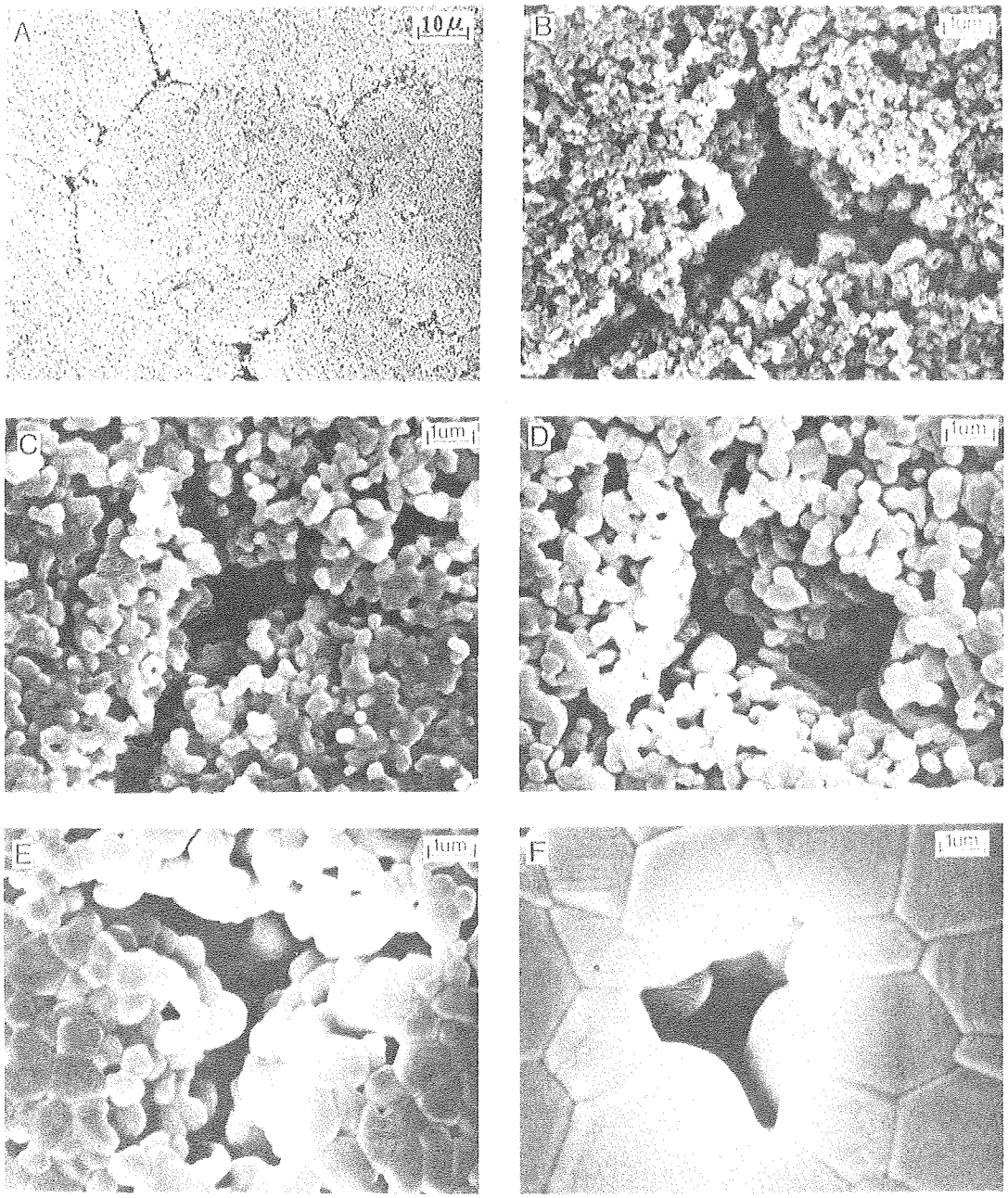

XBB768-7113

Fig. 14. Evolution of the inter-agglomerate pore during the sintering process.

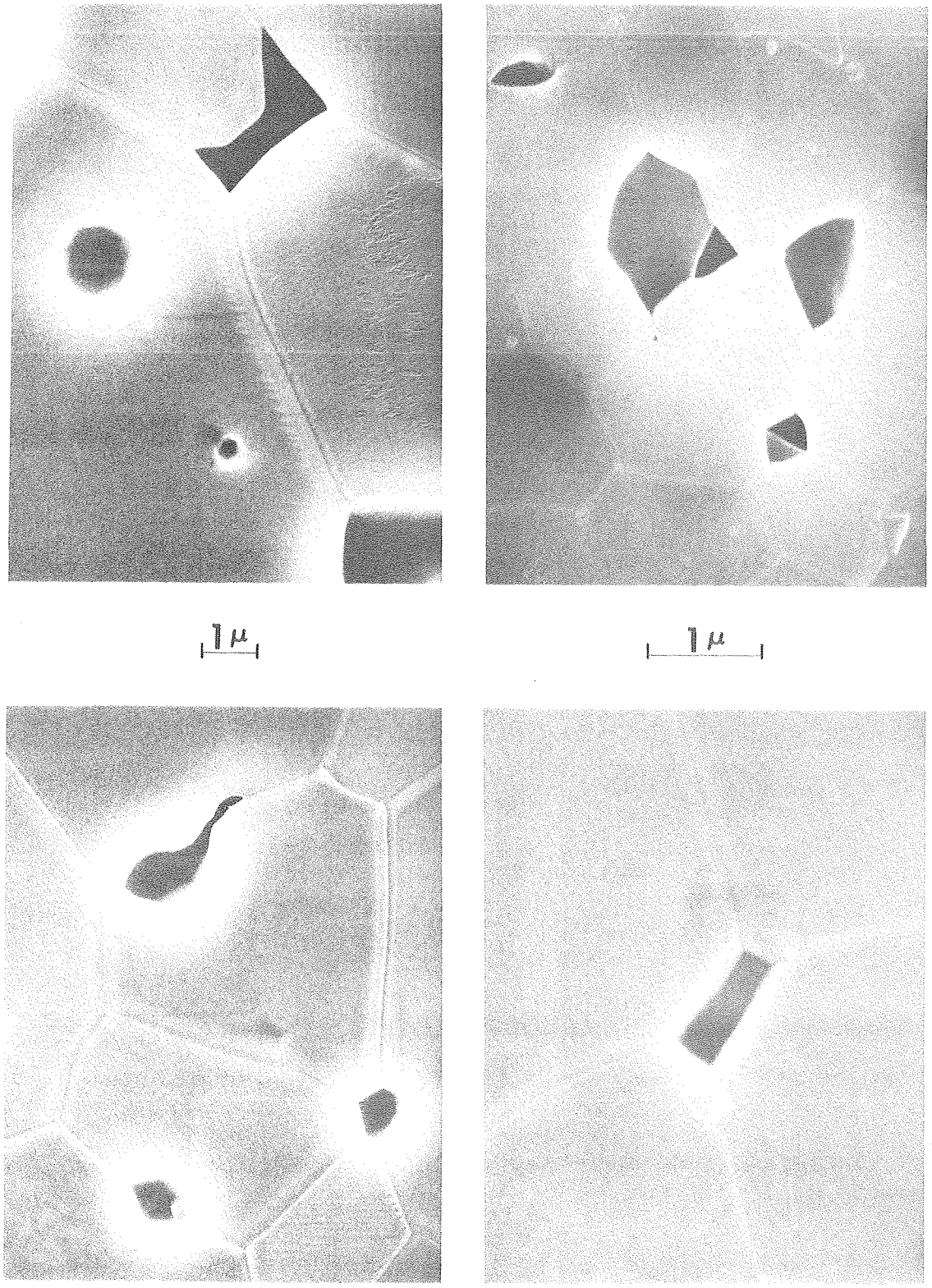

XBB768-7118

Fig. 15. Variations in pore shape in sintered compacts of high density.

0 0 0 0 0 0 4 7 0 0 0 2 3 5 5 3

In addition to the presence of agglomerates, density inhomogeneity is also important when discussing the effect of the green state on the sintering kinetics. The density variation caused by die wall friction during compaction will be referred to here as macro-inhomogeneity since this inhomogeneity will cause anisotropic shrinkage of the compact on a large scale. The type of inhomogeneity caused by the particle agglomeration will be referred to as micro-inhomogeneity. As discussed earlier, the presence of agglomerates causes local variations in pore size and distribution, but in the absence of uneven compaction, this variation will be the same everywhere throughout the compact. Therefore, the density of the compact can be considered as inhomogeneous microscopically and homogeneous macroscopically. A micro-inhomogeneous compact will not show an anisotropic shrinkage but its rate of densification will be different from that predicted by theory. The importance of local variations in pore concentration and size and their influence on the densification kinetics will be discussed later.

As described earlier, the hot stage scanning electron microscope allows the study of linear shrinkage of a compact in two dimensions. Therefore, this technique is able to demonstrate the effect of macroscopic homogeneity and inhomogeneity upon the linear dimensional change of a powder compact during sintering. A comparison was made by selecting one specimen near the edge and another near the center of a two inch diameter cold pressed pellet. The one near the edge (W-7) is considered to be macroscopically inhomogeneous since it was subjected to die wall friction. The one near the center (W-t) is considered to be macroscopically homogeneous since it was subjected to a uniform compaction

pressure. Results of these two sintering runs, in which the samples were heated at a rate of 4°C/min to temperatures of 1350°C and 1380°C, are shown in Fig. 16. After reaching the indicated temperatures, the samples were held isothermally. In both curves, every datum point is the average of nine individual shrinkage measurements. Sample W-5 showed isotropic shrinkage with little scatter in the data. The statistical scatter in the measurements indicates that sample W-7 was inhomogeneous in its shrinkage. Overlaying a magnified picture of the final marker positions on the picture of the original positions points this out dramatically. Although the two samples behaved differently in sintering, their mean average values of nine measurements at each point coincide very well.

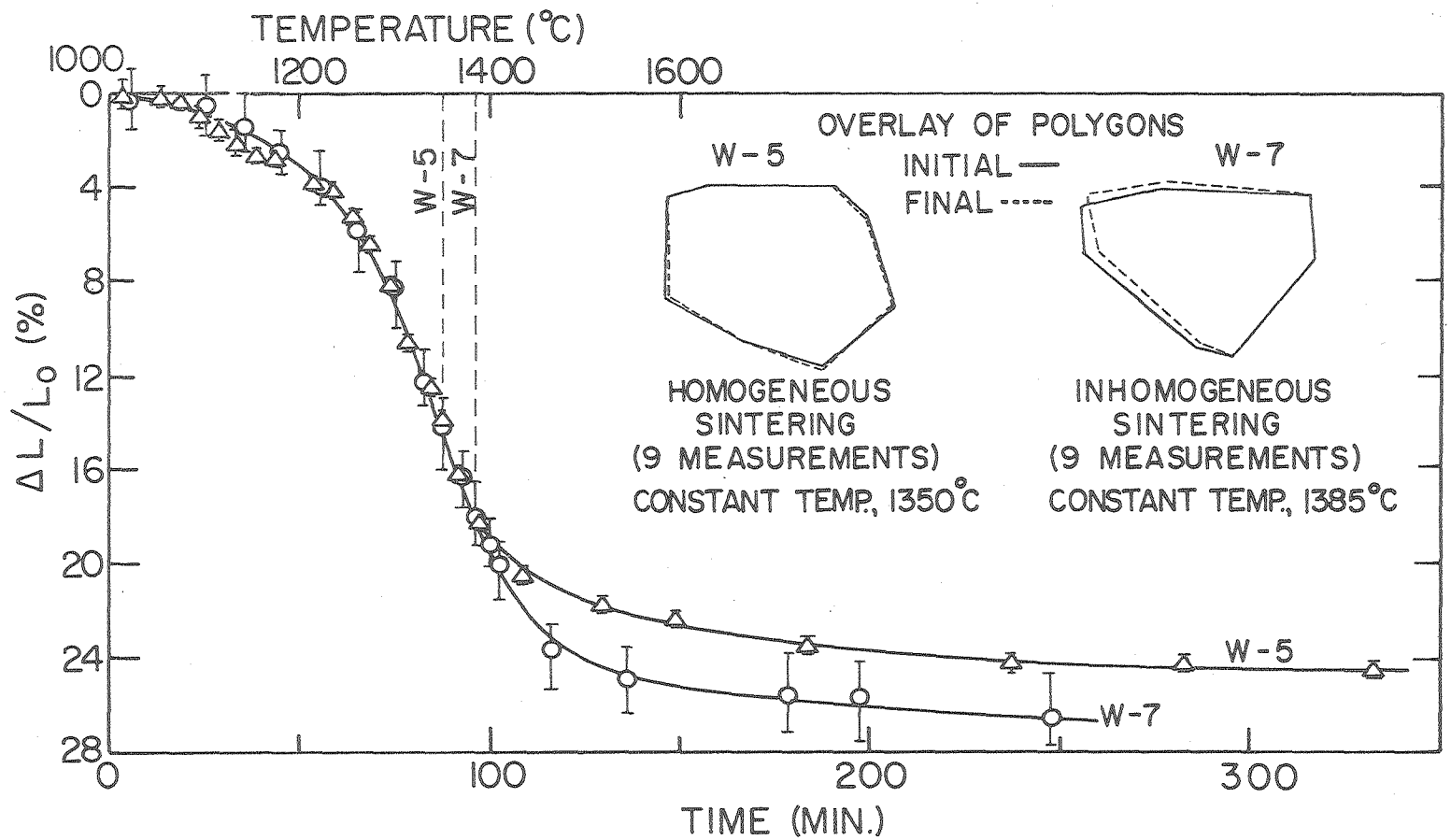

XBL742-5585

Fig. 16. Effect of macroscopic green density inhomogeneity on sintering behavior.

0 0 0 0 0 7 0 0 4 5 5 4

B. Initial Stage Sintering

Isothermal studies of linear dimensional changes of powder compacts in the initial stage have provided most of the available sintering data. Isothermal experiments present several problems, of which the most important is the inability to study the initial portion of the sintering process where the most rapid shrinkage occurs while thermal equilibrium is being established. In addition, stresses accompany the rapid heating necessary for isothermal sintering studies.

To circumvent these problems, sintering has been studied by measuring densification using a constant rate of heating (CRH) technique. In particular, Young and Cutler[41] have studied elutriated Alcoa A-14 aluminum oxide powders. They found that the CRH technique was extremely sensitive to the particle size distribution and other characteristics of the compacts. Because only one heating rate was used in their work, the sintering rate law could not be determined and, therefore, the true activation energy for sintering was not obtained. In studying UO_2 and ThO_2 gel, Woolfrey and Bannister[42] have obtained the sintering rate law by performing CRH experiments at different heating rates. By comparing results from isothermal experiments performed on the same materials, they have demonstrated the validity and accuracy of the nonisothermal technique.

Alcoa A-14 Al_2O_3 is generally considered as "dead burned" or "nonreactive" material while submicron size Al_2O_3 powders are generally considered as "reactive" materials. It was the main purpose of this work to compare the sintering behavior of these powders. In addition, a study of sintering behavior with variations in green compact density

0 0 0 0 0 4 7 0 0 2 3 5 5 5

was also made. This part of the study was done with Union Carbide powder in which only one heating rate was used. Figure 17 shows the pressed surfaces of the green compacts of four different powders. Compacts of submicron size powders from W. R. Grace, General Electric and Union Carbide Companies are shown in A, B, and C, respectively. A compact made of Alcoa A-14 powder, which is approximately 2.5 microns in size, is shown in Fig. 17D. Except for the Union Carbide powder, three or four heating rates were used. The fractional linear shrinkage vs. temperature plots for these powders during sintering are presented in Figs. 18, 19, 20 and 21.

The differential form of the initial stage sintering equation[10] is:

$$d\left(\frac{\Delta L}{L_o}\right)\Big/dt = K/\left(\frac{\Delta L}{L_o}\right)^{n-1} \tag{9}$$

The constants K and n depend on the geometry and the material transport mechanism. For the sintering of spherical particles, when the rate controlling mechanism is volume diffusion:

$$K = (1.95\gamma\Omega D_v/r^3kT) \text{ and } n = 2.0 \tag{10}$$

For grain boundary diffusion:

$$K = (0.48\gamma\Omega bD_b/r^4kT) \text{ and } n = 3.1 \tag{11}$$

where γ is the surface energy, Ω the volume of a vacancy, D the relevant diffusion coefficient, b the grain boundary width, k the Boltzmann constant, r the particle radius, and T the abosolute temperature. The temperature dependence of K can be represented by

$$K = K_o\exp\left(-\frac{Q}{RT}\right) \tag{12}$$

where K_o is proportional to $\frac{1}{T}$.

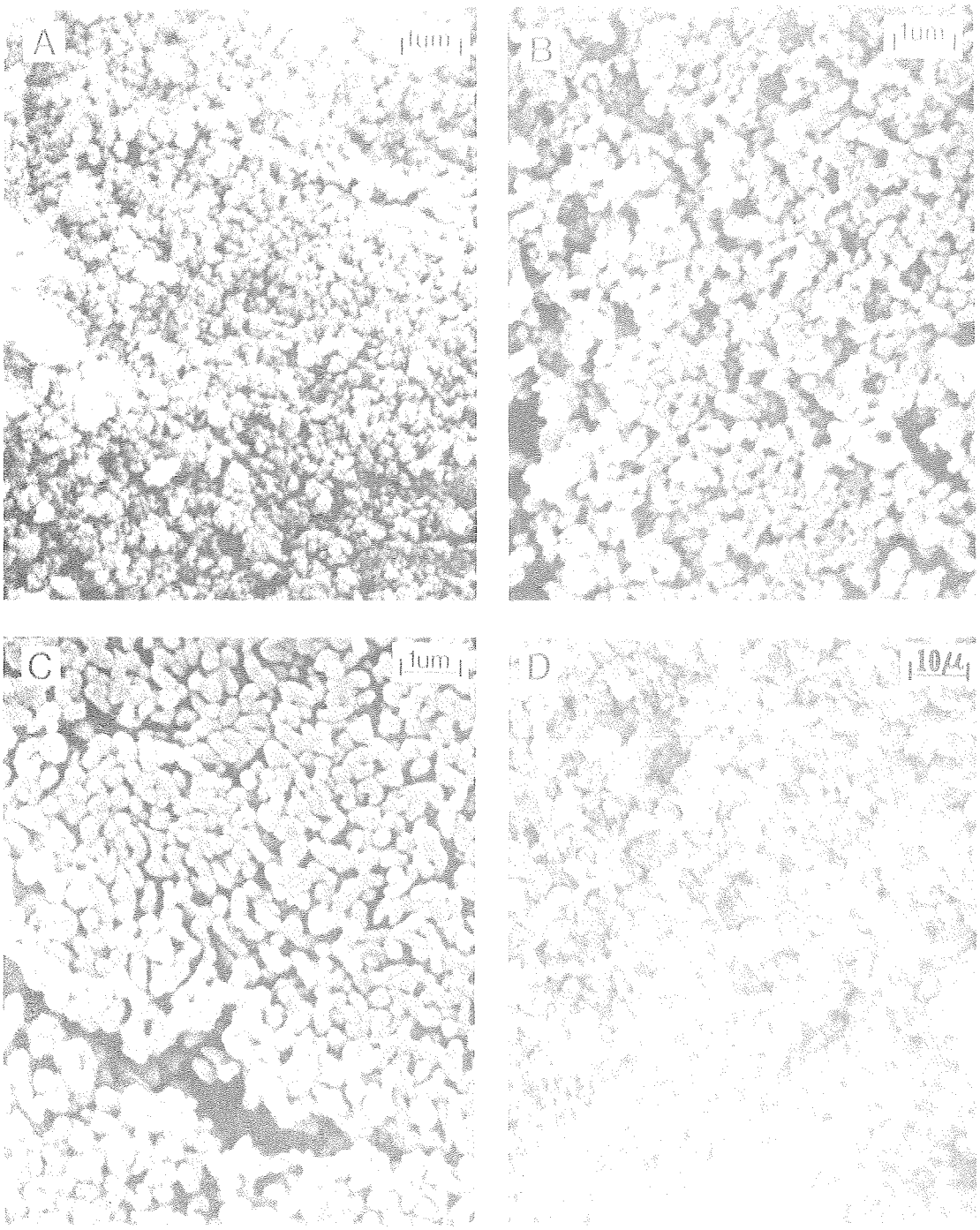

XBB768-7109

Fig. 17. Micrographs of pressed surfaces of Al_2O_3 green compacts of four different powders. (A) W. R. Grace Co., (B) G. E. Co., (C) Union Carbide Co., and (D) Alcoa A-14.

0 0 0 0 0 4 7 3 0 2 3 5 5 6

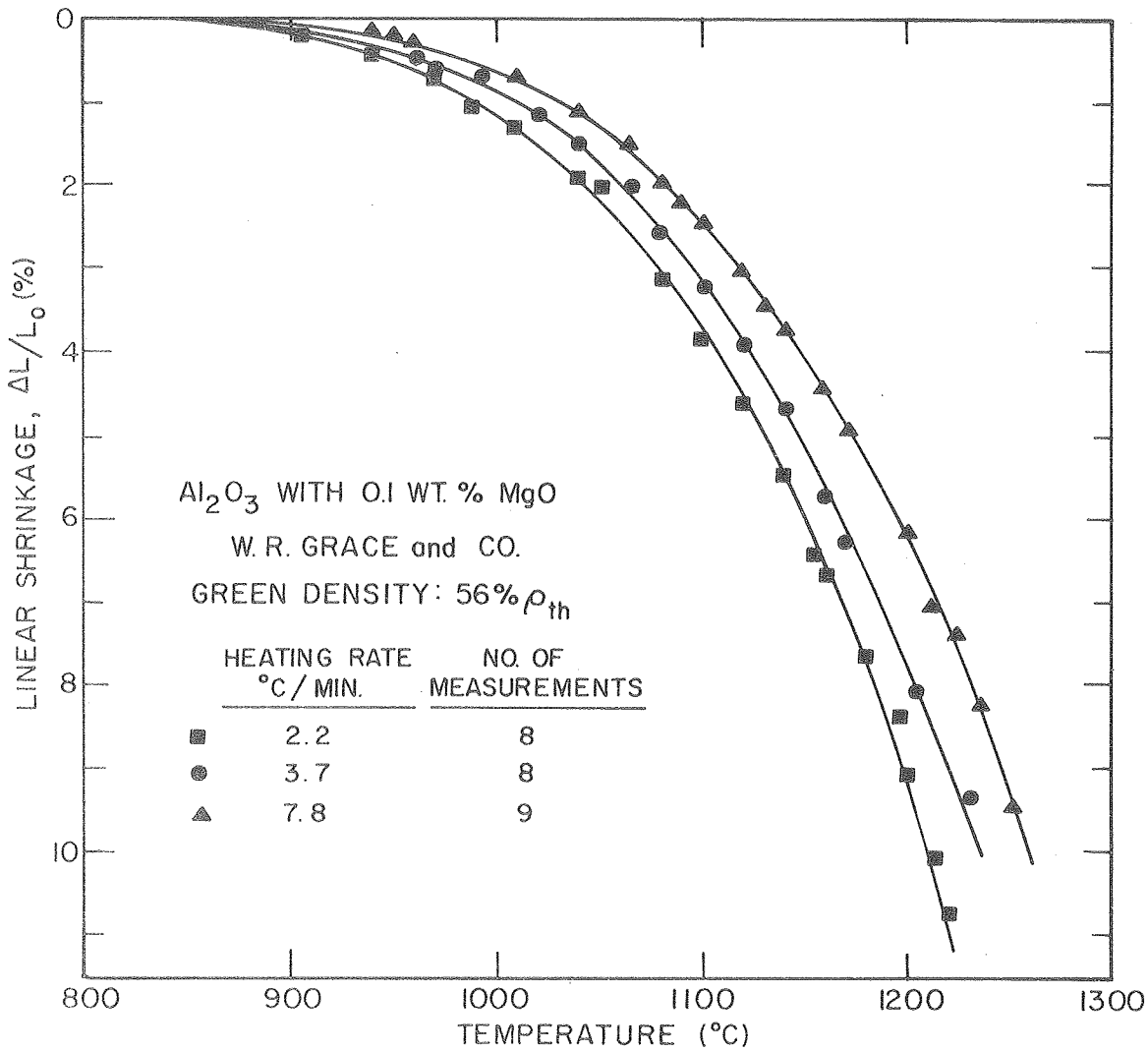

XBL 768-7339

Fig. 18. Densification profiles of W. R. Grace Al_2O_3 powder compacts at various constant heating rates.

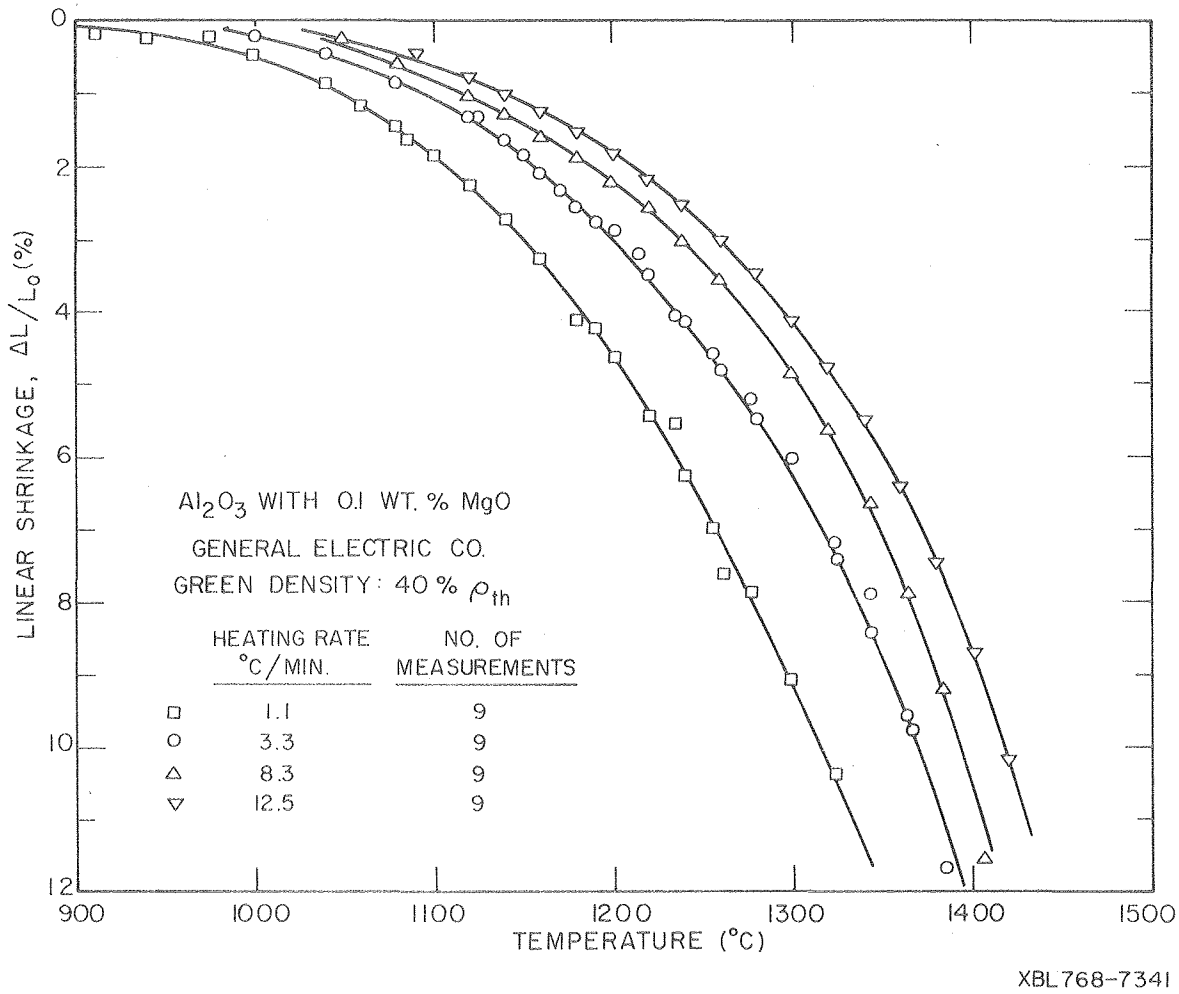

Fig. 19. Densification profiles of G. E. Al_2O_3 powder compacts at various constant heating rates.

0 0 0 0 0 0 4 7 0 0 4 0 2 5 5 7 7

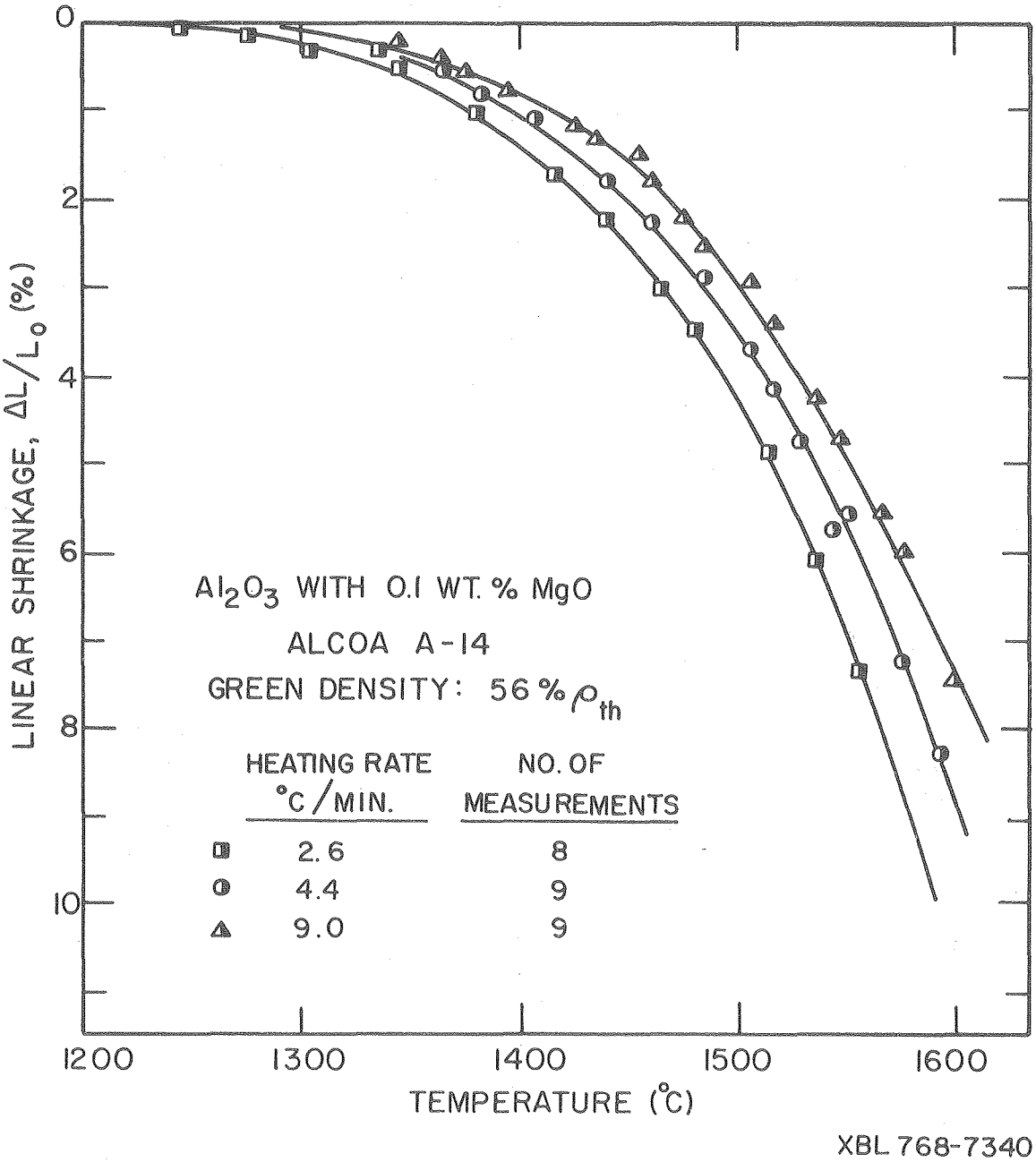

Fig. 20. Densification profiles of Alcoa A-14 Al_2O_3 compacts at various constant heating rates.

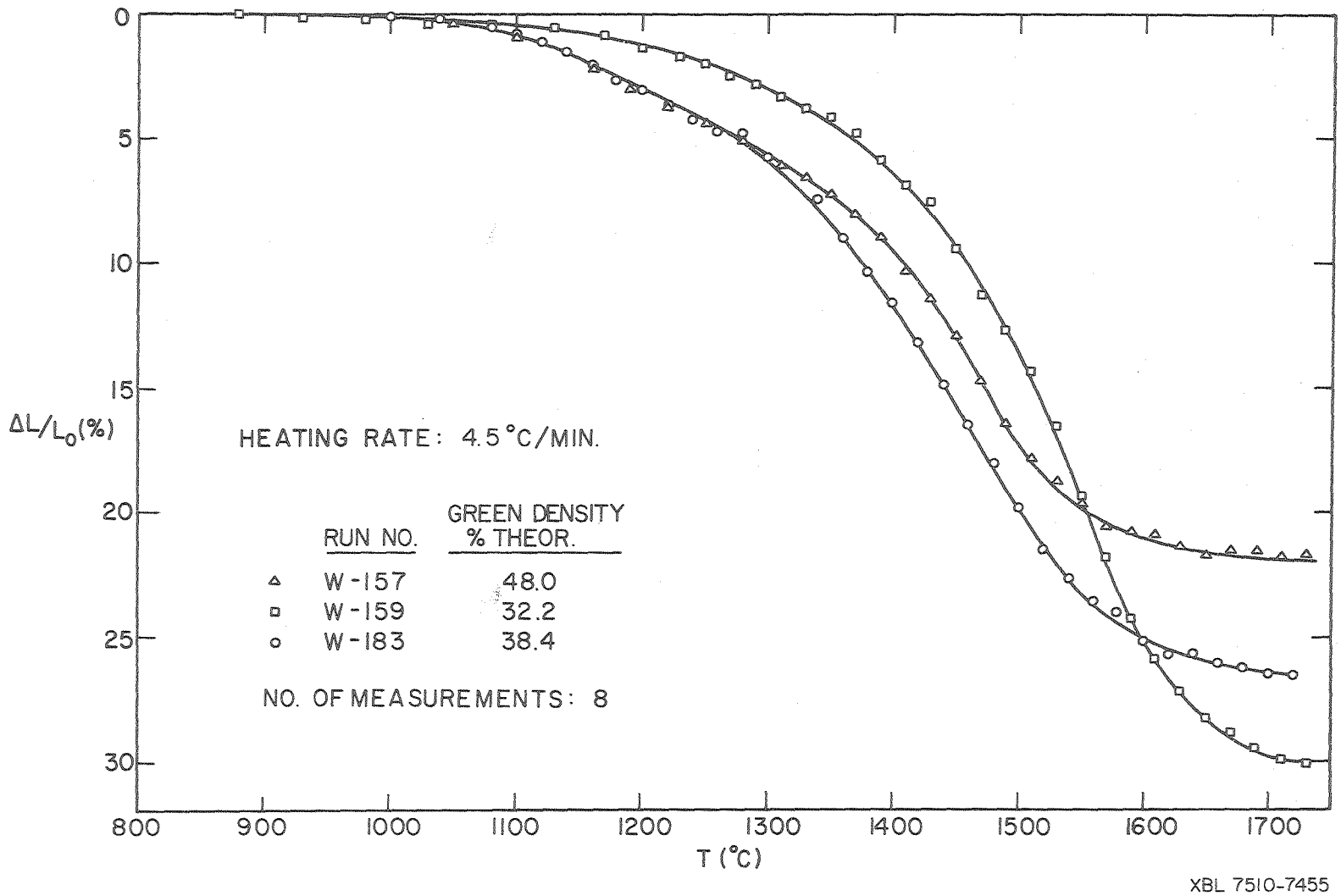

Fig. 21. Densification profiles of Union Carbide Al_2O_3 powder compacts with various green densities.

0 0 0 0 0 0 4 7 0 0 1 2 5 5 8 8

The equation, which applies to CRH conditions, is obtained from equations (9) and (12):

$$d\left(\frac{\Delta L}{L_o}\right)\Big/dt = \left[K_o \exp\left(-\frac{Q}{RT}\right)\right]\Big/\left(\frac{\Delta L}{L_o}\right)^{n-1} \tag{13}$$

This equation[10] is based on the assumption that, at any condition of shrinkage and temperature, the isothermal and nonisothermal shrinkage rates are equal. A mathematical proof can not be offered, but experimental evidence[42,43] has supported the assumption. After substitution of the constant heating rate, $a = \frac{dT}{dt}$, and rearrangement, equation (13) becomes:

$$a\left(\frac{\Delta L}{L_o}\right)^{n-1} d\left(\frac{\Delta L}{L_o}\right)\Big/dT = K_o \exp\left(-\frac{Q}{RT}\right) \tag{14}$$

If Q and n, which are characteristic of the rate controlling mechanism and, in the case of n, the geometry, remain constant:

$$\left(\frac{\Delta L}{L_o}\right)^n = \left(\frac{n}{a}\right)\int_o^t K_o \exp\left(-\frac{Q}{R\theta}\right) d\theta \tag{15}$$

Since Q >> RT equation 15 may be approximated by[44]

$$\left(\frac{\Delta L}{L_o}\right)^n = \left[K_o RT^2 \left(\frac{n}{aQ}\right)\right] \exp\left(-\frac{Q}{RT}\right) \tag{16}$$

Elimination of $\frac{\Delta L}{L_o}$ from equations (14) and (16) provides the shrink rate equation:

$$\frac{d\left(\frac{\Delta L}{L_o}\right)}{dt} = (K_o)^{\frac{1}{n}} \left[\frac{aQ}{RT^2 n}\right]^{\frac{n-1}{n}} \exp\left(-\frac{Q}{nRT}\right) \tag{17}$$

Substituting equations (12) and (13) provides the following equation:

$$T^2 \frac{d\left(\frac{\Delta L}{L_o}\right)}{dt}\Big/a = \left(\frac{Q}{nR}\right)\left(\frac{\Delta L}{L_o}\right) \tag{18}$$

Thus a linear-linear plot of $T^2 \, d\left(\frac{\Delta L}{L_o}\right)\Big/ a$ vs. $\frac{\Delta L}{L_o}$ should give a straight line with slope $\frac{Q}{nR}$. From this slope, the effective activation energy, $\frac{Q}{n}$ can be determined. From equation (16), a log-log plot of fractional shrinkage at a specific temperature vs. heating rate gives a straight line of slope $-\frac{1}{n}$. Substitution into $\frac{Q}{nR}$ then gives the apparent activation energy Q. Another way to obtain the value of $\frac{Q}{nR}$ is from simplified plots of the form $\ln\left(\frac{L}{L_o T}\right)$ vs. $\frac{1}{T}$ obtained from equation (16). This type of plot has been used by Young and Cutler[41] to determine the effective activation energy of A-14 Al_2O_3. In a real situation, transient shrinkage, caused either by the formation of new contacts between the particles or by particle sliding, will be included in the total shrinkage. This error can be minimized if the equation involving the derivative of shrinkage is used. Therefore, in the present work, a differential plot of shrinkage is preferred in determining the sintering kinetics.

Figure 22 gives the results for all the aluminum oxide powders. Two different slopes for each powder are noted. Equation (18) indicates that the plot should exhibit a single slope if (1) the material contains particles of a single size and (2) a single diffusion mechanism operates or if a combination of mechanisms with the same activation energy predominates over the entire initial stage sintering. A change in slope could be caused by a particle size distribution, a change in mass transport mechanism (assuming different activation energies), or by a change in the relative importance of competing mechanisms.

0 0 0 0 0 0 4 8 7 0 0 4 0 2 5 5 5 9 9

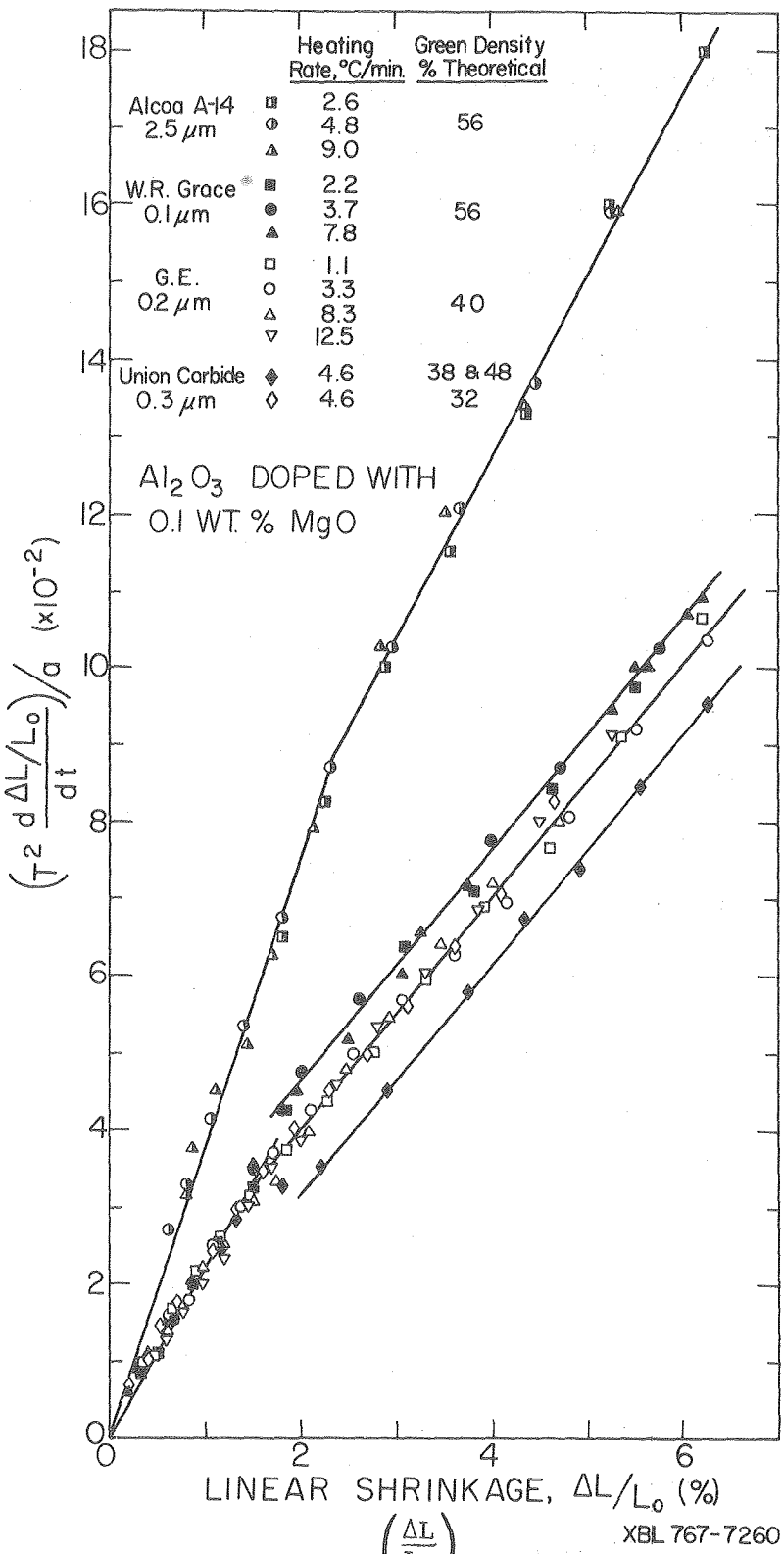

Fig. 22. Plot of $T^2 \frac{d\left(\frac{\Delta L}{L_o}\right)}{dt}$ a vs. $\frac{\Delta L}{L_o}$ for initial stage sintering of four different types of 0.1 wt% MgO-doped Al_2O_3 powder compacts with various constant heating rates.

Because the particle size distribution for the powders used in the present work is so narrow, it should not cause the slope to change. The problem of multiple mechanisms in sintering kinetics was treated by Johnson.[45] He has observed that low activation energy surface diffusion, acting in consort with grain boundary diffusion, results in an abnormally high apparent activation energy for densification. This situation has been described in detail by Cutler.[41] Surface diffusion generally has a low activation energy and it is expected to contribute to material transport at temperatures at or below the initial shrinkage temperature. If a neck is formed by surface diffused material, the flow of material from the grain boundary, which normally would be to the neck, is impeded until a temperature is reached at which flow from the grain boundary predominates. Because of the lengthened diffusion path and larger neck radius, the rate of shrinkage is retarded until the higher temperature is reached. As diffusion from the grain boundary overpowers surface diffusion, the former reaches the magnitude it would have reached if no surface diffusion had occurred. The net effect is a steepened initial slope. The independence of the slopes obtained in Fig. 22 with the heating rate indicates that surface diffusion as a competing mechanism is unlikely. The other mechanism that might be confused with surface diffusion is the volume-to-grain boundary changeover proposed by Johnson and Berrin.[46] These alternatives are difficult to distinguish.

The most remarkable thing found in this experiment is that the effective activation energies calculated from the slopes are different for A-14 Al_2O_3 powder and submicron size Al_2O_3 powders. The effective activation energy, $\frac{Q}{n}$, for A-14 powder is 75 Kcal/mole below 2.5%

0 0 0 0 0 0 4 7 0 0 1 2 5 5 0 0

fractional shrinkage and 42 Kcal/mole above 2.5%. These results give fairly good agreement with the effective activation energies of 83±10 and 38±3 Kcal/mole, respectively, obtained by Young and Cutler[41] who used an Arrhenius - type plot. The two effective activation energies calculated for the submicron size powders are 44 and 30 Kcal/mole with the break point at approximately 2% fractional shrinkage. Green density did not affect the sintering law or the effective activation energy as seen in Fig. 22. A decrease in green density, from 38 to 32% theoretical density, only led to progressively reduced rates of sintering.

Data obtained from Figs. 18, 19 and 20 are plotted in Figs. 23, 24, and 25 respectively, as the log shrinkage at a given temperature vs. log heating rate. In these three plots, the values of n calculated from the slopes indicate that n increases from ~1.5 and levels off at a value of 3. The dashed lines drawn in these figures represent the transitions between $n \neq 3$ and $n = 3$. The transitions between regions are not as apparent as the break points in slopes as seen in Fig. 22. However, they are consistent with the observed variations in effective activation energies over these ranges of temperature and shrinkage.

Because of the ambiguous nature of the lower portions of the kinetics in Fig. 22, further analysis will concentrate on the upper regions of the curves.

The value of $n(\approx 3)$ observed for the upper portions of the curves is that expected for grain boundary diffusion and indicates that this is probably the rate-controlling mechanism. The parameters γ and Ω in equation (11) were assigned the values 1,000 ergs/cm^2 and 10^{-23}cm^3, respectively. The particle sizes, r, were 0.1, 0.2, 0.3 and 2.5 microns

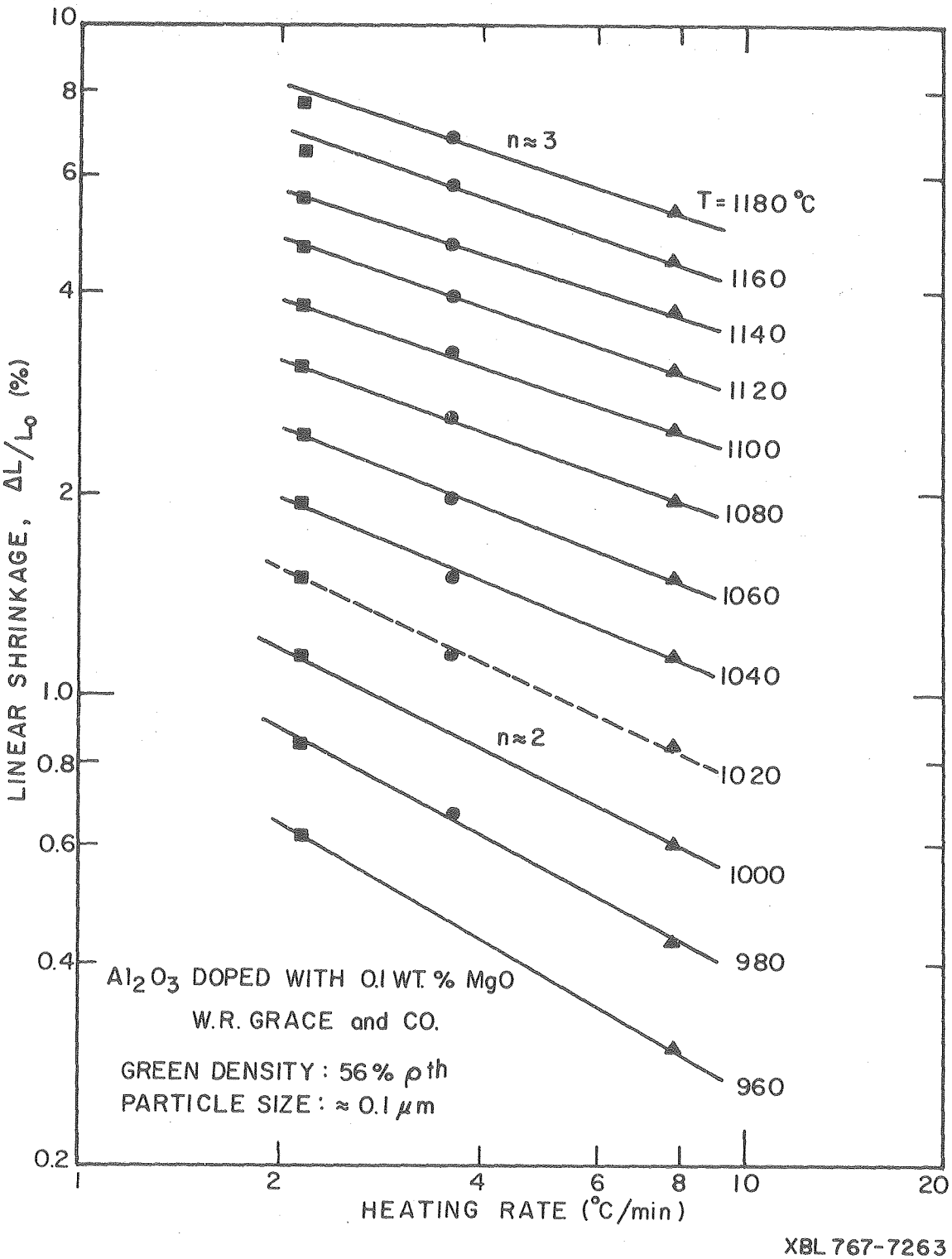

Fig. 23. Effect of heating rate on shrinkage at a specific temperature for initial stage CRH sintering of W. R. Grace Al_2O_3 powder compacts.

0 0 0 0 0 1 4 7 0 0 4 0 2 5 6 1 1

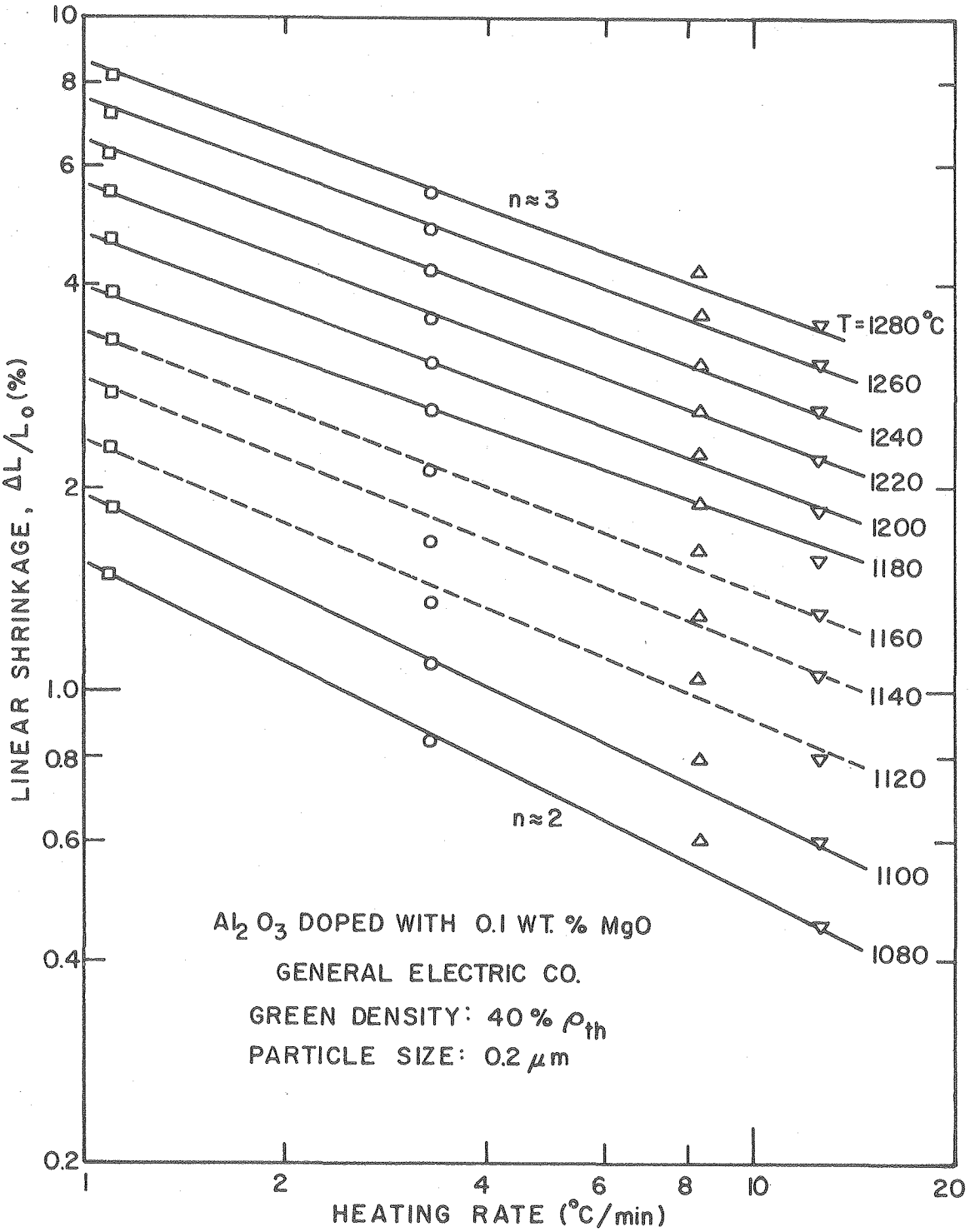

Fig. 24. Effect of heating rate on shrinkage at a specific temperature for initial stage CRH sintering of G. E. Al_2O_3 powder compact.

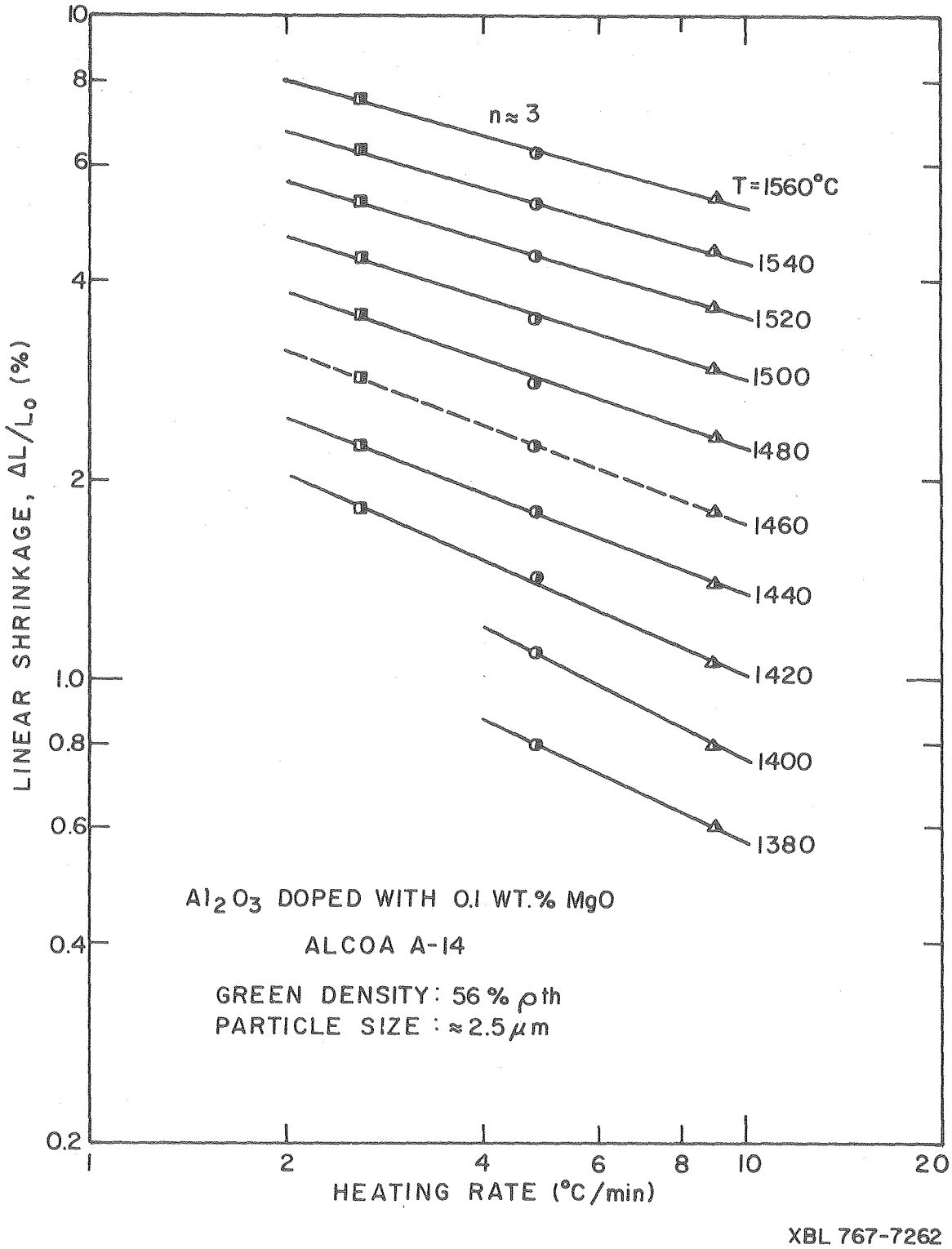

Fig. 25. Effect of heating rate on shrinkage at a specific temperature for initial stage CRH sintering of Alcoa A-14 Al_2O_3 powder compact.

0 00 0: 0 0 4 7 70 0: 2 3 6 2 2

for the W. R. Grace, General Electric, Union Carbide and Alcoa A-14 powders, respectively. The calculated diffusion coefficients by using equations (9) and (11) are shown in Fig. 26. Diffusion coefficients given by other sources[7.17.47.48.49] are also shown. The bD_b and D_v values are given on the same plot although they are not directly comparable. The discrepancy in the bD_b value calculated for Union Carbide powder from that of the other two submicron size powders may arise from difficulties in determining the actual particle size and/or from the differences in grain boundary width. The activation energy for the diffusion process obtained for all these submicron size powders has the same value of 93 Kcal/mole. This agrees very well with the value of 90 Kcal/mole that was observed by Chang[49] in his deformation experiments. However, the activation energy calculated for A-14 alumina is 165 Kcal/mole assuming grain boundary diffusion. This could be attributed to the lack of validity of equation (11) when applied to A-14 alumina powder. In fact, the particle shape of A-14 alumina very much deviates from the spherical shape assumed in using equation (11).

In studying the shape sensitivity of initial sintering, Bannister[10] found that n may be affected as much by the contact geometry as by the material transport mechanism. A value of n = 3 indicate either volume or grain boundary diffusion, depending on the geometry. For the pyramid-pyramid and pyramid-plane geometries, a value of n = 3 indicates that the rate controlling mechanism is volume diffusion. The factor K used in equation (9) is the same as that in equation (10) except that the numerical value changes with changing apex angle. Using 11.4 as the numerical value in equation (10), the calculated volume diffusion

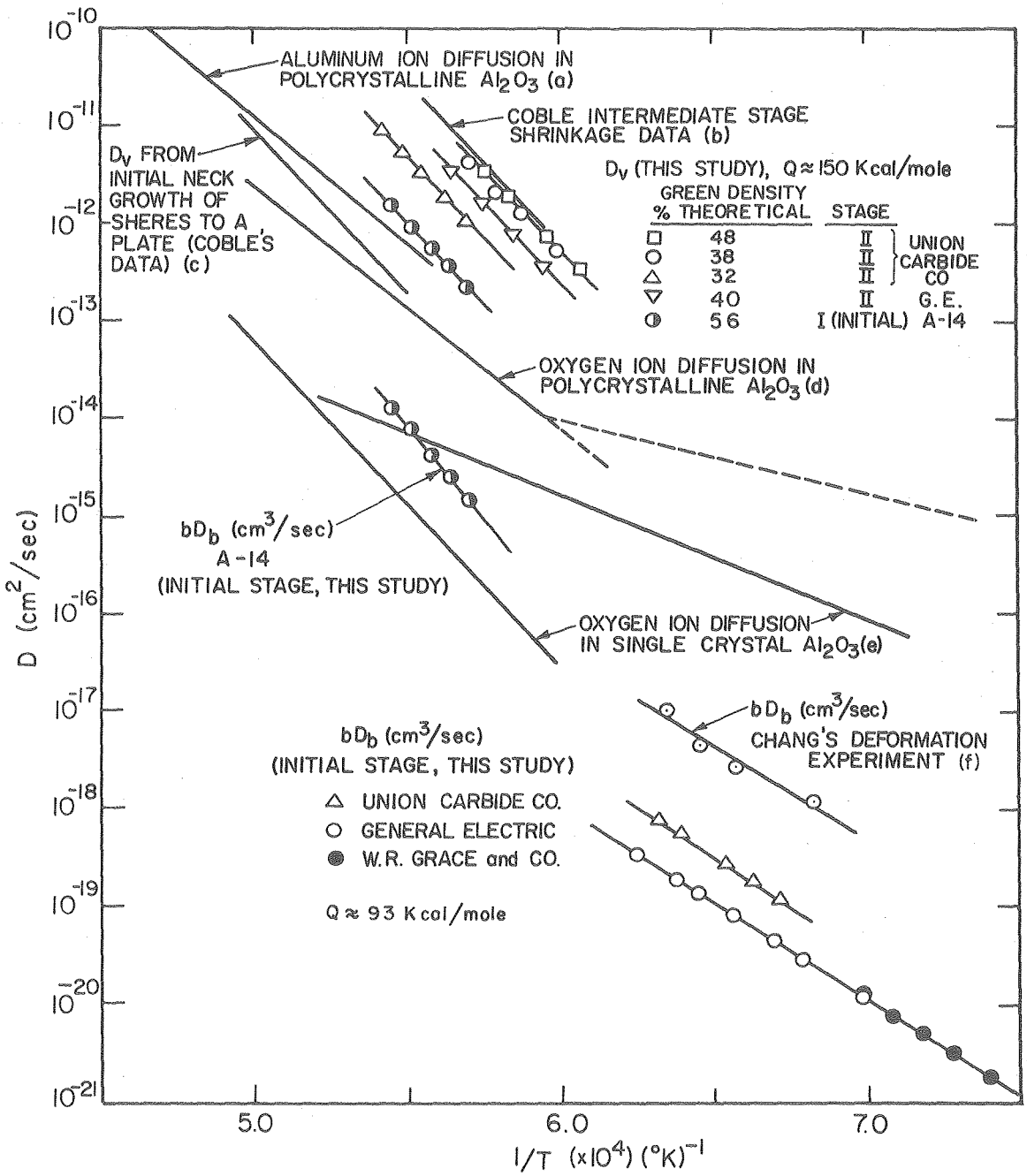

XBL 767-7264

Fig. 26. Diffusion coefficients calculated from initial stage and stage II sintering data compared with directly measured (tracer) values in Al_2O_3. (a) Ref. 47, (b) Ref. 17, (c) Ref. 7, (d)(e) Ref. 48, and (f) Ref. 49.

0 0 0 0 0 1 7 0 0 1 2 5 6 3

coefficients for A-14 alumina is plotted in Fig. 26. This result gives an activation energy of 150 Kcal/mole which is approximately the same as previous values obtained by assuming a volume diffusion mechanism.

With the absence of further evidence, it appears that in the initial stage sintering a grain boundary diffusion mechanism is responsible for mass transport in submicron size Al_2O_3 powder and a volume diffusion mechanism is responsible in Alcoa A-14 Al_2O_3 powder.

C. Post Initial Stage Sintering

1. Densification Kinetics

Powder compacts of different green densities were heated at various rates in the hot stage scanning electron microscope. In each run, the specimen was first heated to 800°C and then the temperature was increased to 1700°C or higher at a controlled rate. The fractional shrinkage was determined and the density was calculated by using equation (8). The relative density value was obtained by dividing this calculated value by the theoretical density value of 3.98. The change of density and densification rate with temperature and time were correlated with the microstructural evolution during the sintering process.

Figure 27 gives the change of relative density with temperature for four different heating rates using compacts with a green density of 40% of theoretical. Two runs were made for each heating rate in order to generate more accurate experimental results. As indicated by the curves, the slower the heating rate used, the higher the density at any given temperature. By measuring the tangent of the curve at a given temperature and by utilizing the equation $dT = adt$, the densification rate, $\frac{d\rho}{dt}$, can be determined for a particular temperature. The results are presented in Figs. 28 and 29.

Figure 28 shows that the densification rate increases with temperature to a maximum value and then decreases. The temperature at which this maximum value occurs depends on the heating rate used. Examination of densification rate versus relative density curves in Fig. 29 reveals that the maximum value occurs at the same relative density, about 0.74, which is independent of heating rate and temperature. The

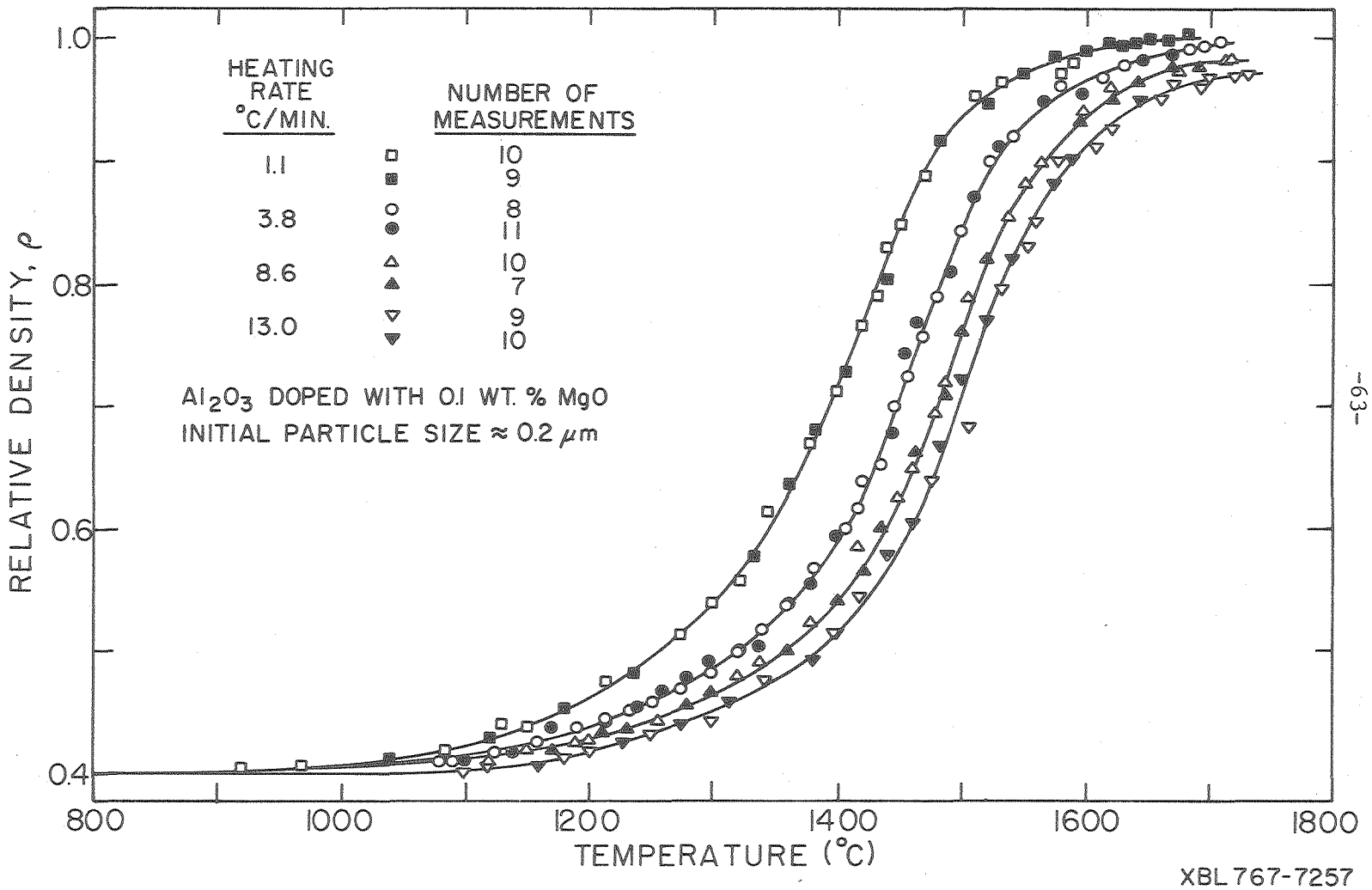

Fig. 27. The relative density of 0.1 wt% MgO-doped G.E. Al_2O_3 powder compact as a function of temperature for four constant heating rates.

0 0 0 0 0 0 1 7 0 4 2 5 6 4

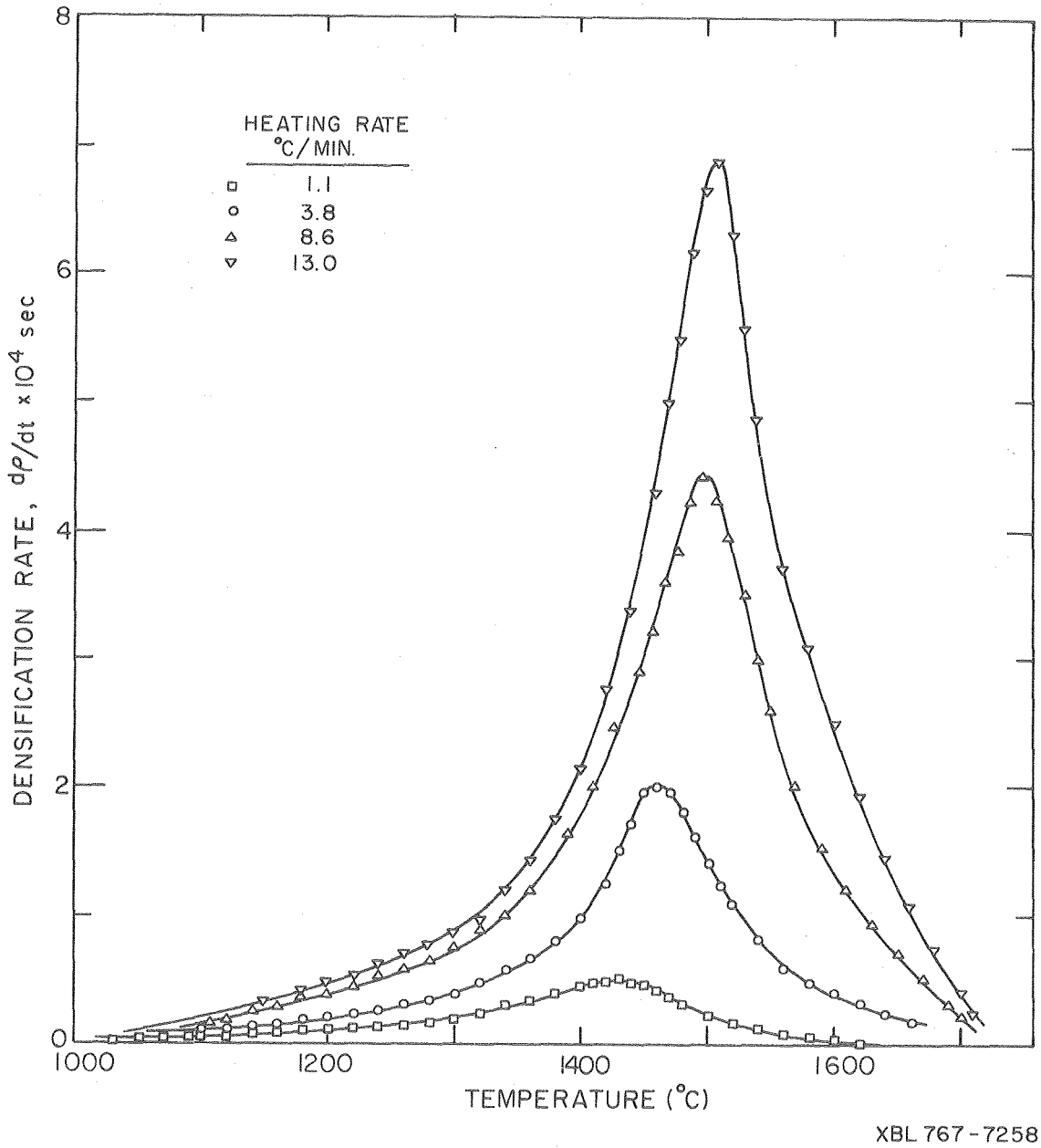

Fig. 28. The densification rate of MgO-doped G.E. Al_2O_3 powder compacts as a function of temperature.

0 0 0 0 0 1 4 7 0 0 2 5 6 5

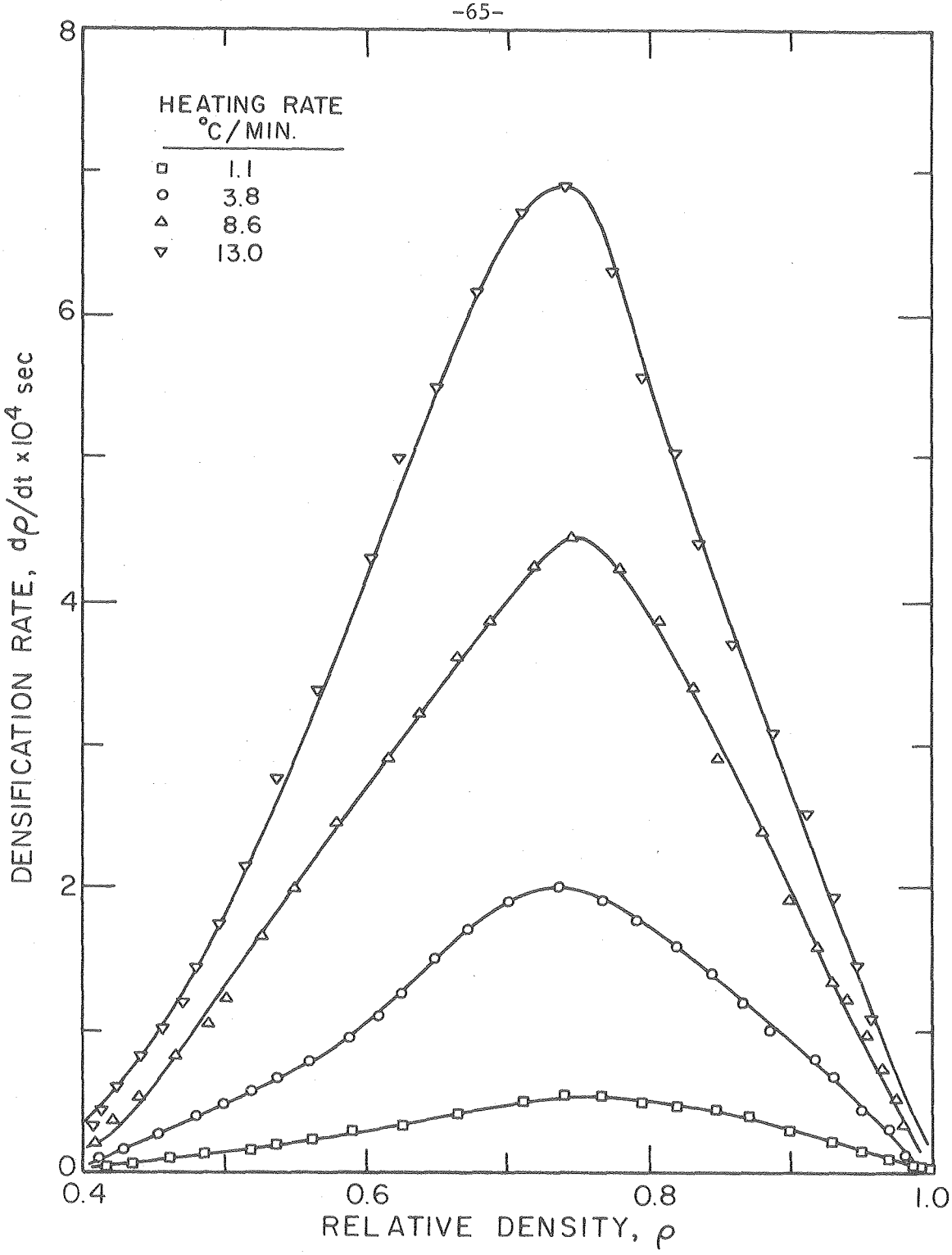

XBL 767-7259

Fig. 29. The densification rate of MgO-doped G.E. Al_2O_3 powder compacts as a function of relative density.

difference in the values of the maximum densification rate for different heating rates is attributed to the difference in temperatures at which the maximum rate occurs, as illustrated in Fig. 28. In this system, with a green density of 40% of theoretical, the critical density value, i.e., the relative density at which the maximum densification rate occurs, is approximately 73%. In a diffusion-controlled sintering process, densification of a compact is accomplished by a transfer of mass from grain boundaries to the surface of the pores due to a vacancy concentration gradient. If the densification proceeds only by the reduction of pore size, with no change in the grain structure and pore distribution, the densification rate should increase with increasing temperature since the diffusion coefficient is an exponential function of temperature. The occurrence of a maximum densification rate, therefore, indicates that there must be microstructural changes during the densification process, which are vital to the densification rate.

These changes can be generally divided into three categories: (1) evolution of grain structure, including changes of grain shape, size, and distribution (2) evolution of a pore phase, including changes of pore size, shape, and distribution, and (3) the change of the pore-grain boundary geometry. The combined effect of the grain structure evolution and the pore phase evolution on the densification rate will be discussed later. At this point, it is assumed that the major cause for the occurrence of a maximum densification rate at a constant relative density, independent of the heating rate used, is the distinct change of the pore phase. Therefore, it is expected that the maximum densification rate will shift to a different value of relative density as the green density

0 0 0 0 0 1 7 0 0 2 5 6 0

varies. A variation in green density will cause a change of particle packing, and as described in Section III-A, pore size and pore distribution are determined by the packing of particles in the powder compact.

Figure 21 shows the fractional shrinkage vs. temperature for three different green density compacts heated at the same constant heating rate. The coincidence of the curves up to 5% fractional shrinkage for the 38% and 48%-of-theoretical-density compacts indicates that the inter-particle pores are the same in the green compacts. The deviation observed for the rest of the curves indicates that the inter-cluster and inter-agglomerate pore sizes and distributions in these two compacts are different. The complete deviation of the curve for 32% green density compact from the other two indicates that not only the inter-cluster and inter-agglomerate pore phase but also the inter-particle pore phase is different. The results on the relative density vs. temperature and the densification rate vs. relative density for these compacts are presented in Figs. 30 and 31. Figure 31 shows that the occurrence of the maximum densification rate shifts toward a higher relative density value as the green density of the compact increases. The corresponding values of the relative density for the maximum densification rates are 68%, 72%, and 78% for 32%, 38% and 48% of theoretical density green compacts, respectively. Because small pores disappear first, the larger number of small pores in a high green density compact will, therefore, lead to a higher density before the densification rate starts to decrease.

Figure 32 gives further confirmation of the fact that the critical density (1) is not affected by the heating rate used as long as the green density is kept constant and (2) increases with increasing green

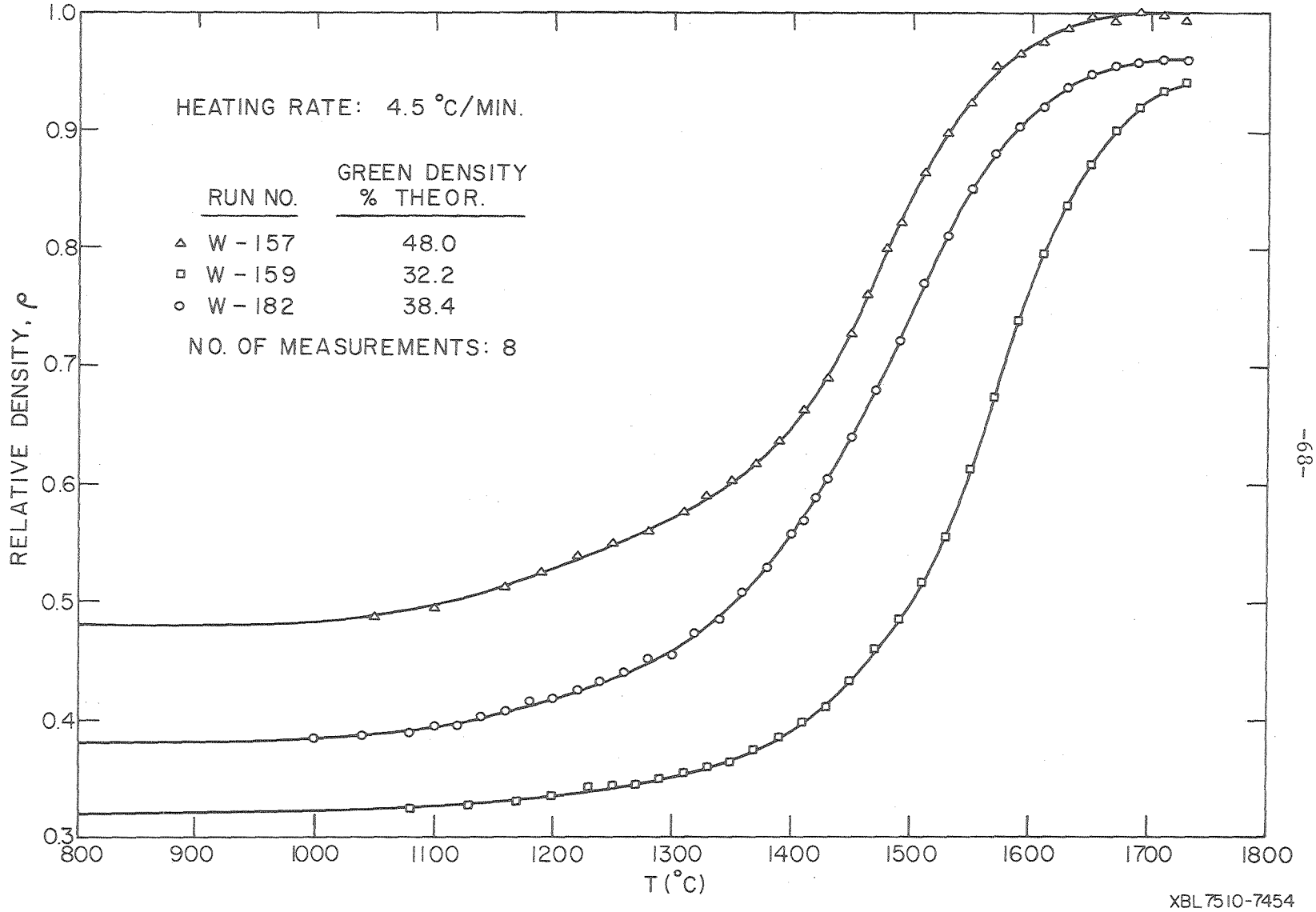

Fig. 30. Relative density vs. temperature for 0.1 wt% MgO-doped Union Carbide Al_2O_3 powder compacts with various green densities heated at a constant rate of 4.6°C/min.

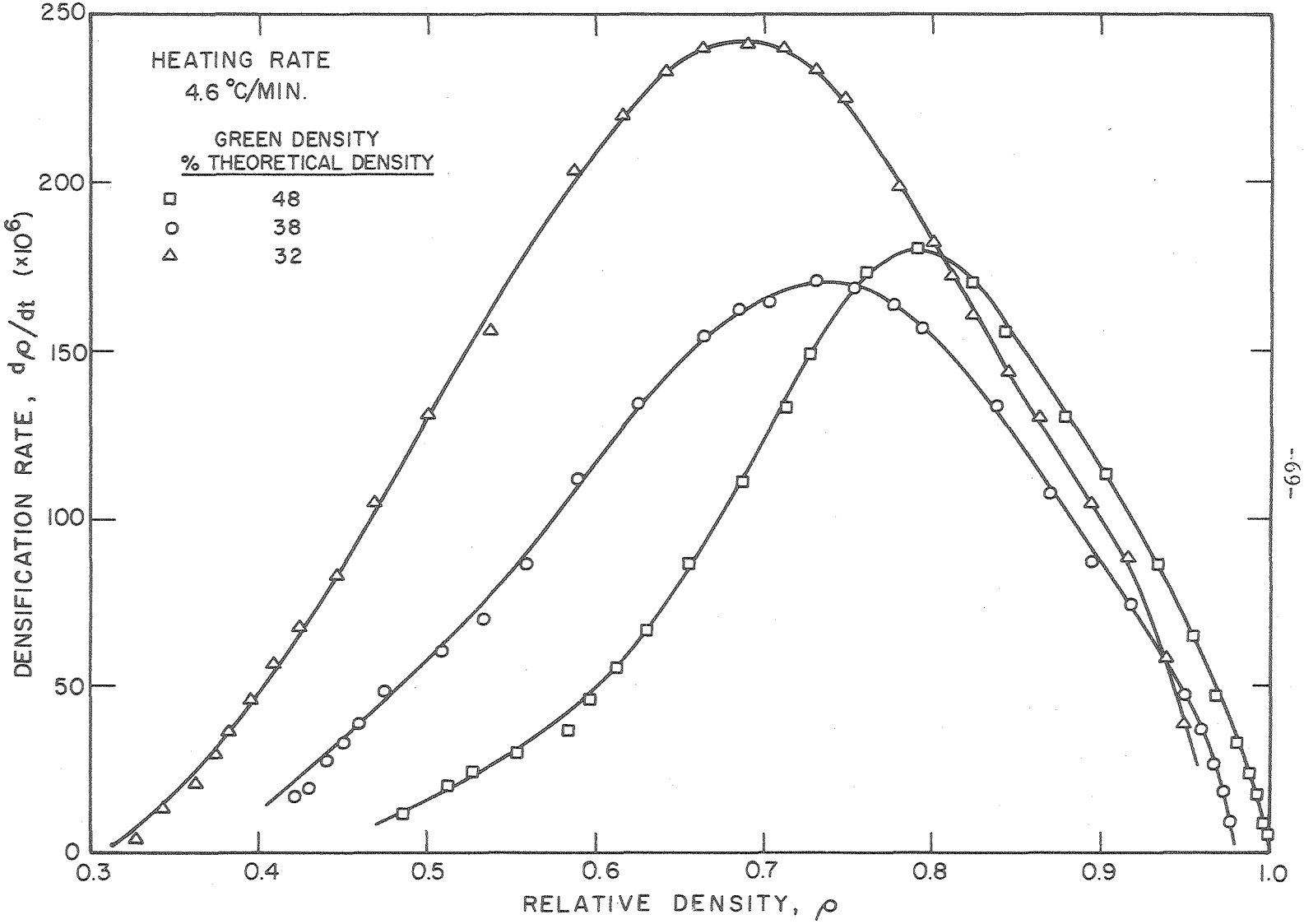

Fig. 31. Densification rate vs. relative density for MgO-doped Al_2O_3 powder compacts with various green densities heated at a constant rate of 4.6°C/min.

0 0 0 0 7 2 0 1 2 6 3 7

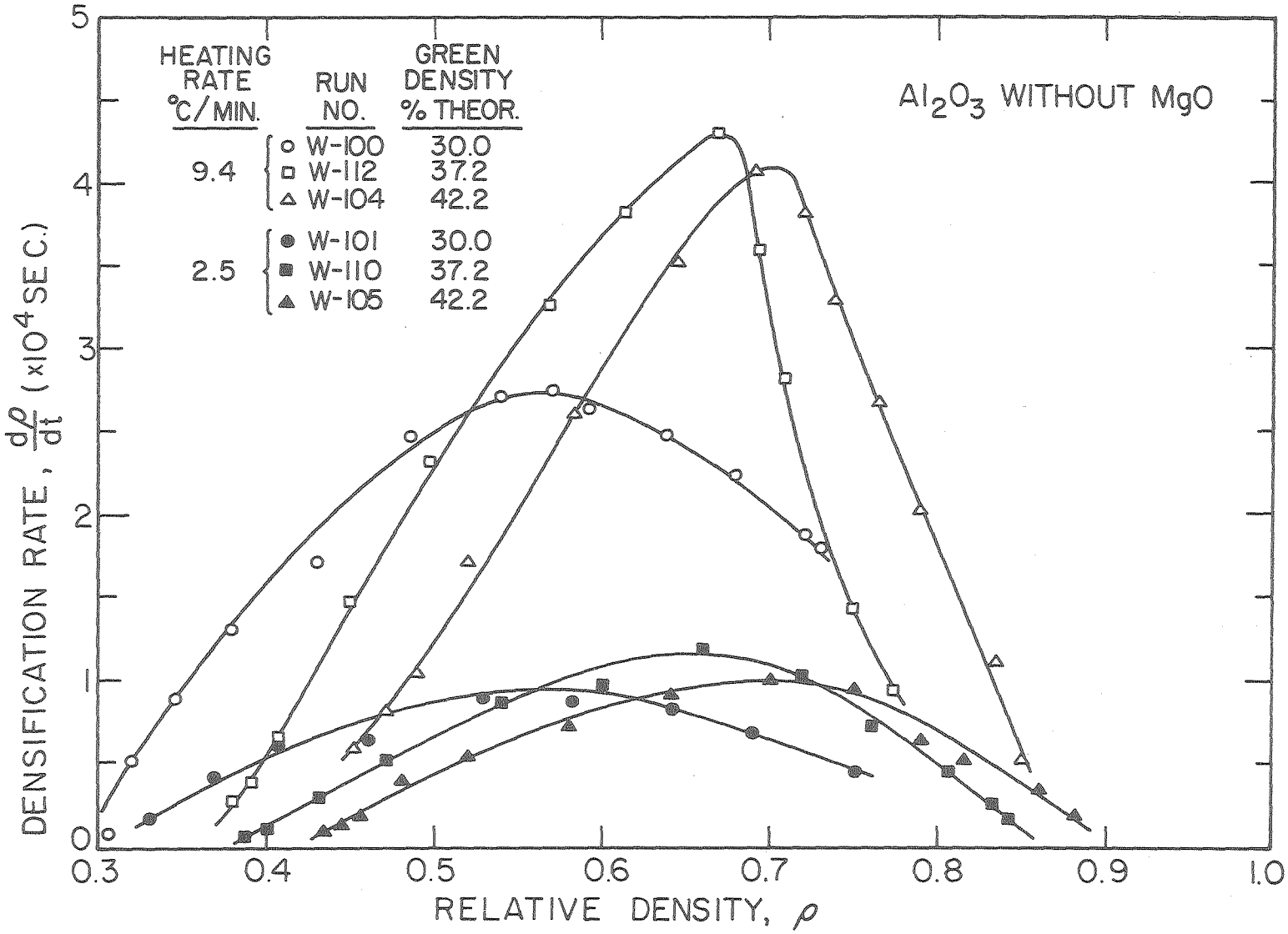

XBL 749-7323

Fig. 32. Densification rate vs. relative density for undoped Al_2O_3 powder compacts with various green densities heated at two constant heating rates.

0 0 0 0 4 7 0 3 2 5 8 8

density. In this study, the critical densities are 55%, 67% and 70% of theoretical for green compacts of 30%, 37.2% and 42.2% of theoretical, respectively. However, the observed critical densities are lower than would be anticipated from the results in Fig. 31. For example, the 42.2% green density sample in Fig. 32 has a lower critical density value (70%) than the 38% green density sample in Fig. 31 (72%). Although the absence of MgO as a dopant is one difference between the samples used to generate the results of Figs. 31 and 32, this is not considered to be the reason for the above mentioned discrepancy and this point will be illustrated in a later section. Instead, the lower critical density values are attributed to the difference in the initial powder compaction. The results presented in Fig. 31 were made with compacts which were isostatically pressed, while those presented in Fig. 32 were made with compacts which were uniaxially pressed. Compacts pressed uniaxially result in lower green density in the diametrical direction than in the pressing direction. Therefore, the relative density values were determined from a section of the sample with a lower green density than that of the overall specimen. This explains the discrepancy between Figs. 31 and 32.

Further evidence of the effect of the evolution of pore phase on the densification rate can be obtained by examining the development of microstructure of compacts during sintering. Figure 33 consists of six microphotographs which were taken from polished surfaces of fired compacts. These 40% green density compacts were heated at a rate of 4.6°C/min from 800°C until the desired densities were achieved and then they were cooled by quenching. The number appearing on the upper left hand corner of each photograph represents the value of relative density. It

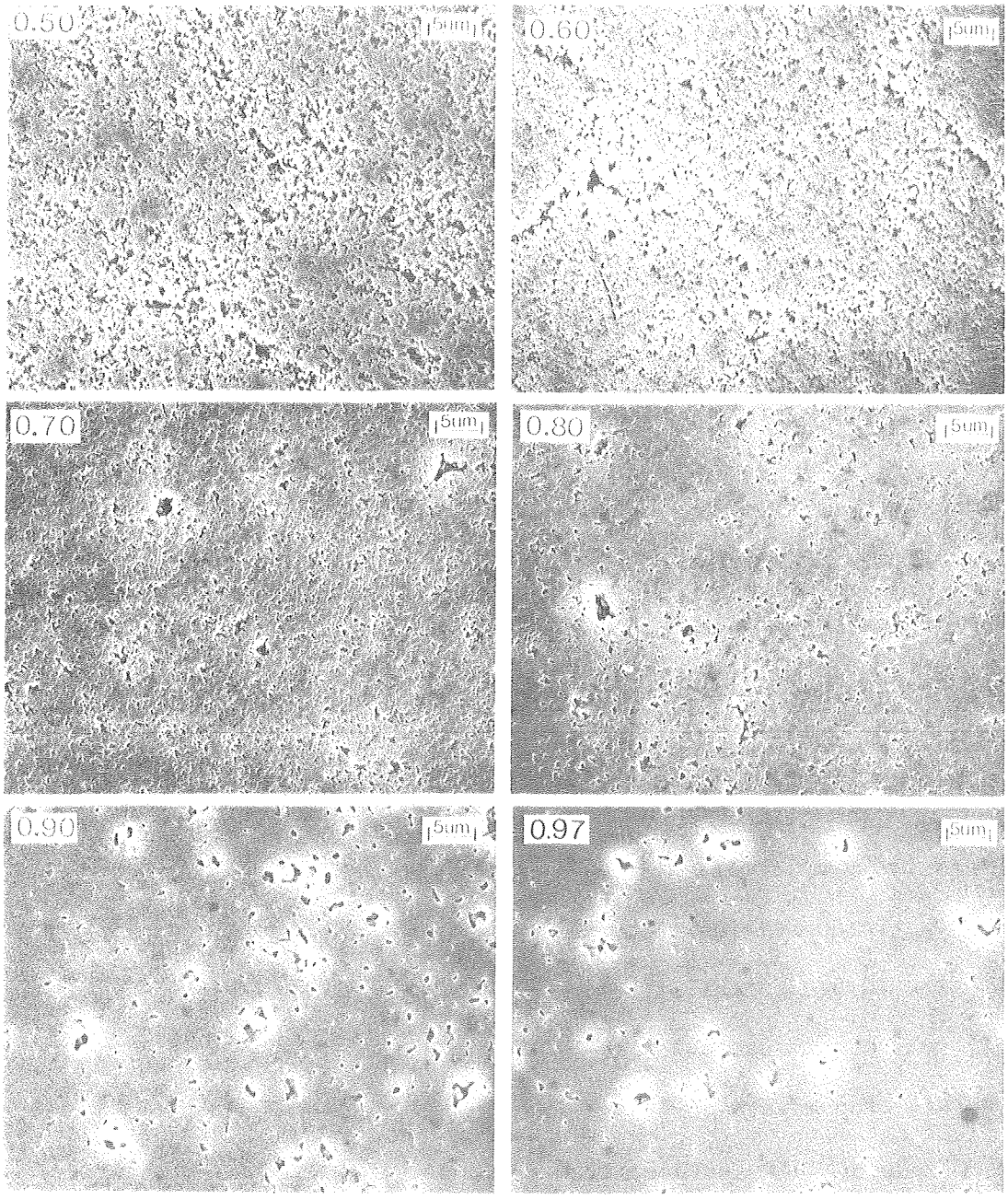

XBB768-7114

Fig. 33. Evolution of the pore phase of MgO-doped G. E. Al_2O_3 (40% green density) powder compacts sintered at a rate of 4.6°C/min. The number appearing on the upper left hand corner of each photograph represents the value of relative density.

0 0 0 0 4 7 0 0 2 6 8 9

is apparent that the average pore size increases and the number of pores decreases as density increases. This can be explained in terms of the existence of a bimodal or even trimodal pore size distribution in the initial powder compact, as described in Section III-A. As sintering proceeds, the pore size distribution will gradually shift to a large pore size through the elimination and reduction in size of small pores. This shift, of course, leads to larger average pore size and a reduction in total number of pores as density increases. By examining the shape and geometry of the large pores in the final microstructure (0.97) and by tracing their history back to the low density microstructures, it appears that these large pores result directly from the inter-agglomerate pores in the green compact rather than as a result of pore growth. A further study on the subject of pore growth will be presented later.

Figure 33 illustrates a transition region between 70% and 80% relative density in terms of the uniformity of the distribution of inter-particle and inter-cluster pores. (The inter-agglomerate pores are excluded from this observation since the high magnification (2000X) used for these photographs allows coverage of only a few agglomerates.) Microstructure developed at or below the relative density of 70% have a fairly uniform distribution of pores since densification to this point is due mainly to reduction in size and elimination of inter-particle pores and reduction in size of inter-cluster pores. Microstructure developed at or above the relative density of 80% do not have a uniform distribution of pores. In this stage of sintering, densification results mainly from a reduction in size of inter-cluster and inter-agglomerate pores as well as the elimination of some inter-cluster pores.

As described earlier, there is a size distribution for inter-cluster pores and therefore, after the elimination of small inter-cluster pores, large inter-cluster pores are left resulting in a non-uniform porosity distribution.

The non-uniform distribution of pores, i.e., the local variation in pore concentration, is usually more important than the range of pore size as far as the rate of densification is concerned. This results from the fact that pores in the porous region are restrained from shrinkage by the dense region. Transfer of material from grain boundary to pores leads to a normal tension on the boundary. This lower chemical potential gradient for diffusion restricts further mass transport. Relief of these differential strains is necessary before densification can continue. It is supposed that this local variation in pore concentration and the increase in average pore size are the reasons that the densification rate becomes highly density dependent. The occurrence of the maximum densification rate at a relative density of 73% (Fig. 29) coincides with the occurrence of a transition state (between relative densities of 70% and 80% in Fig. 33) concerning uniformity of pore concentration.

In addition to the evolution of pores the evolution of grain structure and pore-grain boundary geometry are also important to densification kinetics. Grain size is generally considered as a parameter which characterizes the diffusion path length for mass transfer during sintering. A change of grain size will change the rate of densification. The site and size of a pore relative to the boundary network affects both the distance for diffusion and the driving force for the process.

Scanning electron microphotographs taken from polished and subsequently etched surfaces of compacts which were heated at the same rate of 4.6°C/min from a 40% green density to different densities are shown in Fig. 34. In order to obtain more representative pictures, only areas inside agglomerates were selected and, therefore, the pores shown in these pictures include only inter-particle and inter-cluster pores. Several features should be noted: (1) the grain (particle) size increases as density increases and considerable grain growth has occurred even at the very early stage of sintering; (2) all the pores either intersect grain boundaries or are located in four grain corners, depending on the initial particle packing; (3) the shape of the grains (particles) changes as sintering proceeds: initially, the particles appear to be chain-like (Figs. 34B and C), then to be oblong (Fig. 34D), and, finally, to be equiaxed (Figs. 34E, F, G and H); (4) the local variation in pore concentration allows the growth of particles in the dense region and results in a broader grain size distribution as compared with that in the low density microstructures. In accordance with the change of particle shape and pore concentration as shown in Fig. 34, a transition region occurs between relative densities of 70% to 75% which again agrees quite well with the density found for the occurrence of the maximum densification rate.

A study of the heating rate effect on microstructural evolution is required before any further quantitative analysis of the densification kinetics is possible. Scanning electron micrographs of compacts of the same relative density obtained by heating at rates of 1.1, 3.8, 8.6 and 13°C/min are shown in Figs. 35, 36 and 37 for the relative

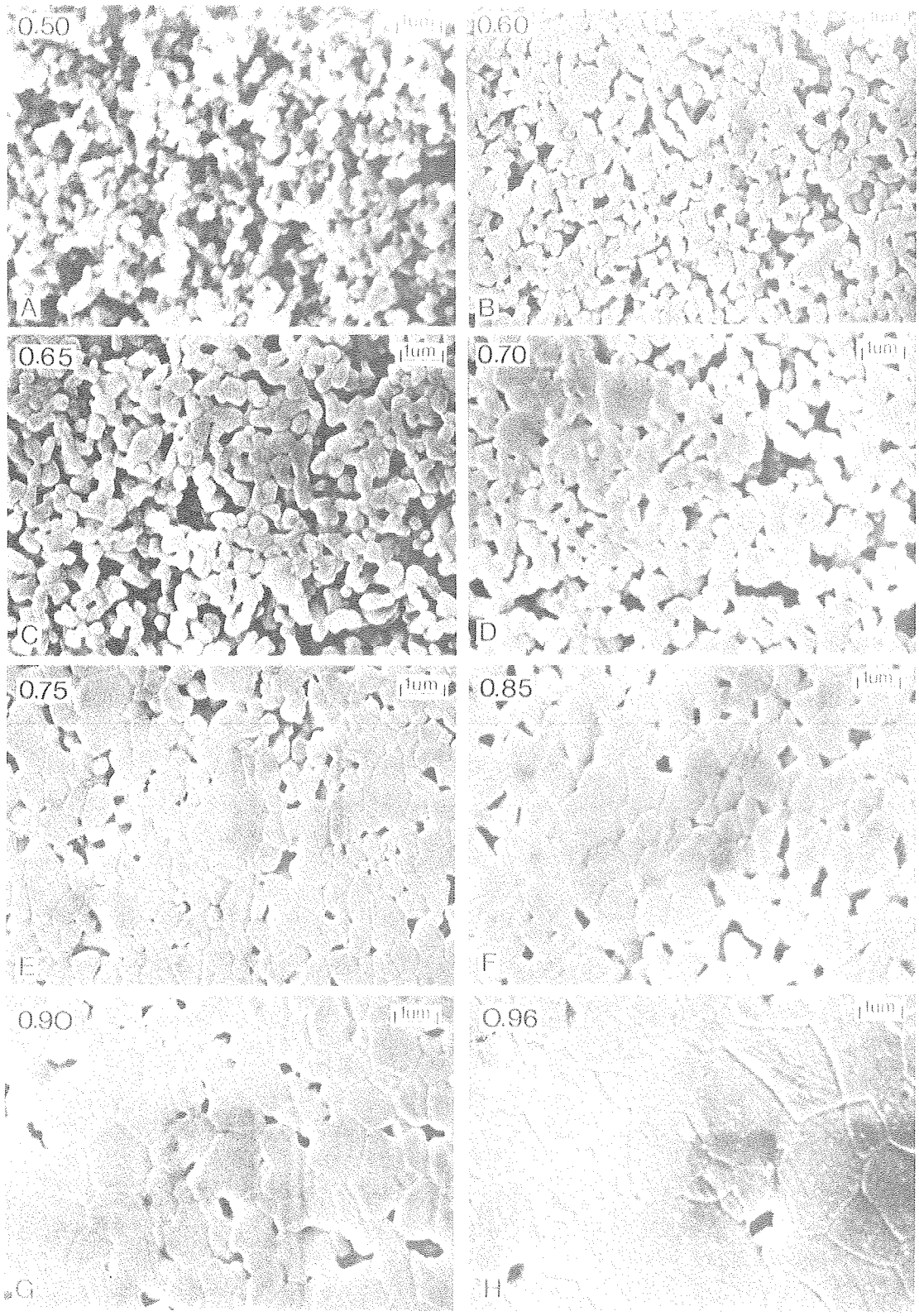

XBB768-7102

Fig. 34. Evolution of the microstructure of MgO-doped G. E. Al_2O_3 (40% green density) sintered at a constant rate of 4.6°C/min. The number appearing on the upper left hand corner of each photograph represents the value of relative density.

0 0 0 0 4 7 0 0 2 9 1

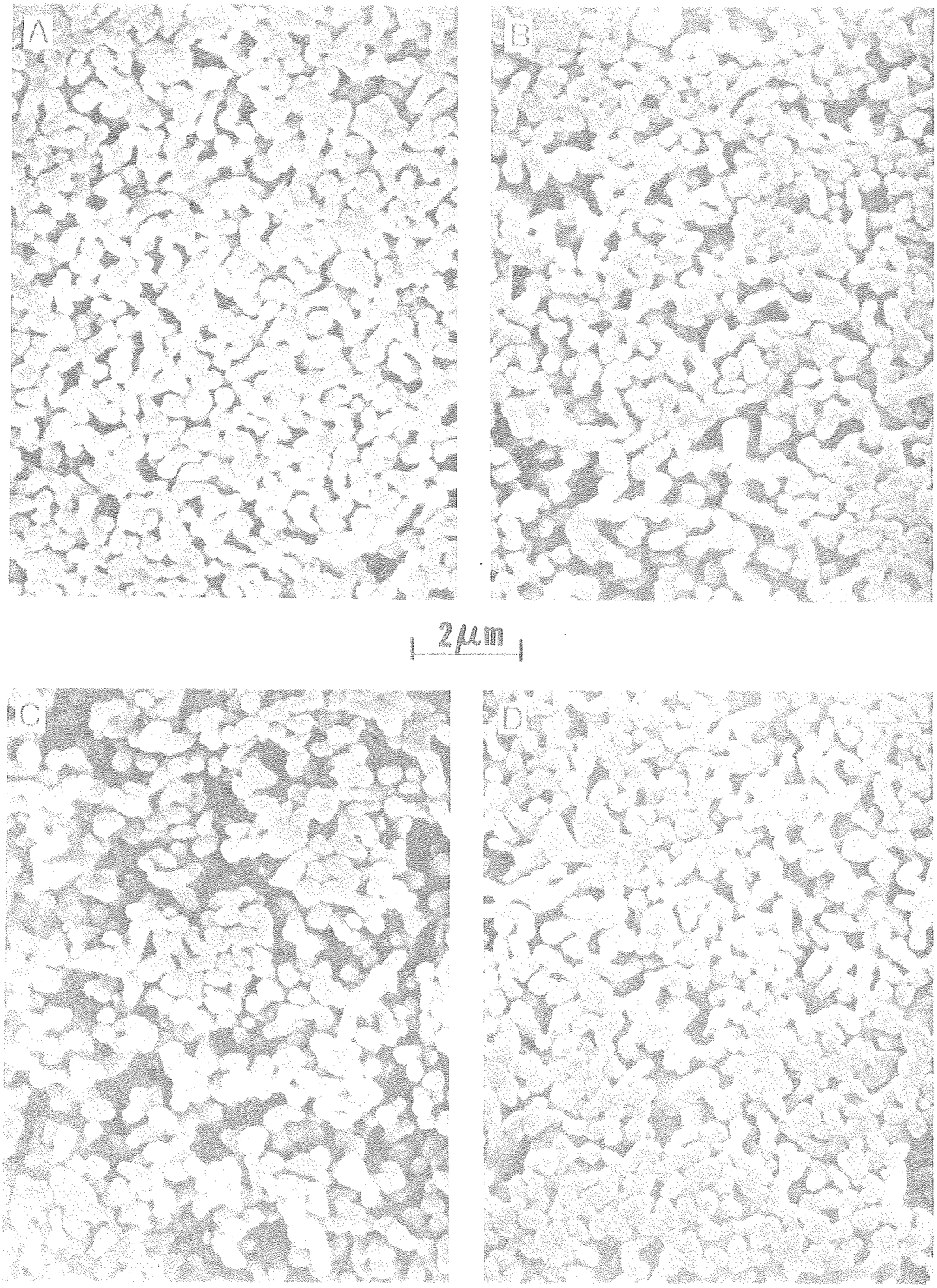

XBB768-7117

Fig. 35. Scanning electron micrographs of compacts with the same relative density of 65% by heating at rates of (A) 1.1°C/min, (B) 3.8°C/min, (C) 8.6°C/min, and (D) 13°C/min.

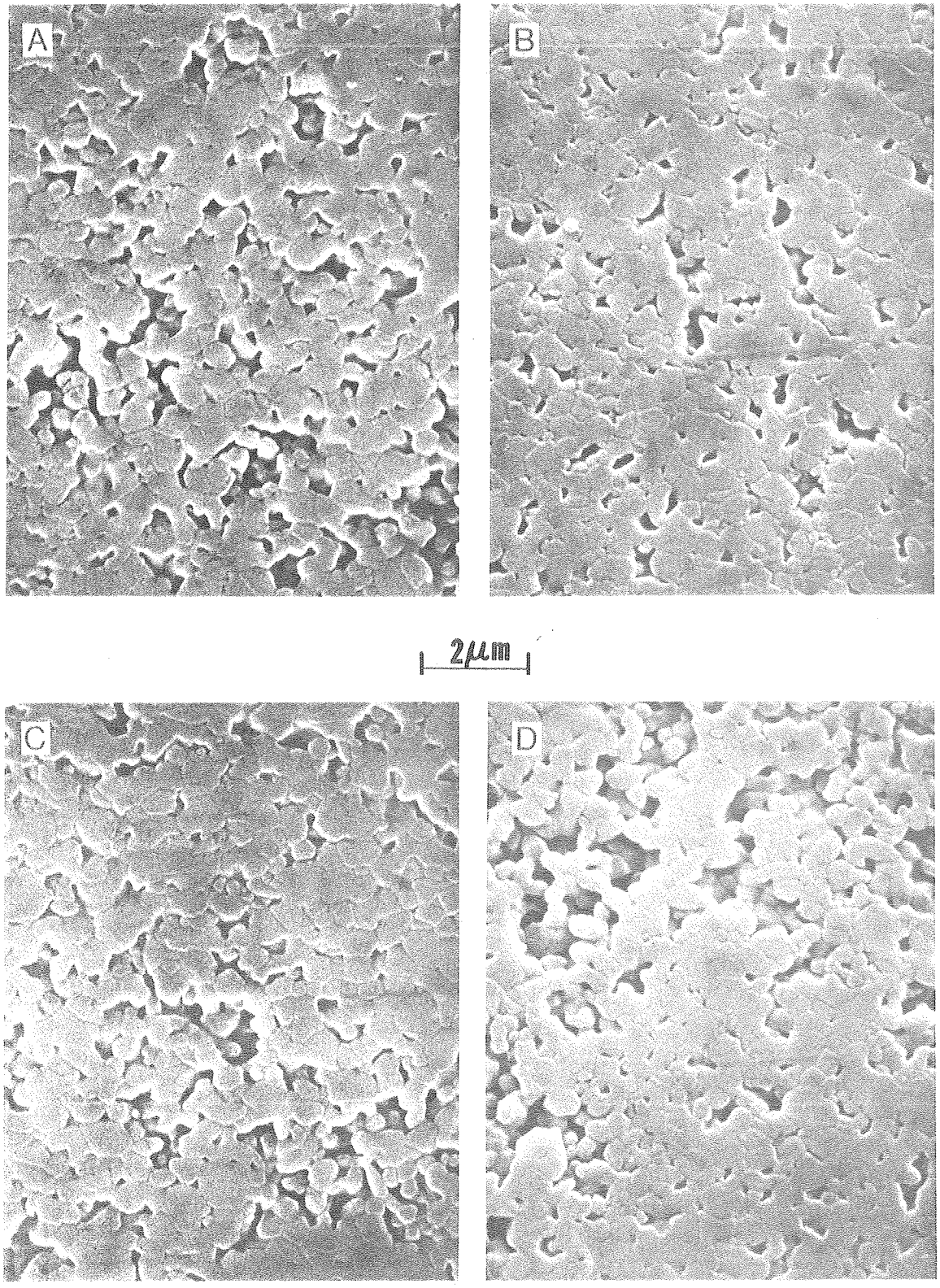

XBB768-7119

Fig. 36. Scanning electron micrographs of compacts with the same relative density of 77% obtained by heating at rates of (A) 1.1°C/min, (B) 3.8°C/min, (C) 8.6°C/min, and (D) 13°C/min.

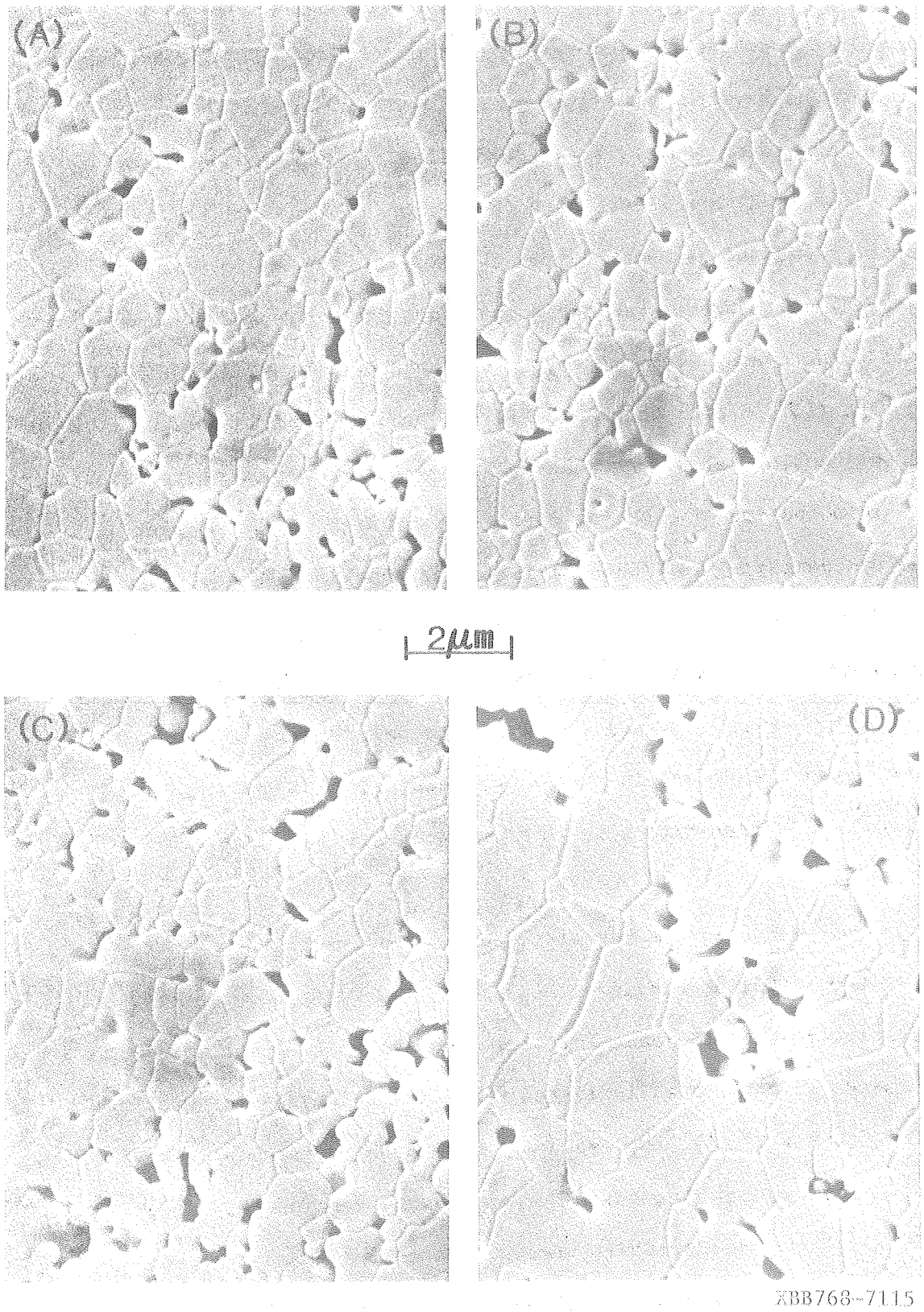

XBB768-7115

Fig. 37. Scanning electron micrographs of compacts with the same relative density of 95% obtained at rates of (A) 1.1°C/min, (B) 3.8°C/min, (C) 8.6°C/min, and (D) 13°C/min.

densities of 65%, 77% and 95%, respectively. In Fig. 35, all grains are chain-like and have the same average size. In Fig. 36, all grains are equiaxed and have the same average size. The change of grain shape from chain-like to equiaxial is expected since the two corresponding densities (65%, 77%) are those which fall below and above the transition region as has been observed from the evolution of grain structure shown in Fig. 34. However, as the compact density increases (or the temperature increases), the microstructure developed when using a high heating rate (13.0°C/min) becomes different from those developed when using lower heating rates. As seen in Fig. 37, for the microstructures at a relative density of 95%, the average grain size in the compact obtained by heating at 13°C/min (D) is larger than the average grain size in those compacts obtained by using lower heating rates (A, B, C). The early exposure to a high temperature (and consequently the rapid elimination of the small pores) is assumed to be the cause for the resulting larger grain size in the compact heated at 13°C/min. The change in densification rate with changing grain size will be discussed later.

A plot of grain size vs. density for compacts with green density of 40% of theoretical and doped with 0.1 wt% of MgO is shown in Fig. 38. The grain size remains the same for a given density irrespective of the heating rate. This relation indicates that, for this range of heating rates (2.5° to 9.4°C/min), the evolution of microstructure is insensitive to heating rate as long as the green density remains the same. Figure 39 gives the results which were generated from compacts of three different green densities (48%, 38% and 32% of theoretical) sintered at

0 0 0 0 0 4 2 0 2 3 3 3

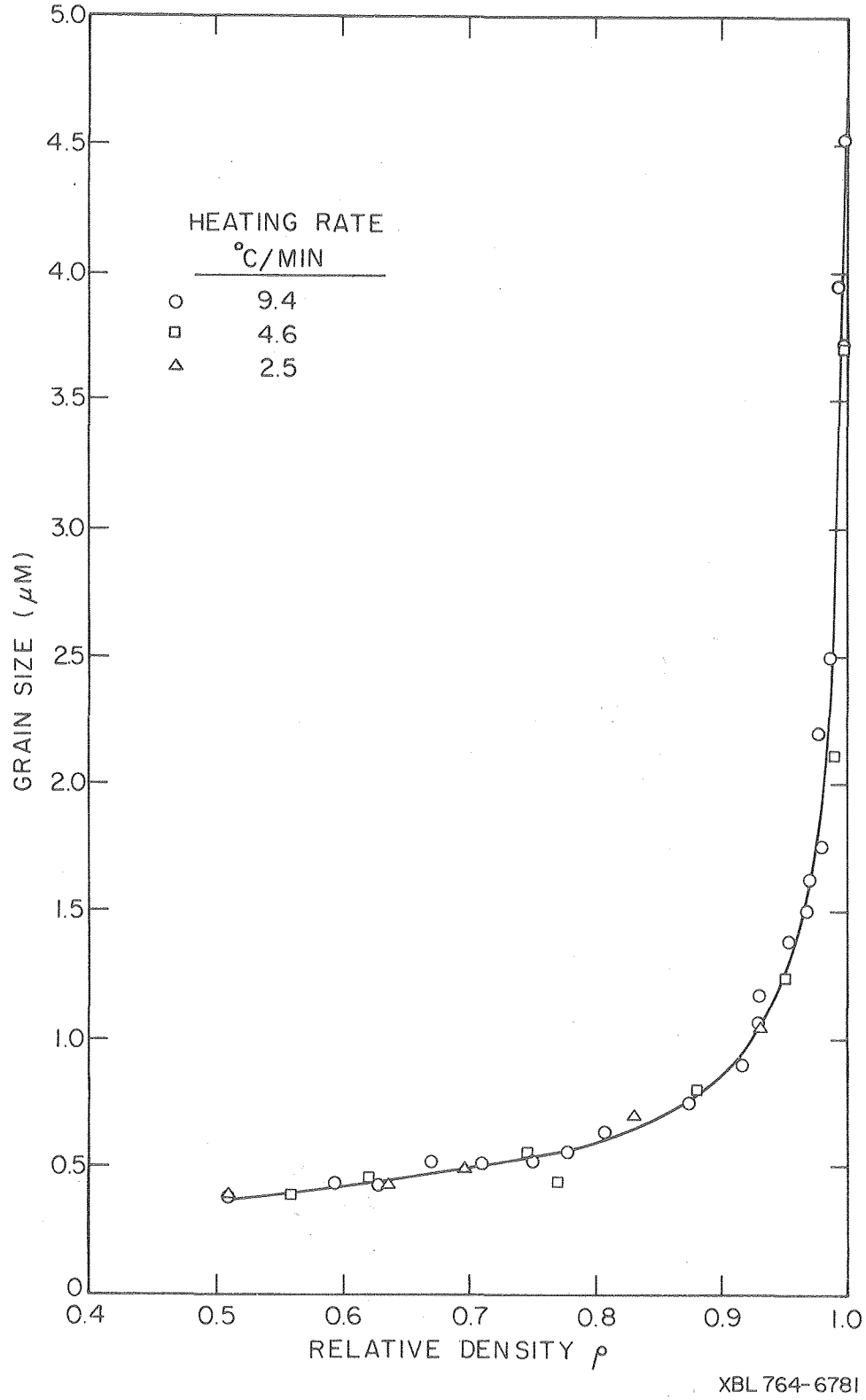

Fig. 38. Grain size vs. relative density for 0.1 wt% MgO-doped G. E. Al_2O_3 powder compacts (40% green density) heated at three rates.

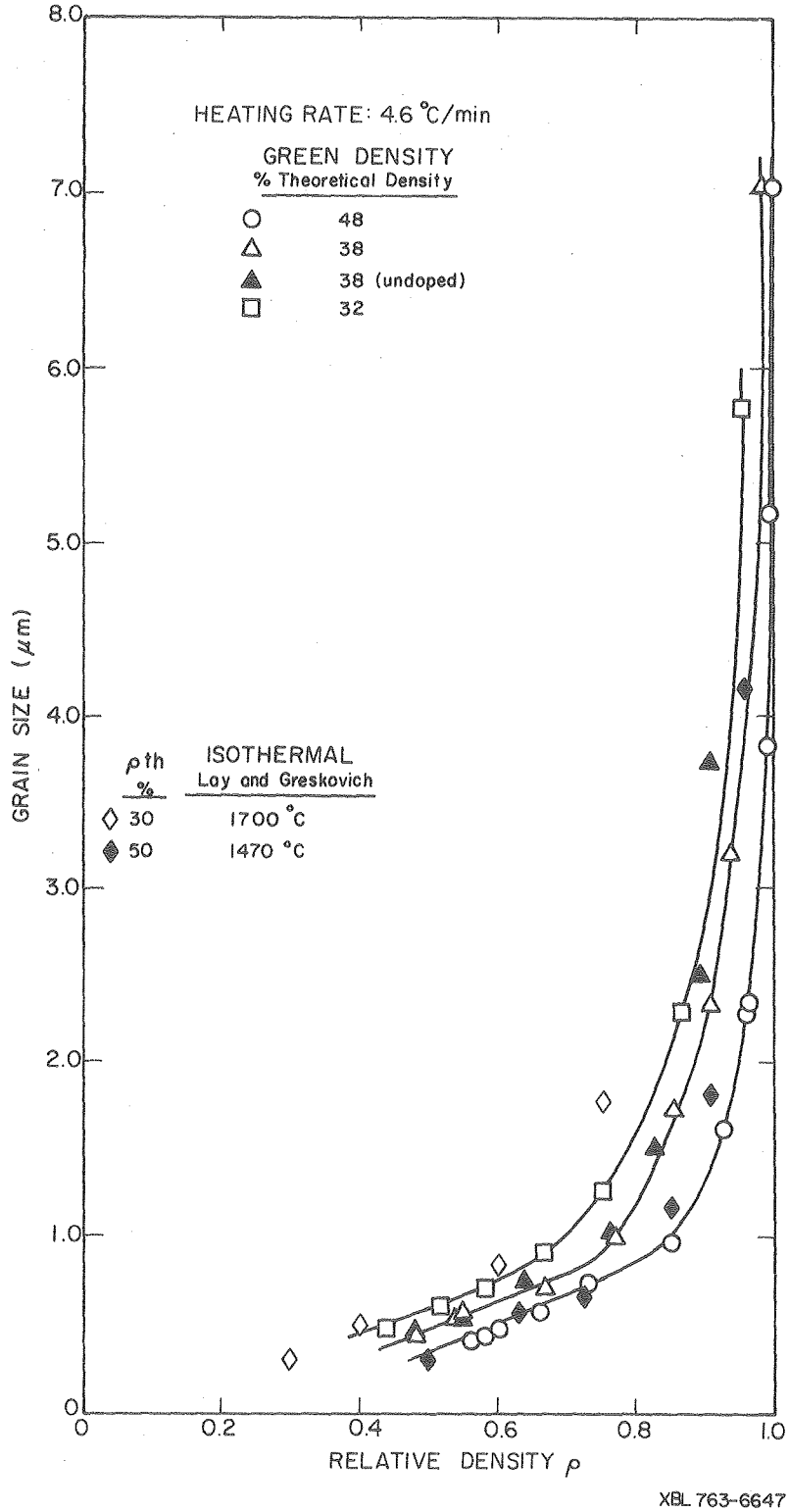

Fig. 39. Grain size vs. relative density for 0.1 wt% MgO-doped and undoped Union Carbide Al_2O_3 powder compacts with different green densities heated at a rate of 4.6° C/min. Isothermal data (Ref. 23) is presented for comparison.

the same heating rate (4.6°C/min). Previous measurements by Lay and Greskovich[23] using an isothermal sintering technique (1700° and 1740°C for compacts of green densities of 30% and 50% of theoretical, respectively) are also plotted in Fig. 39 to compare with the present results. Agreement is good until the curves start to bend upward. This agreement further shows the grain size-density relationship is independent of heating rate and temperature as long as the green density of the compact is kept constant. Figures 38 and 39 also illustrate that the grain size and density are linearly related until a particular density is reached. The density at which the linearity ends varies with green density. The densities at the bending points are approximately 75% of theoretical for the curve shown in Fig. 38 and 65%, 75% and 78% for green densities of 48%, 38% and 32% of theoretical, respectively, in Fig. 39. These values are about the same values that have been observed in Figs. 29 and 31 as the densities at which the maximum densification rate occurs. The reciprocal of the slope of the straight lines in Figs. 38 and 39 represents an incremental decrease in fractional void volume with an incremental increase in grain size. The decrease in void volume in the straight line section of these curves results mainly from the elimination and reduction in the size of the small pores. After the critical density is reached, local variation in pore concentration is developed and, consequently, grain growth in denser regions is no longer retarded by the presence of pores. This is the reason for the upward curve in the relationship between grain size and relative density after the critical density is reached.

At a given density, the microstructural features (such as grain size, pore size, pore shape, and pore-grain boundary geometry) are assumed (based on the qualitative and quantitative evidence presented) to be fixed during the sintering process, independent of heating rate used. The rate of the densification process can then be described by the following empirical equation regardless of the detailed mechanisms and the microstructural evolution with change of density.

$$\frac{d\rho}{dt} = \frac{K\exp(-\frac{Q}{RT})}{kT} P^n \tag{19}$$

where $\frac{d\rho}{dt}$ and ρ are densification rate and fractional porosity ($P = 1-\rho$) at any temperature, respectively. Q is the apparent activation energy for the densification process, n and K are constants, R is the gas constant, k is the Boltzmann constant, and T is the sintering temperature (°K) at which $\frac{d\rho}{dt}$ and p are determined. Therefore a plot of $\ln(T\frac{d\rho}{dt})$ vs. 1/T with relative density, ρ, kept constant should give a straight line if the apparent activation energy does not change during the densification process. This plot can be made by using the results which were obtained with four heating rates as shown in Fig. 26. For any value of relative density, there is a densification rate at each temperature. In Fig. 40 four values of $\ln T\frac{d\rho}{dt}$ (one for each heating rate) at four temperatures are plotted from a relative density of 50% to 98%. For $\rho = 0.98$ only three and two points, respectively, are shown because the final densities achieved by using 13.0°C/min and 8.6°C/min heating rates are below $\rho = 0.97$ and $\rho = 0.98$, respectively.

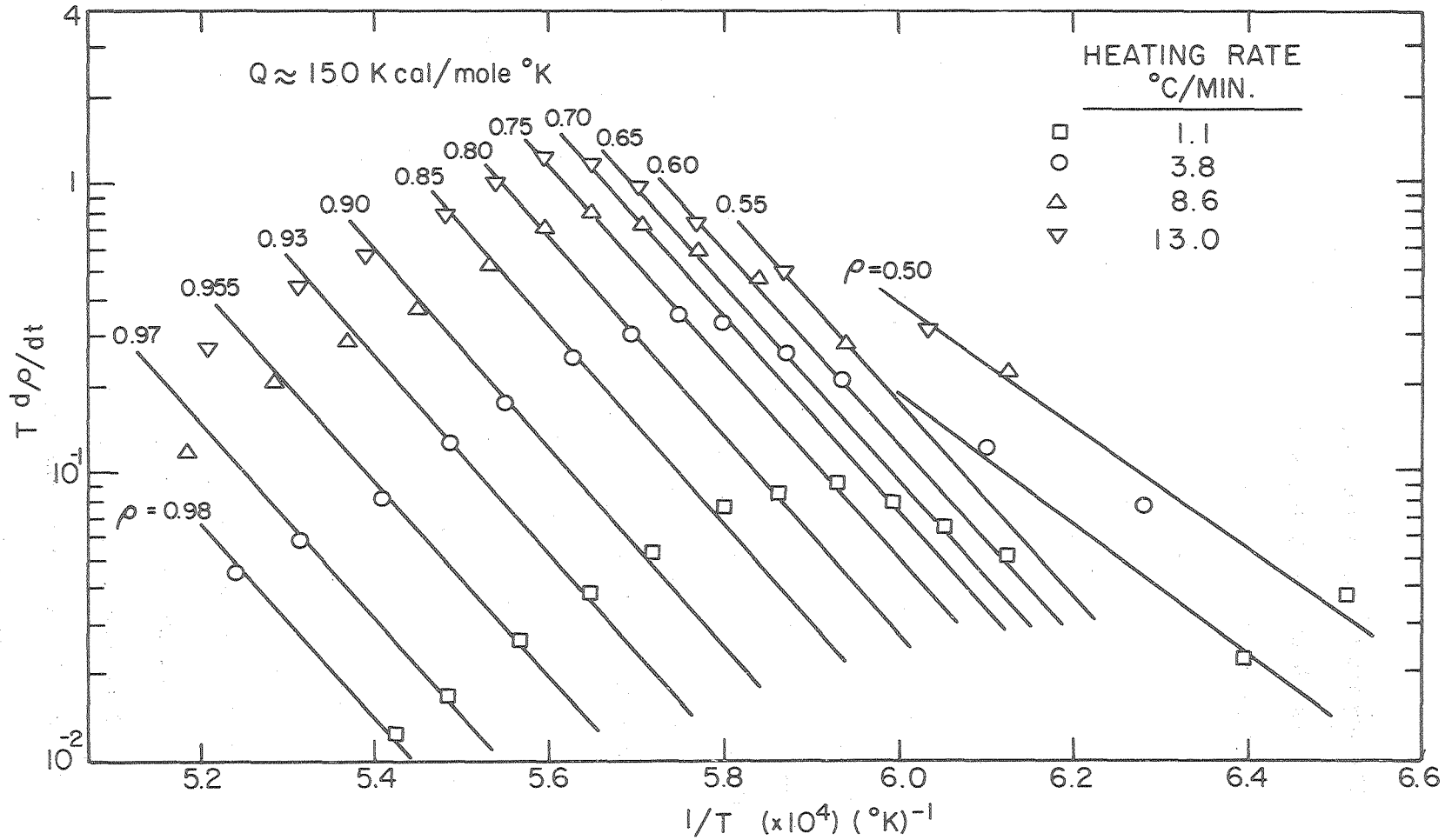

XBL 767-7254

Fig. 40. $\ln T \frac{d\rho}{dt}$ vs. $\frac{1}{T}$ for 0.1 wt% MgO-doped G. E. Al_2O_3 powder compacts with a 40% green density heated at four rates.

0 0 0 0 0 4 7 1 4 1 2 9 3

The apparent activation energy calculated from the slopes give two values. For densities below 55% of theoretical, the activation energy is approximately 90 Kcal/mole, while for densities above 55% of theoretical, the activation energy is approximately 150 Kcal/mole. The low value of 90 Kcal/mole is about the same value (93 Kcal/mole) determined for the initial stage sintering. The high value of 150 Kcal/mole determined in the present work agrees very well with the values of 153 Kcal/mole and 150 Kcal/mole reported by Coble[17] and Bruck,[22] respectively. The deviation of points with high heating rates at densities of 95.5% and 97% can be explained in terms of the larger average grain size as compared to those obtained at lower heating rates (see Fig. 37).

The observation of a single valued apparent activation energy for the whole densification process, except for the initial stage, suggests that (1) a single diffusion mechanism or a combination of mechanisms with the same activation energy predominates over the entire temperature range; and that (2) surface diffusion and evaporation-condensation mechanisms are primarily dependent rather than temperature dependent. If surface diffusion and evaporation-condensation are primarily dependent on the firing temperature, then with the present CRH technique, these mechanisms would cause different microstructural evolution in compacts of the same relative density. For example, if a slow heating rate is employed, the long time at low temperatures will favor surface diffusion. This changes the pore shape, which reduces the driving force for densification and, therefore, reduces the densification rate. However, this phenomenon is not observed in the present study as seen in Fig. 40.

By assuming a volume diffusion mechanism and by assuming the interior geometry of the compact to be represented by a system of uniform cylindrical pores situated on all the edges of polyhedra of uniform size, Coble[12] derived an equation to predict the time-dependence for intermediate stage sintering. Based on his assumptions, the equation is correct if it is presented in the form of

$$\frac{d\rho}{dt} = \frac{ND_v\gamma\Omega}{l^3kT} \tag{20}$$

Here $\frac{d\rho}{dt}$ is the densification rate at absolute temperature T(°K), N is a numerical factor[50] having the value of 335, D_v is the volume diffusion coefficient, γ is the surface energy, Ω is the volume of a vacancy, l is the edge length of the grain, and k is the Boltzmann constant. Since $D_v = D_o\exp(-\frac{Q}{RT})$ and $l \approx G$, the equation becomes, after rearrangement,

$$\frac{\frac{d\rho}{dt}\,G^3T}{\exp(-\frac{Q}{RT})} = \frac{ND_o\gamma\Omega}{k} = \text{constant} \tag{21}$$

In order to check the applicability of Coble's equation to the present results, simultaneous measurements of densification rate and grain size G at their corresponding temperature were used. Using the value of 150 Kcal/mole as the apparent activation energy Q, the values for the left hand side of equation (21) were calculated and plotted against porosity in Fig. 41. As shown in Fig. 41, Coble's equation for sintering kinetics holds up to a density of 70% of theoretical (30% porosity). The linear relationship between porosities of 30% and 5% can be explained by the interdependence of densification and grain growth kinetics which will be discussed in the next section. Because

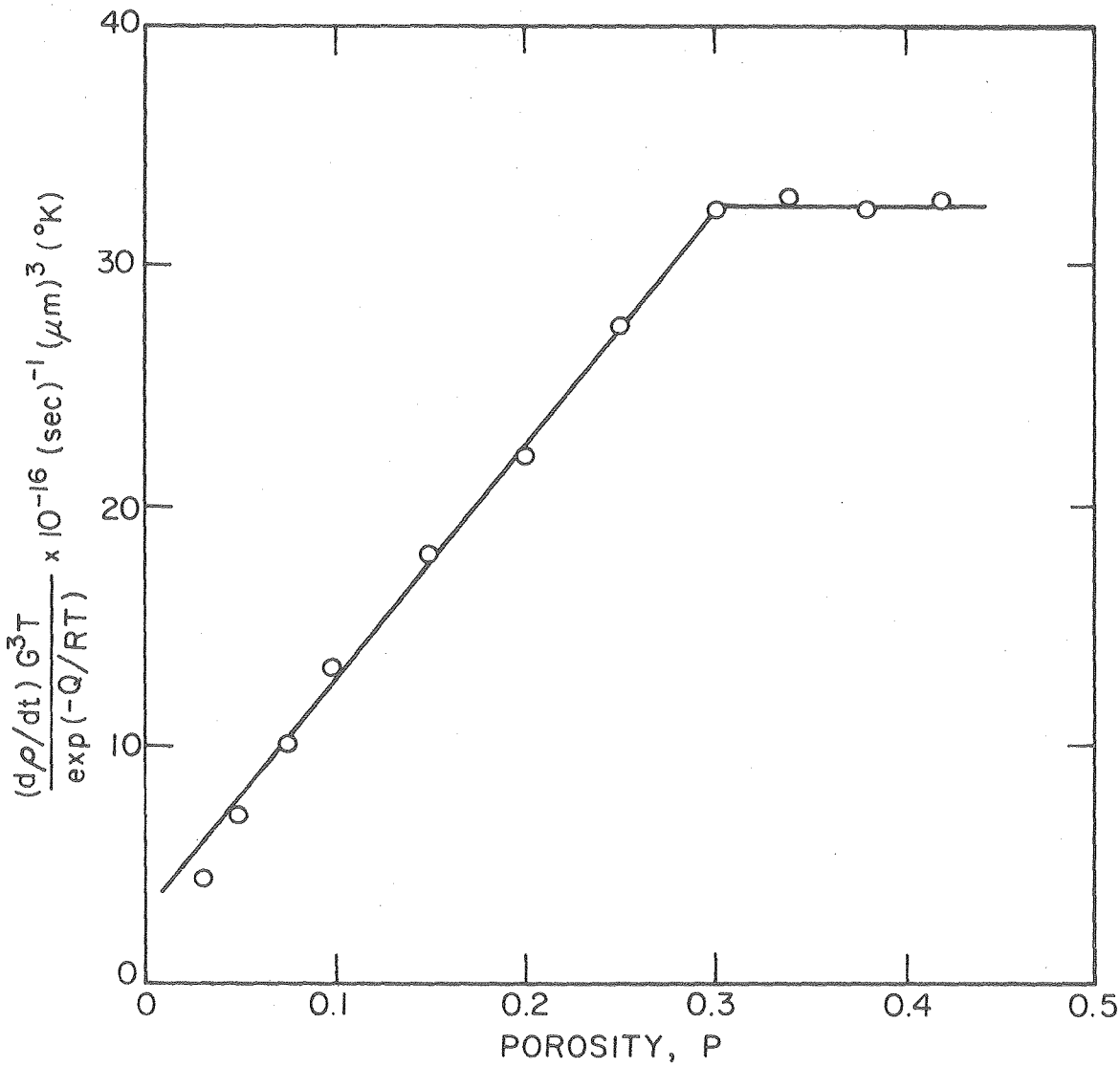

XBL 767-7252

Fig. 41. $(\frac{d\rho}{dt}\,G^3T/\exp(-\frac{Q}{RT})$ vs. porosity, P, plot using Coble's intermediate stage sintering equation (Ref. 12) for MgO-doped G. E. Al_2O_3 powder compacts.

0 0 0 0 0 4 7 0 0 2 3 7 7

the occurrence of the breaking point (70% relative density in Fig. 41) agrees well with the critical density value observed in Fig. 23, the inapplicability of Coble's equation can, therefore, be explained in terms of the local variation in pore concentration. The reduction of the total number of pores and the increase of the average pore size after the critical density is achieved were not taken into account in Coble's equation. Figure 42 replots the data from Fig. 41 with the results for three different green density compacts. As illustrated, the porosity-independent lines extend to different relative density values as green density of the compact varies. They are 78%, 72% and 63% for green densities of 48%, 38% and 32% of theoretical, respectively. These values agree well with their respective critical density values as shown in Fig. 31

In Fig. 42, the difference in the intercept values for the different green density compacts made from Union Carbide powders might be attributed to the difference in their microstructures. The ratio (number of grains between small pores/pore spacing) is assumed to be higher for low green density compacts than for high green density compacts because a higher total number of small pores are present in the high green density compact. If the densification for this stage, stage II, results from shrinkage of small pores, then the ratio of effective diffusion path length to the grain size is higher for low green density compact than for high green density compact. Therefore, this will change the intercept value if G is considered to be the grain size instead of the effective diffusion path length.

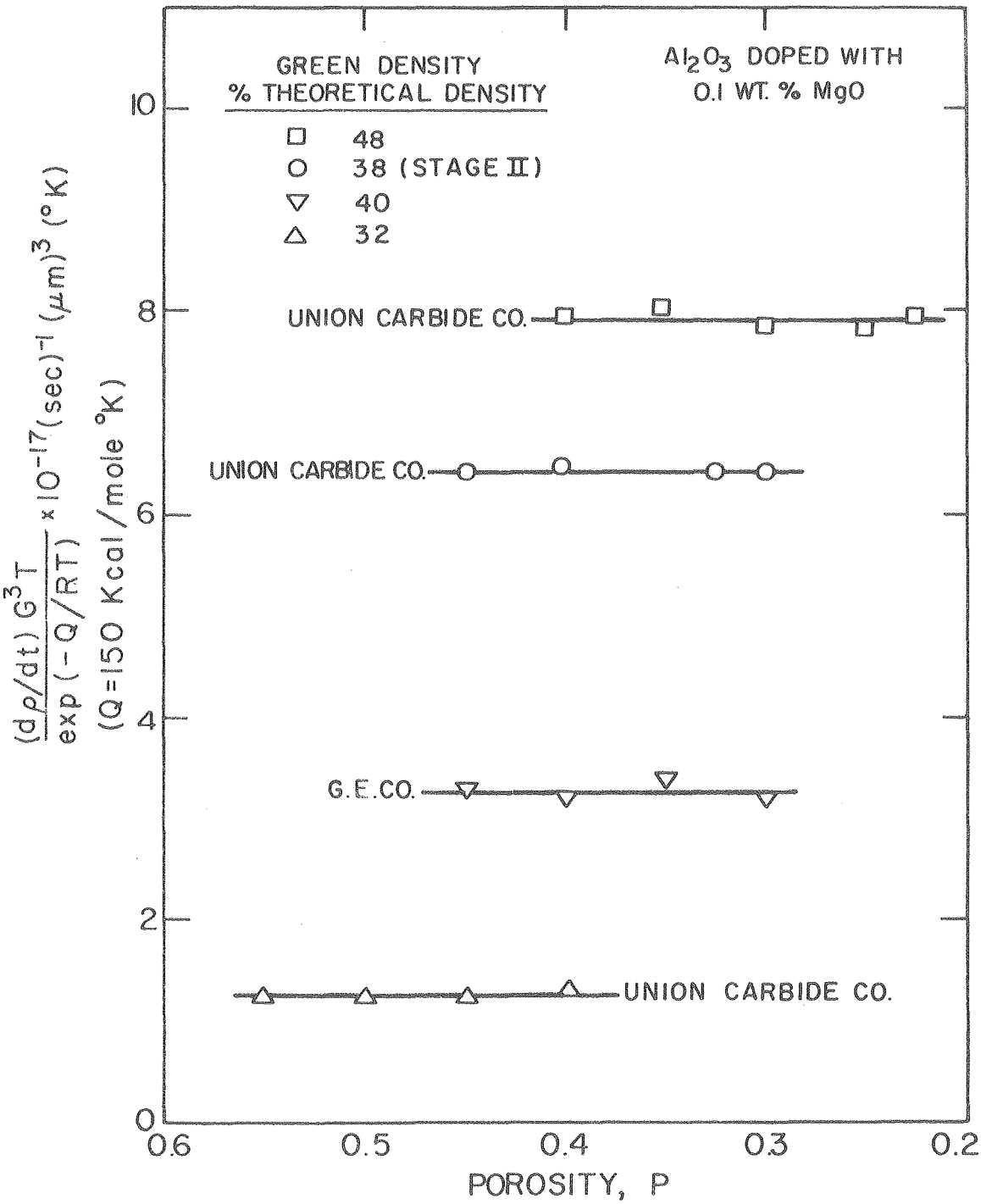

XBL 767-7248

Fig. 42. $(\frac{d\rho}{dt})\,G^3T/\exp(-\frac{Q}{RT}$ vs. porosity, P, plot using Coble's intermediate stage sintering equation (Ref. 12) for MgO-doped Union Carbide Al_2O_3 compacts of various green densities.

0 0 0 0 3 4 7 0 0 4 2 3 8 8

The values of the diffusion coefficients D_v for compacts of different green densities and powders are calculated from their stage II sintering kinetics using Coble's equation (with γ = 1,000 erg/cm^2 and $\Omega = 1.4 \times 10^{-23} Cm^3$). These values are shown in Fig. 26 along with previously reported values. The reason for the discrepancy observed in diffusion coefficients is the same as that described for the discrepancy in the intercept values in Fig. 42.

The activation energy calculated from these results, using Coble's equation is the same value, 150 Kcal/mole, determined in Fig. 42 for shrinkage of pores.

2. Grain Growth Kinetics

Grain boundary migration occurs when a grain boundary is subjected to a sufficiently high driving force. The resultant boundary migration will be such as to cause a reduction in the free energy of the system.

Boundary migration is a thermally activated process and hence the rate at which a boundary migrates under the influence of a given driving force is strongly temperature-dependent.

The relationship between the migration rate, V, and the driving force, P, for a hypothetically "pure material" is generally given by the equation

$$V = MP \tag{22}$$

where M, the intrinsic mobility of a boundary in the pure material, is of the form $M = M_o \exp(-\frac{Q_b}{RT})$ and Q_b is the activation energy for grain boundary self-diffusion.[24]

By making a number of assumptions,[51] a theoretical expression for the rate of grain growth in a polycrystalline material can be deduced

from equation (22).

$$V\alpha\frac{dG}{dt} = \frac{AM\gamma_b}{G} \tag{23}$$

or in integral form

$$G^2 - G_o^{\ 2} = 2AM\ \gamma_b t \tag{24}$$

where G is the average grain diameter, G_o is the grain size at t = 0, A is a geometrical constant, and γ_o is the interfacial energy of the grain boundary.

Increasing the temperature should cause the rate to increase according to the relationship

$$G^2 - G_o^{\ 2} = AM_o\gamma_b\exp(-\frac{Q_b}{RT})t \tag{25}$$

In experimental work, it is common to obtain a series of isothermal grain growth measurements at various temperatures and to plot log G vs. log t by assuming G_o is negligible. The resultant curves can usually be represented by the empirical relationship.[52]

$$G^m = k_o\exp(-\frac{Q}{RT})t \tag{26}$$

Equation 25 predicts that the exponent m = 2 and Q = Q_b. In fact, values of m>2 and Q>Q_b are commonly found. These values may occur for several reasons: (1) G_o is not negligible when compared with G and (2) a second phase (solid inclusions and pores) and/or solute impurities are commonly present in polycrystalline materials.

Solute effects have been considered by Lücke and Detert[53] and Cahn.[26] These authors suggested that there are two types of boundary migration. At low temperatures and with small driving forces, solute atoms will be sufficiently bound to a grain boundary so that the rate-

0 0 0 0 3 7 0 3 2 3 0 9

determining factor for boundary migration will be the rate at which solute can diffuse through the bulk lattice while moving along with a migrating grain boundary. At high temperatures and with large driving forces, grain boundaries will be able to break away from their atmospheres of solute atoms and migrate independent of the solute. The activation energy for this break-away solute-independent migration is that of grain boundary self-diffusion while the activation energy for solute-dependent boundary migration is very close to that for diffusion of solute through the bulk lattice.

Gordon[54] was able to show that the nature of the transition between migration in the impurity-bound state to migration in the broken-away state would depend on the magnitude of the driving force. For low driving forces, such as in the grain growth, the transition between the solute-dependent and solute-independent migration would be characterized only by a change in slope of an Arrhenius plot of velocity versus inverse temperature.

The effect of second phase inclusions on grain growth has been discussed by Beck[55] who points out two basic interaction mechanisms: (1) At very small driving forces, the grain boundaries are pinned by inclusions which must be dragged along if the boundary is to migrate; and (2) If the driving force for grain boundary migration exceeds the pinning force exerted by the inclusions, then the boundary is pulled free from the inclusions and passes through the lattice without changing the distribution of the inclusions. The temperature dependence of the mobility of the boundary in the bypassing process (case 2) will be similarly characterized by grain boundary self-diffusion as in the case

of the broken-away solute-independent migration process. In the sweeping of inclusions (case 1) material transport, either in the surrounding matrix or in the inclusion-matrix interface, is required. The activation energy observed for the grain growth would then depend on the possible rate controlling process involved. Since the sweeping of inclusions is limited to low driving forces and the bypassing process is only possible at high driving forces, a migration mode exists at intermediate driving forces where the transition from sweeping to bypassing occurs.

Zener[56] showed that as a result of pinning by a second phase (solid inclusions or pores) the grain size should be limited by the volume fraction and the size of the second phase.

Hillert[57] found that if the second phase grows due to a diffusion controlled mechanism the average grain size is predicted to increase as

$$G^3 = kt \qquad (27)$$

Moreover, this derivation assumes a constant volume fraction of pinning particles, and therefore, does not strictly apply to pores during sintering.

Kingery and Francois[29] considered grain growth controlled by migrating pores. Their assumptions were (1) the driving force is inversely proportional to the average grain size, (2) the grain boundary migration rate is the same as the pore migration rate, (3) the pore migration rate is inversely proportional to the pore size, and (4) the pore size is proportional to the grain size. With these assumptions, they found $G^3 \alpha t$.

0 0 0 0 0 1 7 0 4 2 3 0 0

Following the idea of pore migration along the grain boundary, Nichols[27] showed that the cubic law must be interpreted as being controlled by vapor transport through the pore with the pressure maintained at $2\gamma/r$, where γ is the surface tension and r the pore radius. The calculated activation energy for grain growth is therefore the heat of vaporization for the material. This theory predicts that the compact should show a decrease in density during grain growth. This behavior has been observed in the case of UO_2 but apparently has not yet been reported for Al_2O_3.

Previous studies on the grain growth kinetics in Al_2O_3 compacts have concentrated on the 90-99$^+$% density range. A cubic growth law and an activation energy of approximately 150 Kcal/mole were determined by using MgO-doped Al_2O_3 compacts.[17,21,22] Recently, Greskovich and Lay[23] have studied the grain growth in very porous MgO-doped Al_2O_3 compacts. The temperature dependence of the process was not determined since only one temperature was used.

In the present work, a more extensive study of grain growth kinetics was made. MgO was added to the Al_2O_3 powders to prevent exaggerated grain growth. The amount of MgO added was 0.1 wt% which is equivalent to 1000 ppm MgO. Roy and Coble[58] found the solubility of MgO in Al_2O_3 in vacuum was given by the equation

$$\ln X = 8.1 - 30{,}706/T \qquad (28)$$

where X = atomic fraction Mg/(Mg + Al) and T = absolute temperature. Since this means a solubility of 680 ppm MgO in Al_2O_3 at 1750°C in vacuum, the amount of MgO used in the present work should result in the

formation of a second phase. In order to study this prediction, compacts doped with 0.1 wt% of MgO were sintered at 1750°C in H_2 for 1 hour and in vacuum for 10 hours. Metallography established the presence of second phase particles at the grain boundaries (See Fig. 43 A and B). Figure 43C shows the EDAX analysis on one of the particles in which the presence of Mg is confirmed by the peak furthest to the left in the spectrum. The other two peaks show the presence of Al and Au which were from the Al_2O_3 and Au coating on the specimens, respectively. However, the second phase particles were not found in low density or fine grained compacts. This fact indicates that the distribution of second phase particles has changed during the grain growth process. This change further implies that the grain boundaries are pinned by the second phase inclusions and consequently, the inclusions are dragged along with the migrating boundaries. This effect is expected particularly in the later stage of grain growth when the driving force is small. Once particle dragging starts, the boundary collects practically all particles in the volume which it sweeps and, therefore, the region behind the boundary is almost free of inclusions. Thus, particles collected in the boundaries coalesce more rapidly than those in the grains. If a small grain shrinks, all the particles collected in its boundary will cluster together and form one large particle as has been illustrated in Fig. 43A and B.

The functions of second phase inclusions in the sintering of Al_2O_3 powder can be understood by comparing the densification and grain growth behavior of doped and undoped compacts. Figure 44 gives the relative density vs. temperature plot for compacts with a 40% green density which

0 0 0 0 3 7 0 3 2 3 1

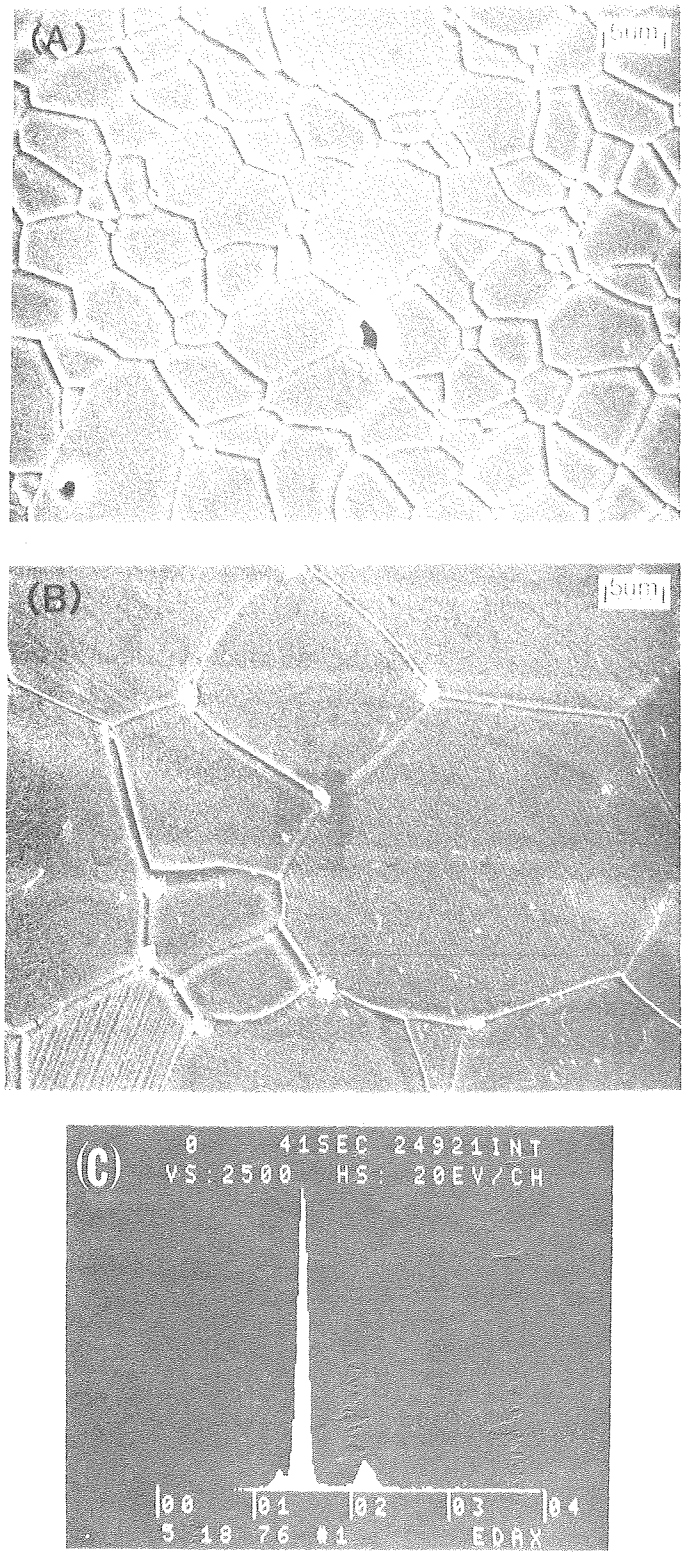

XBB768-7105

Fig. 43. Scanning electron micrographs of second phase in 0.1 wt% MgO-doped Al_2O_3 compacts sintered (A) at 1750°C in H_2 for one hour and (B) at 1750°C in vacuum for 10 hours. EDAX spectrum for a second phase particle is shown in (C). Mg is the small peak to the left, the center peaking Al, and the right hand peak is Au from the conductive coating on the specimen.

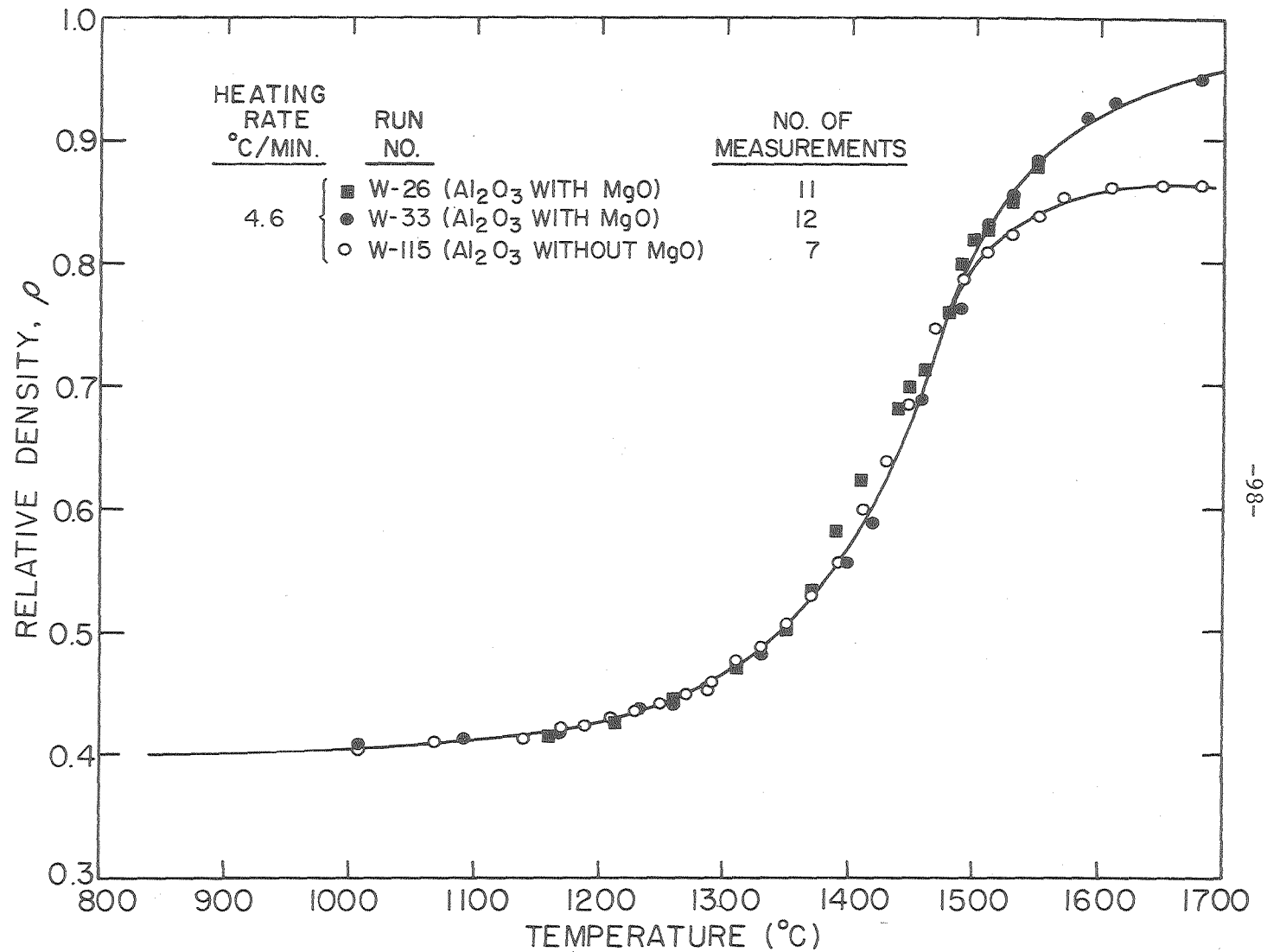

Fig. 44. The relative density as a function of temperature for 0.1 wt% MgO-doped and undoped Al_2O_3 powder compacts heated at a rate of 4.6°C/min.

0 0 0 0 0 4 7 0 0 1 2 3 2 2

were heated at 4.6°C/min. There is no effect on the densification kinetics until the critical density of 75% is reached. After the attainment of the critical density, a deviation in the rate of densification occurs between doped and undoped compacts. Comparison of the microstructures for doped and undoped Al_2O_3 at different densities shows that there is essentially no difference in grain size and pore distribution for the compacts of 70% relative density at 1450°C (Figs. 45A, B, C and D). When the density increases to a value above the critical density (Figs. 45E, F, G and H), the microstructures for doped and undoped compacts become different. This can be understood by considering that the driving force for grain boundary migration undergoes a transition from bypassing to sweeping the inclusion particles, and this transition occurs at the critical density. Grains in the compacts with densities below the critical density will have a large driving force for boundary migration and, therefore, the boundary bypasses the inclusions. As a result, there is no effect of the MgO dopant on the densification and grain growth kinetics. Grains in the compacts with densities above the critical density will have a small driving force due to the large grain size and, more importantly, to the shape change of the grains. As has been described (see Fig. 34), grain shape becomes equiaxed when the density of compact is above the critical density which thereby reduces the boundary curvature. Therefore, with the small driving force, the boundaries in MgO doped compacts will migrate with a slow rate due to the pinning effect by the second phase particles while the boundaries in the undoped compact will move at a high rate. This is illustrated in Figs. 45G, H, and J. The high boundary migration rate in the undoped

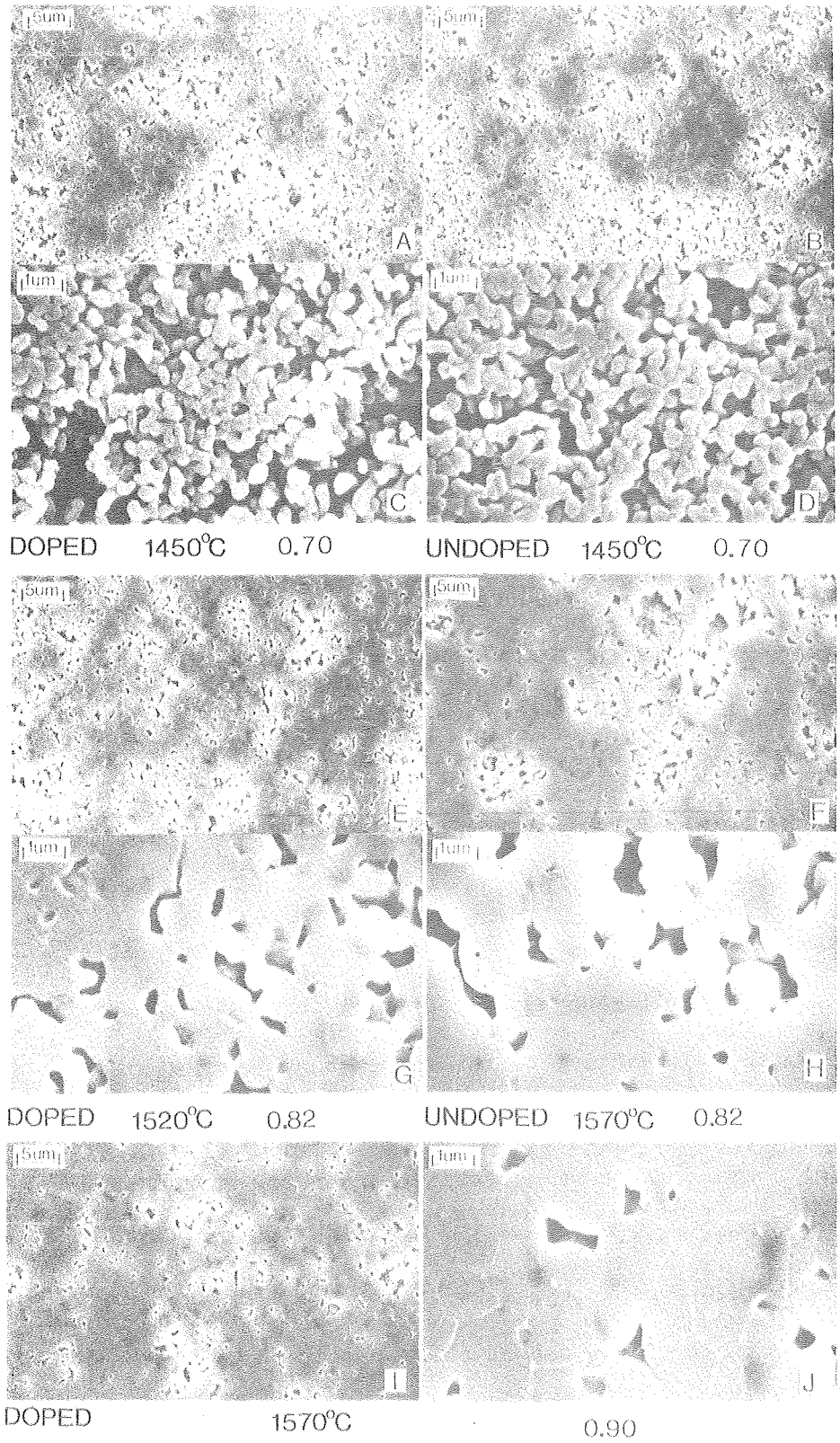

XBB758-8628

Fig. 45. Comparison of microstructural evolution for MgO-doped and undoped Al_2O_3 powder compacts. The number appearing to the right of the temperature represents the value of relative density.

0 0 0 0 0 1 0 7 0 1 2 3 3 3

compact results in an exaggerated grain growth in which pores are entrapped in the grains (see Fig. 45H).

In the present work, since a CRH technique was used, a modification of equation (26) is needed in order to analyze the experimental results. After differentiation at constant temperature, equation (26) becomes

$$G^{m-1} \frac{dG}{dt} = k_o \exp(-\frac{Q}{RT}) \tag{29}$$

or

$$(m-1) \ln G + \ln \frac{dG}{dt} = \ln k_o - \frac{Q}{RT} \tag{30}$$

From equation (30), a plot of $\ln \frac{dG}{dt}$ at a specific grain size, G, vs. $\frac{1}{T}$ gives a straight line of slope $-\frac{Q}{R}$. The activation energy for the grain growth process, Q, can then be determined. A ln-ln plot of grain growth rate, $\frac{dG}{dt}$, at a specific temperature vs. grain size, G, gives a straight line of slope -(m-1), thereby determining the growth law.

Figure 46 gives the results obtained from G. E. powder compacts which were heated with three heating rates (2.5, 4.6 and 9.4°C/min). The activation energies were calculated as 95 Kcal/mole and 150 Kcal/mole for grain growth kinetics below and above the critical density, respectively. As discussed previously, the large driving force for boundary migration in the compacts below the critical density allows the boundary to bypass inclusion particles. This results in a temperature dependence of the mobility of the boundary which is characteristic of grain boundary self-diffusion. The activation energy of 95 Kcal/mole observed indeed approximates the value of 93 Kcal/mole observed for the initial stage sintering process in which a grain boundary diffusion mechanism was assumed.

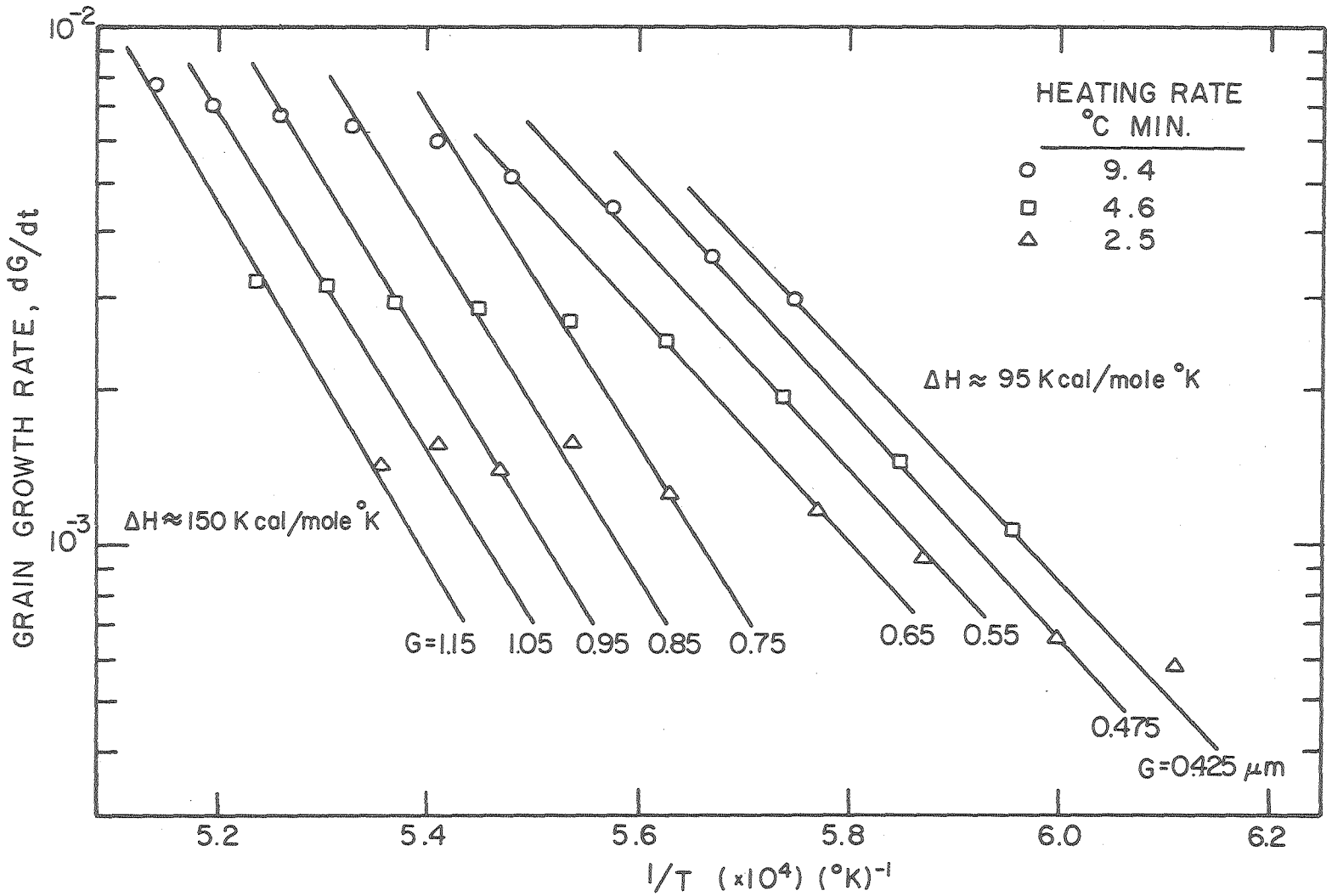

XBL 767-7253

Fig. 46. Arrhenius plot of grain growth rate vs. 1/T for 0.1 wt% MgO-doped G. E. Al_2O_3 compacts with a 40% green density.

0 0 0 0 0 1 7 0 0 2 3 0 4

Greskovick and Lay[23] proposed a grain growth mechanism for very porous Al_2O_3 compacts (which are equivalent to the compacts below the critical density in the present study). They suggested that the grain boundary cannot migrate from the neck region because increases in interfacial area and total interfacial energy would be required. Therefore, the grain growth mechanisms must involve the growth of a neck between two particles (principally via surface diffusion) and the migration of the boundary which may be followed by spheroidization of the remaining single particles. If the boundary migration is controlled by the formation of a neck, one should expect to find the same value of activation energy for the simultaneous densification and grain growth which occurs during this interval (50 to 75% relative density). In contrast, this study found an activation energy of 150 Kcal/mole for the densification process and 95 Kcal/mole for the grain growth kinetics. The independence of grain growth from neck formation might be due to the fact that there are non-equilibrium defects in the initial powders since the powders were chemically prepared and subjected to a low temperature decomposition. In contrast to surface tension-induced grain boundary migration in which boundaries always move toward their centers of curvature, strain-induced boundary movement occurs in such a manner that the boundary may well move away from its center of curvature. One of the interesting aspects[59] of strain-induced boundary migration is that the total surface energy of the boundary may actually increase by an increase it its area. In addition, it has been suggested by several investigators[60,61] that the rate of boundary migration can be affected by the vacancy concentration.

The intrinsic mobility of a grain boundary is a function of the supply of vacancies to a migrating boundary. This further supports the idea that grain boundary migration may be independent of neck formation.

The activation energy of 150 Kcal/mole for the later stage grain growth process agress well with the values of 153 Kcal/mole and 153.7 Kcal/mole obtained by Coble[17] and Bruch,[22] respectively, in high density compacts using isothermal sintering techniques. This high value of activation energy indicates that the boundary migration is (1) controlled by the pores present in the microstructure and/or (2) controlled by the solid inclusion particles.

A ln-ln plot of growth rate vs. grain size at specific temperatures is presented in Fig. 47. Solid circles in this figure represent a transition region. Values of 2.5 and 3.2 for the exponent m in equation (26) are determined for the region below and above the critical density, respectively.

A plot of grain size vs. temperature for Union Carbide powder compacts with green densities of 32%, 38%, and 48% of theoretical, heated at a rate of 4.6°C/min, is presented in Fig. 48. Unlike the observation by Bruch,[22] who found no effect of the green density on the sintered grain size, the grain size in the present work has been found to increase as the green density increases at any temperature (Fig. 48). Microstructures obtained for compacts with green densities of 32%, 38% and 48% of theoretical heated at the rate of 4.6°C/min to 1640°C are shown in Figs. 49A, B, and C, respectively. In these microstructures, all pores are intergranular and the grain size varies with green density. It is assumed that the difference in the microstructural development in

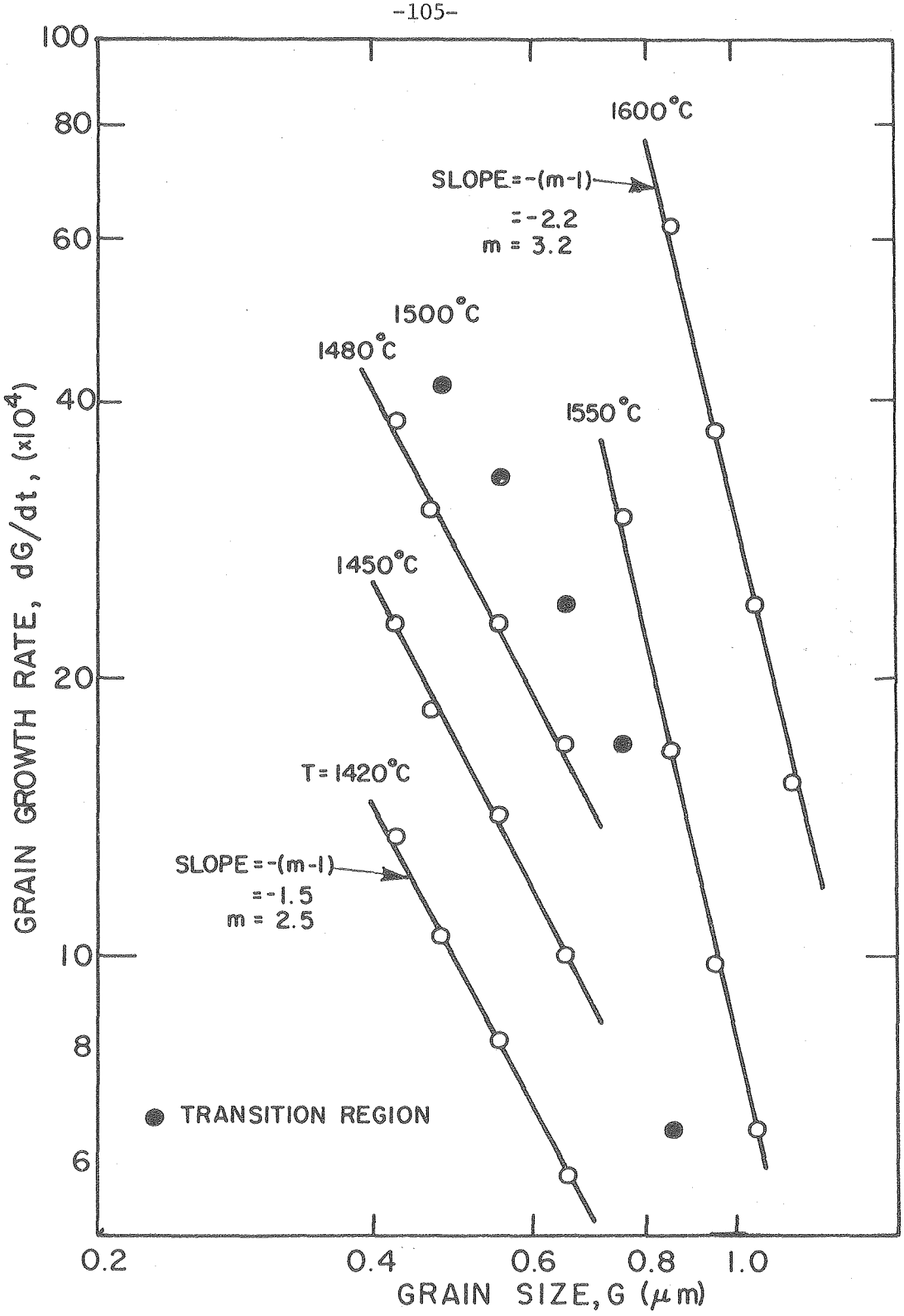

XBL 767-7246

Fig. 47. Plot of ln grain growth rate vs. ln grain size for MgO-doped G. E. Al_2O_3 compacts of 40% green density.

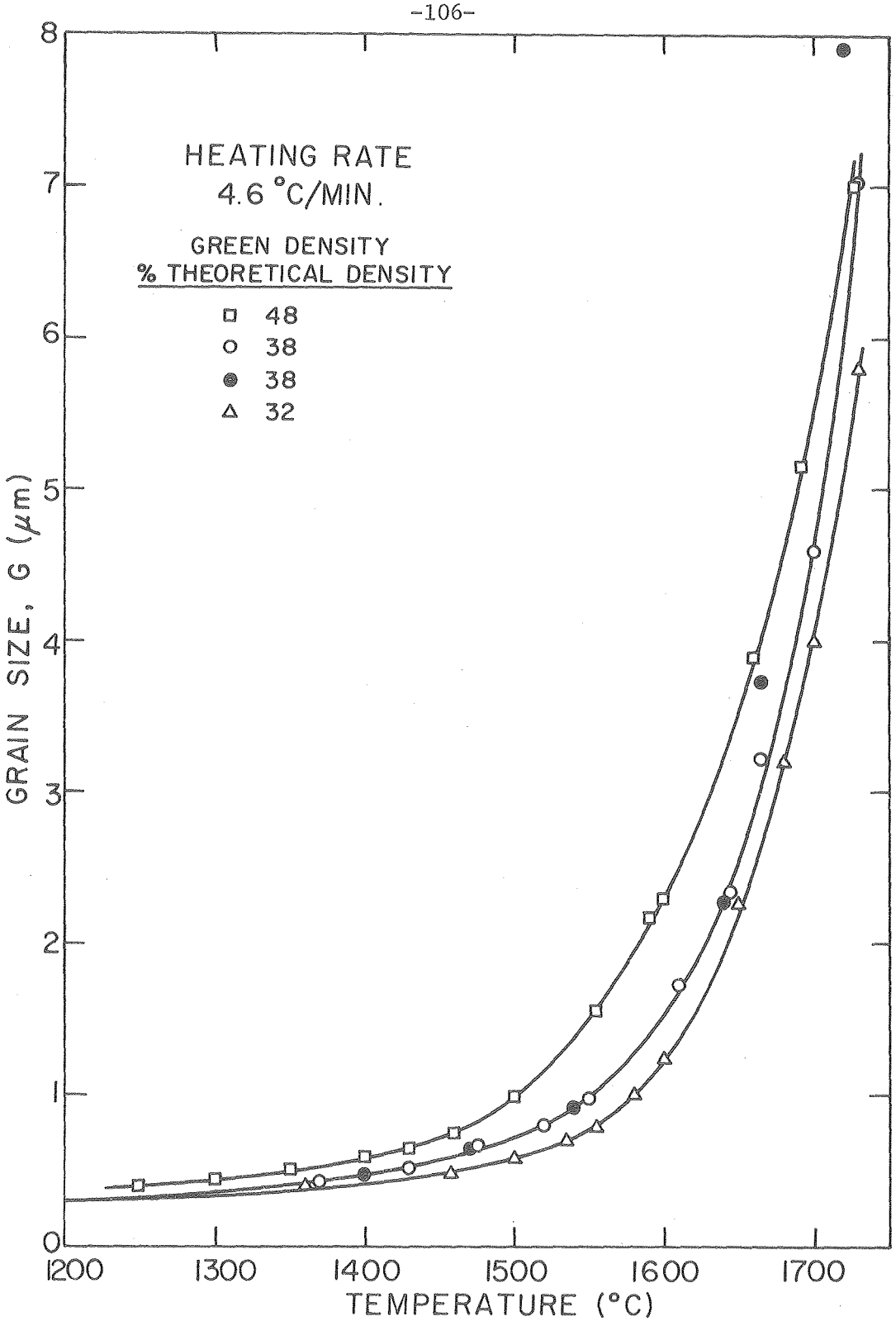

XBL 767-7251

Fig. 48. Grain size vs. temperature for MgO-doped and undoped Union Carbide Al_2O_3 compacts of various green densities heated at a rate of 4.6°C/min.

0 0 0 0 0 0 0 4 7 7 0 0 4 0 2 5 8 3 5 6

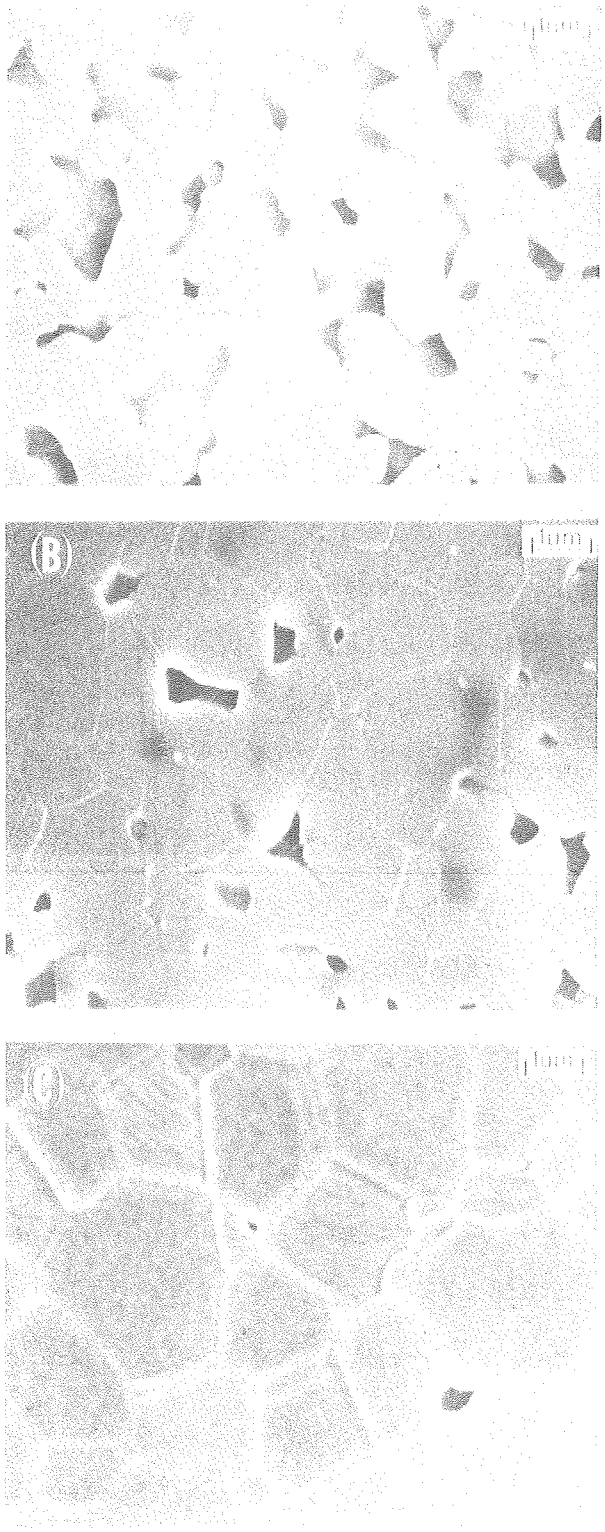

XBB768-7107

Fig. 49. Scanning electron micrographs for MgO-doped Al_2O_3 compacts with green densities of (A) 32%, (B) 38%, and (C) 48% of theoretical after sintering at the rate of 4.6°C/min to 1640°C.

this study from Bruch's work is attributed to the difference in sintering atmosphere used. In the present work, a vacuum atmosphere was used while in Bruch's work a H_2 atmosphere was used. In order to understand the effect of firing atmosphere on the microstructural development, compacts with different green densities (32%, 38%, and 48% of theoretical) were rapidly brought to 1750°C in 10^{-6} torr vacuum and 0.8 atmosphere H_2 and held for one hour and 10 hours (Figs. 50 and 51). Examination of these microstructures reveals the following: (1) Extensive pore-grain boundary separation was developed in the vacuum sintered compacts with low green densities (32%, 38% of theoretical), (2) No effect of green density on the sintered grain size for those compacts sintered in H_2 atmosphere (further confirming the observations by Bruch), (3) Although there is a variation in grain size with green density for vacuum sintered compacts, this difference is not as noticeable as that observed for compacts sintered with constant heating rate (see Fig. 49), and (4) No effect of firing atmosphere on either the densification or the grain growth was found for compacts of 48% green density.

These observations can be best explained in terms of the mobility of pores. It is supposed that pores are immobile in a vacuum atmosphere but mobile in H_2 atmosphere. Pore migration can be accomplished by mass transport processes (such as evaporation-condensation, surface diffusion, or volume diffusion) as a result of different in curvature of the pore surfaces which is usually determined by the pore-boundary geometry. Pore mobility might be expected to change with different firing atmospheres since γ_{sv} (and the resulting dihedral angle)

0000: 0044770 0268877

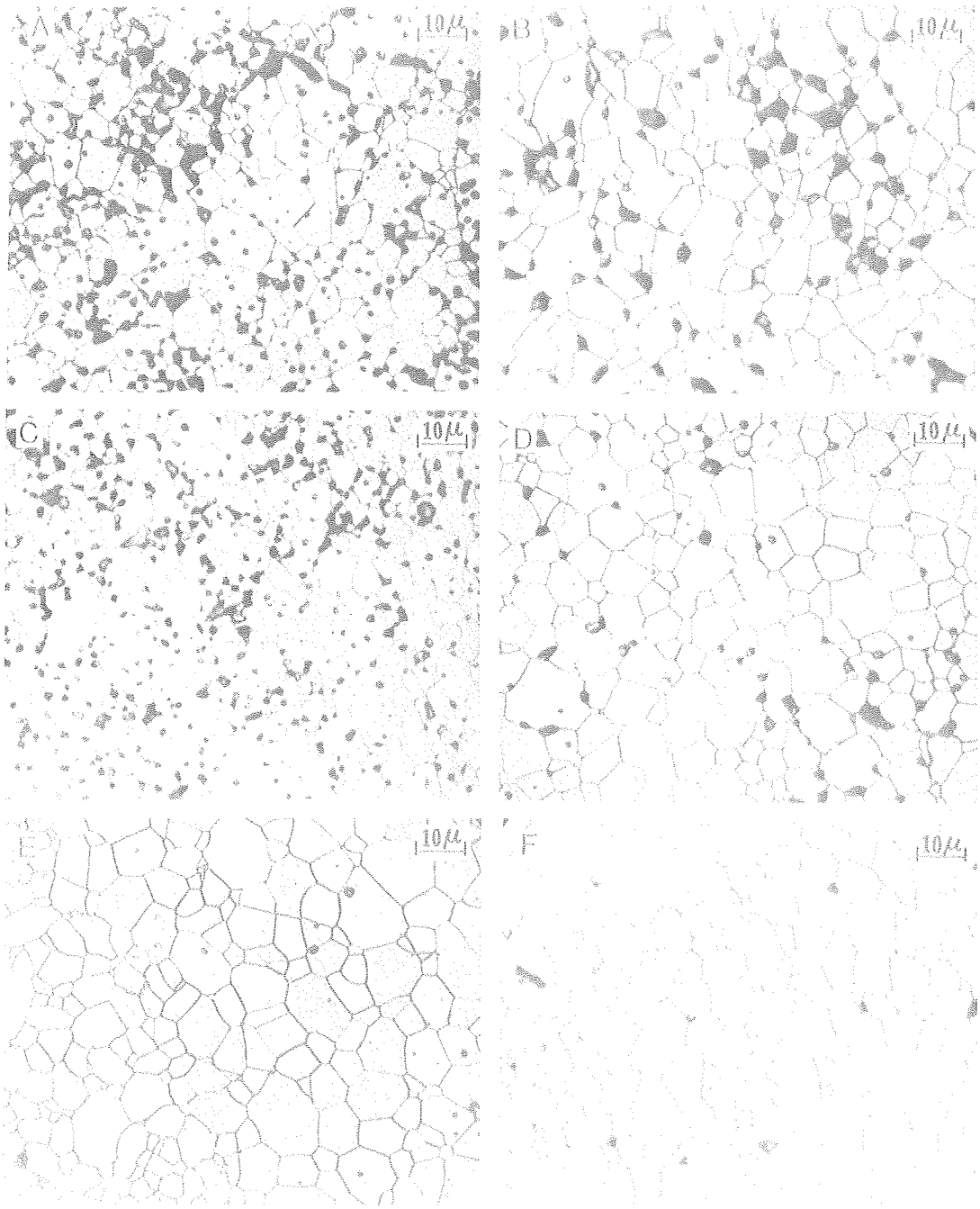

XBB768-7112

Fig. 50. Optical micrographs of MgO-doped Al_2O_3 compacts of different green densities after sintering at 1750°C in vacuum and H_2 for one hour. Vacuum: A (32%), C (38%), E 48%), and H_2: B (32%), D (38%), F (48%).

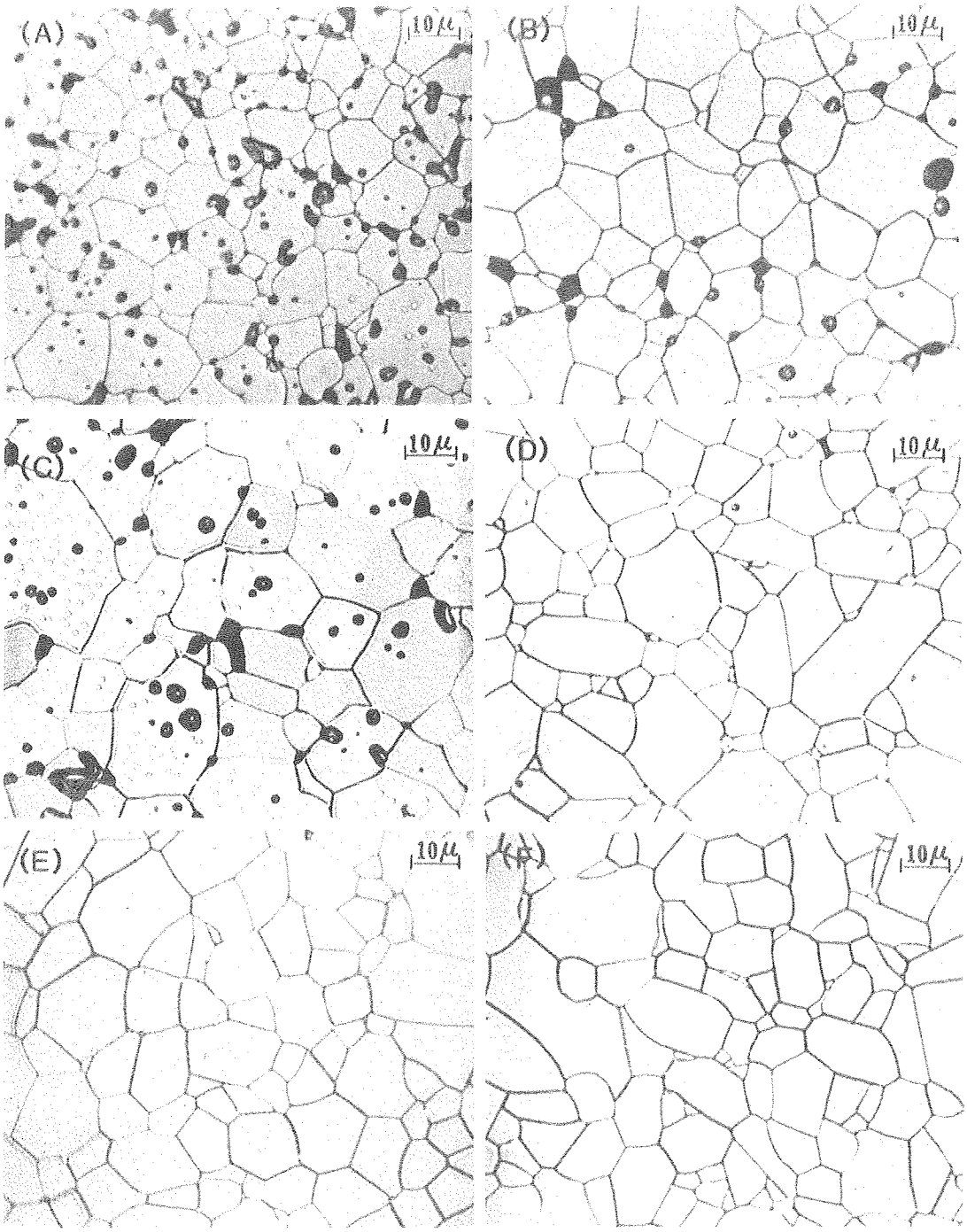

XBB768-7104

Fig. 51. Optical micrographs of MgO-doped Al_2O_3 compacts of different green densities after sintering at 1750°C in vacuum and H_2 for 10 hours. Vacuum: A (32%), C (38%), E (48%), and H_2: B (32%), d (38%), F (48%).

0 0 0 0 0 1 7 7 0 0 1 2 3 1 8 8

may change.

If the mobility of the pores is sufficient to permit them to keep up with the boundary (such as in the case of H_2 sintering), the pores will gradually become concentrated at boundary intersections and coalesce into large pores as grain growth proceeds (see Figs. 50B, D, and F, and Figs. 51 B, D, and F). If the pores are not mobile (such as in the case of vacuum sintering), the boundary will be either pinned by the pores or will pull away from the pores, depending on the relative values of the boundary driving force and the boundary mobility. When the compact is brought up rapidly to a high temperature, the large grain boundary volocity (due to the large mobility term) allows the boundary to overcome the forces exerted upon them by the small pores and, therefore, pore-grain boundary separation can occur (see Figs. 50A, B, and Figs. 51 A, B). In this situation the boundary may bend around the pores which results in the formation of a corrugated boundary. This effect can be seen in Fig. 52A and B. When the MgO dopant is absent, the velocity of the grain boundary also becomes large (due to the high driving force term) and, even at low temperatures, the boundaries can overcome the forces exerted upon them by the pores. This results in a pore-boundary separation and, if the compact density is not homogeneous, exaggerated grain growth will occur (see Fig. 45H). However, in the constant rate of heating, the gradual temperature increase does not allow the boundary migration velocity to become high enough to overcome the binding force of the immobile pores. These pores are normally larger than the average size since smaller pores have been eliminated.

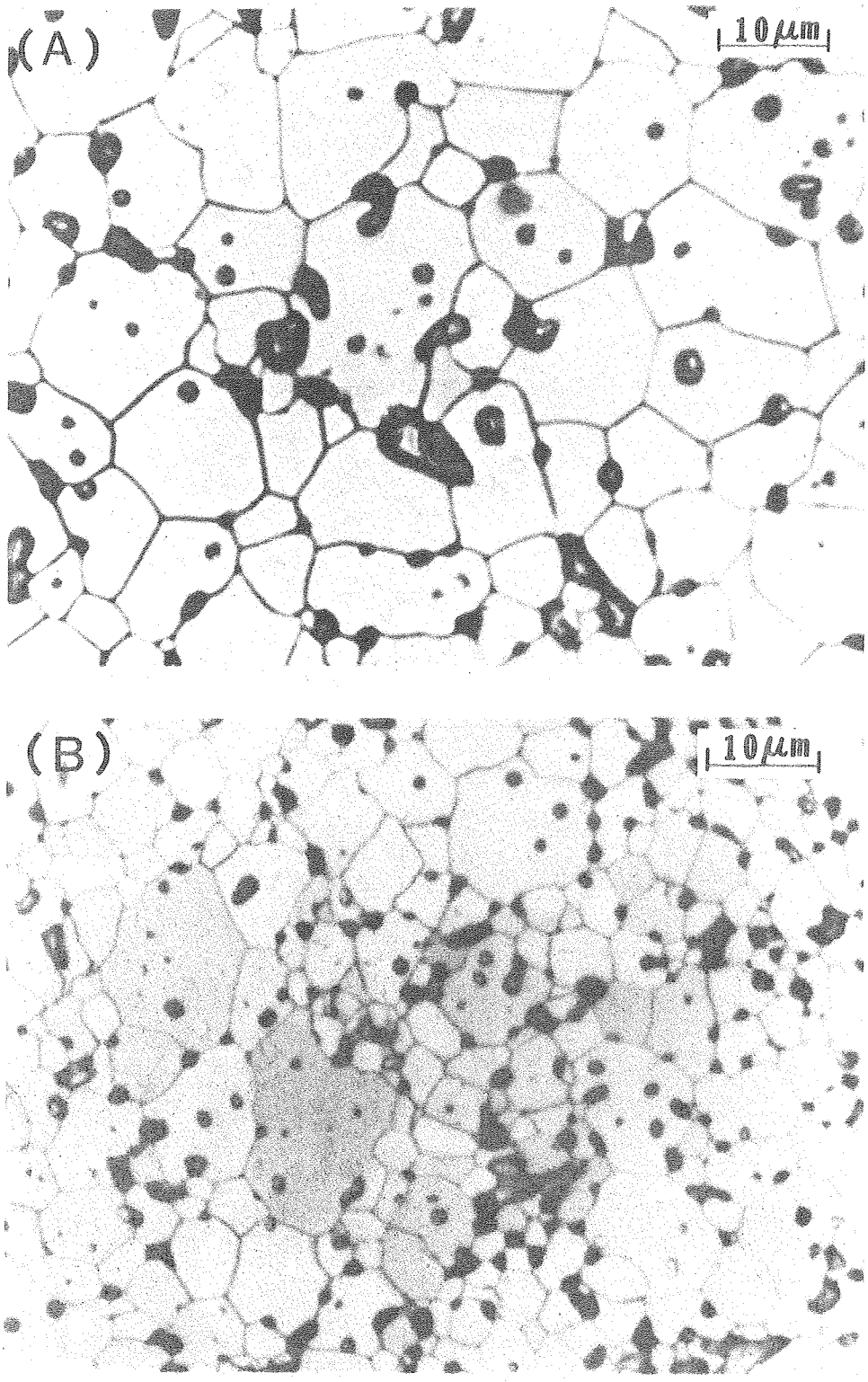

XBB768-7103

Fig. 52. Optical micrographs showing corrugated boundaries resulting from the pinning effect of pores for MgO-doped Al_2O_3 compacts of green densities of (A) 32% and (B) 38% after sintering at 1750°C in vacuum for 10 hours and one hours, respectively.

0000 0047700 4023899

Therefore, in vacuum sintering, the boundary is completely pinned by the pores and the grain size becomes limited by the pore size and the volume fraction of pores. As a result, there is an effect of green density on the sintered grain size. Since the boundary migration rate is controlled by the rate of shrinkage (i.e., the rate of the removal and the reduction in size of pore) it is not surprising that the activation energies for densification and grain growth are both 150 Kcal/mole.

Grain growth kinetics on compacts made of Union Carbide powders with different green densities were also studied. Since one heating rate was used, the rate law could not be determined. It is assumed that the grain growth kinetics of these compacts obey the same rate law which was determined for compacts made of G. E. powder.

Figure 53 gives the results for compacts with green densities of 32%, 38%, and 48% of theoretical in the form of $\ln G^{m-1} \frac{dG}{dt}$ vs. $\frac{1}{T}$ plot in which m = 3 is used. It shows that the grain growth kinetics above their respective critical density values obey the same rate law as determined from G. E. compacts and the activation energy is also the same value. By using m = 2.5 in equation (29), Fig. 54 gives the kinetics for the grain growth in compacts of densities below their respective critical density values. Again it shows the activation energy (94 Kcal/mole) is in good agreement with the value (95 Kcal/mole) determined for the G. E. compacts. The deviation in the intercept value shown in Figs. 53 and 54 is not readily explainable. It might be caused by the difference in the geometrical constant (as in equation (35)) for different green densities.

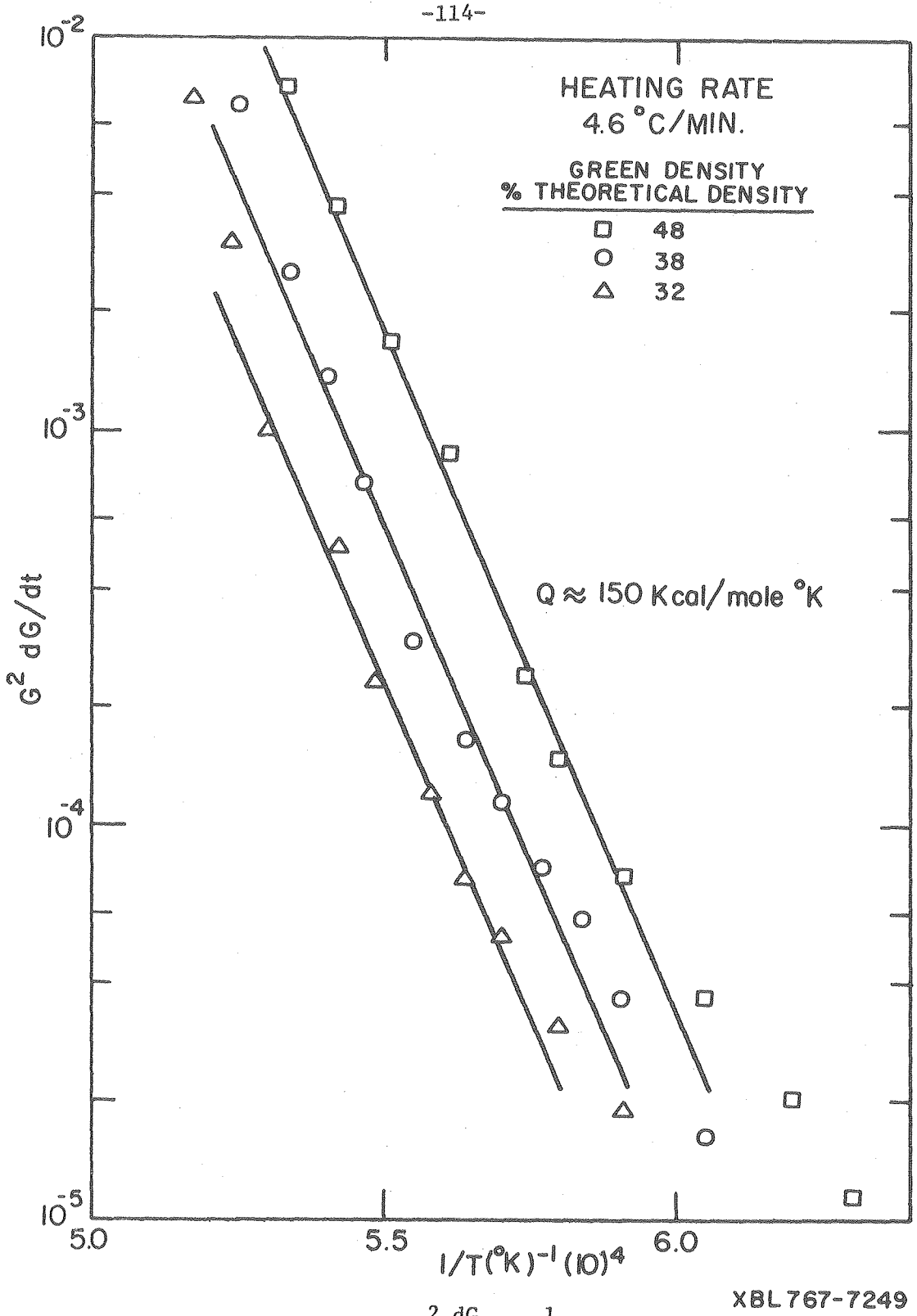

Fig. 53. Arrhenius plot of $G^2 \frac{dG}{dt}$ vs. $\frac{1}{T}$ for MgO-doped Union Carbide Al_2O_3 compacts of various green densities.

0 0 0 0 0 0 0 4 0 7 7 0 0 4 0 2 3 9 0 0

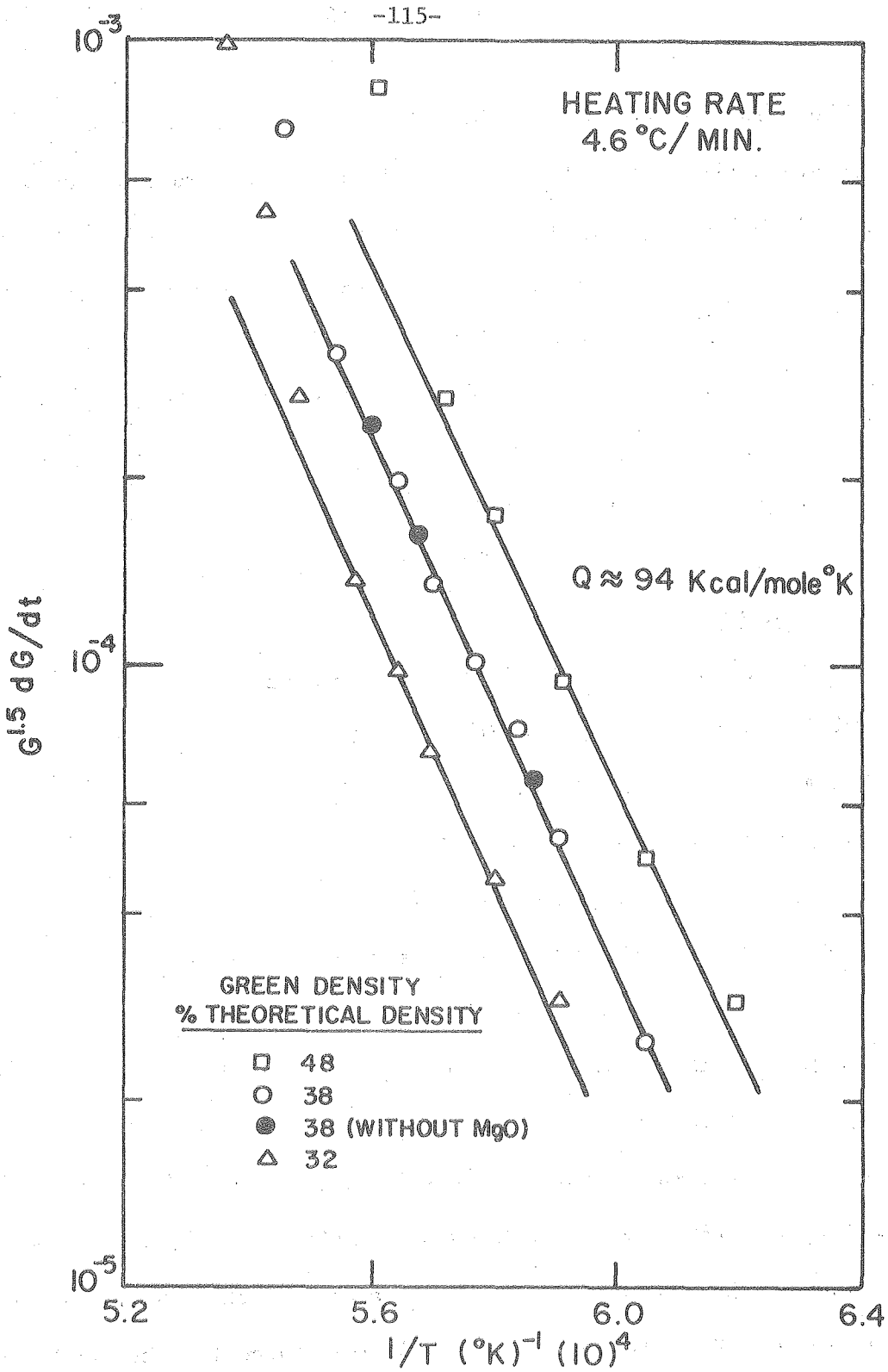

XBL 767-7247

Fig. 54. Arrhenius plot of $G^{1.5}\frac{dG}{dt}$ vs. $\frac{1}{T}$ for MgO-doped and undoped Union Carbide Al_2O_3 compacts of various green densities.

The values of m(2.5 and 3.2) found for the two stages of the grain growth are empirically based. The pinning effect must be considered for each grain boundary separately. Those boundaries having high curvature (very large or very small grains) will be free to move while those with low curvature will be pinned. Therefore, the grain size distribution, porosity distribution, pore shape, and pore size must all be considered before any growth rate law can be theoretically derived. Because the exact morphology of any real system will be quite complex, the development of a quantitative theory of the process is probably not possible.

3. Correlation

It has been found in the previous sections (IIIA and B) that the densification and the grain growth kinetics depend on the porosity of the compact after the attainment of the critical density. The rate of grain growth at a constant temperature is controlled by changes in volume fraction and size of pores (i.e. densification) and, in turn, the rate of these porosity changes is determined by the grain growth rate, since the rate of vacancy flow is, in part, governed by the grain size. The exact rate laws for both processes and their interdependence rely on the mathematical solution of the diffusion process. For densification, this involves a precise calculation of the time-dependent flow of atoms to pores from adjacent grain boundaries. Therefore, the pore-grain boundary geometry and the local values of the driving forces have to be known. For grain growth, the driving force for the boundary migration, and its dependence on the size and the shape of pores and grains, has to be calculated. Since geometrical changes involved in the sintering process are enormously complicated, the theoretical

0000 0047790-0259911

formulation of the rate laws in terms of specific values of processing parameters, such as the sintering time and temperature, is virtually impossible.

However, the microstructural features which govern the mass transport rate are fixed at a given density independent of heating rate and temperature used. As long as the green density of the compact is the same, there must be a certain relationship between the densification kinetics and grain growth kinetics in terms of porosity and grain size. This relationship above the critical density can be obtained from the empirical equations which were formulated in the preceding sections from the densification and the grain growth processes.

For densification $$\frac{d\rho}{dt} = \frac{K \exp(-\frac{Q}{RT})}{kT} p^n \qquad (19)$$

For grain growth $$G^{m-1} \frac{dG}{dt} = \frac{K' \exp(-\frac{Q}{RT})}{kT} \qquad (31)$$

It has been observed that the temperature dependences of these two processes are characterized by the same value of activation energy (150 Kcal/mole) after the critical density is reached. Thus, after combination of equations (19) and (31), and rearrangement, the relationship between grain size and porosity is:

$$G^m = K'' P^{1-n} \qquad (32)$$

This equation predicts a straight line with a slope of $\frac{1-n}{m}$ in a plot of ln G vs. lnP.

The value of n can be obtained by measuring the slopes of straight lines from a plot of $\ln T \frac{d\rho}{dt}$ vs. lnP at specific temperatures according to equation (19). Results generated from constant rate of heating and

isothermal treatment for G. E. compacts are presented in Fig. 55. The isothermal densification data were obtained by heating the compacts at a rate of 13°C/min to temperatures (1350, 1450, and 1550°C) and holding at respective temperatures for 100 minutes (see Fig. 56). Figure 55 shows, in accordance with the porosity change of the compact, the densification precess can be divided into three stages in addition to the initial density change from 40% to 50% of theoretical. The slope, n, of the straight lines for the fractional porosity range of 25 to 5% is determined to be 2.5. Using n = 2.5 and m = 3 in equation (32), a plot of lnG vs. lnP should give a straight line with a slope of - 1/2. Indeed, as seen in Fig. 57, the results for G. E. compacts shows a straight line with a slope of - 1/2. This grain size- porosity relationship explains the linear relationship observed between porosities of 30% and 5% in Fig. 41.

The time dependence of the densification process for compacts made of Union Carbide powder with various green densities and for MgO-doped and undoped compacts were obtained by plotting $\ln T \frac{d\rho}{dt} / \exp(-\frac{Q}{RT})$ vs. lnP according to equation (19), using Q = 150 Kcal/mole. The results are presented in Fig. 58 and 59. As shown in Fig. 58, a value of n = 3.25 was calculated for compacts of 32% and 38% green densities and n = 2.5 for the 48% green density compact. The difference in n values is attributed to variations in the pore phase with changing green density. Together with the value of m = 3, these n values should give slopes of -0.75 and -0.5 for the ln G vs. lnP plots for 32% and 38% green densities and 48% green density, respectively (Fig. 60).

0 0 0 0 4 7 0 0 2 9 2

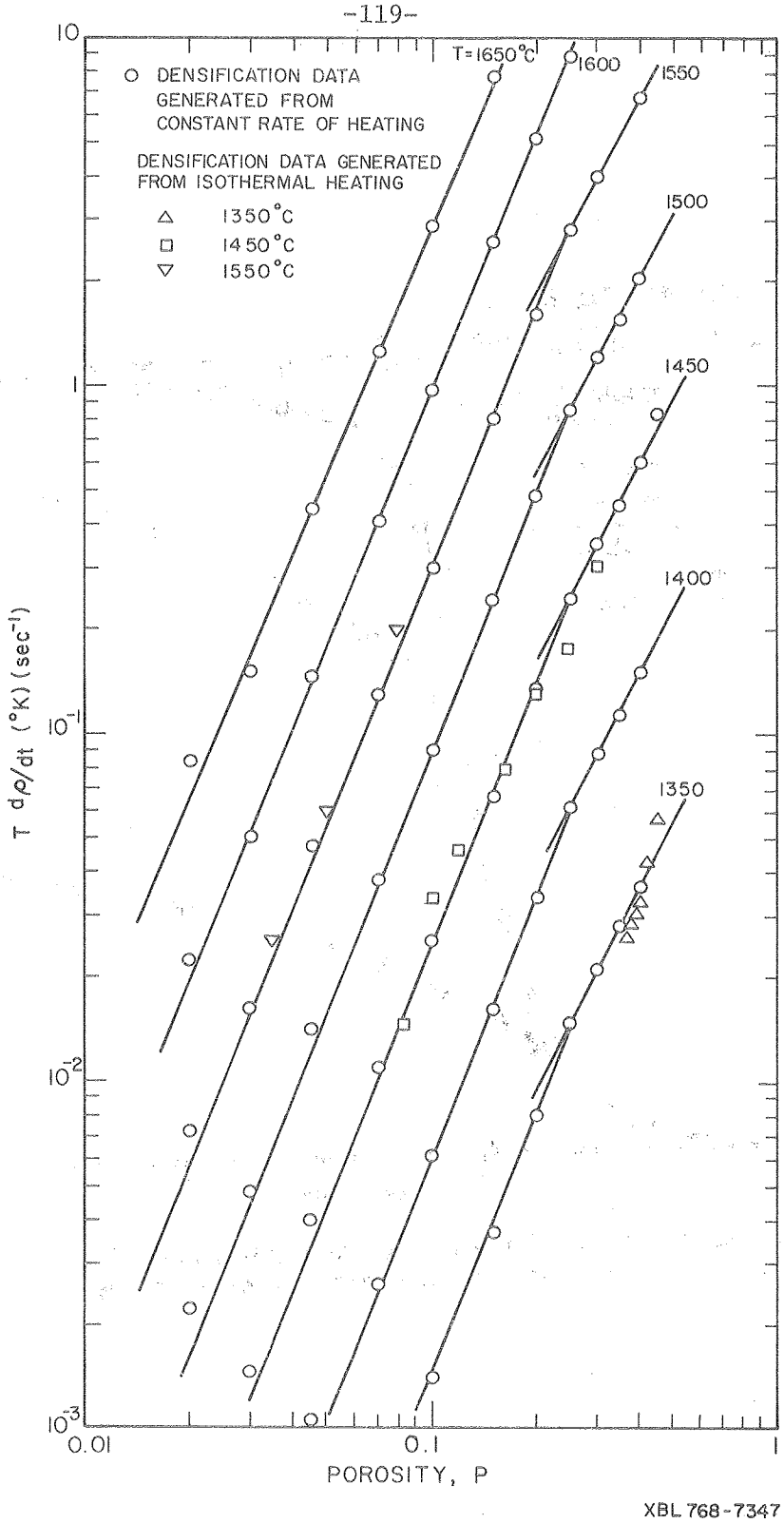

Fig. 55. Plot of ln $T\frac{d\rho}{dt}$ vs. lnP for MgO-doped G. E. Al_2O_3 compacts heated with various constant rates and isothermal treatments.

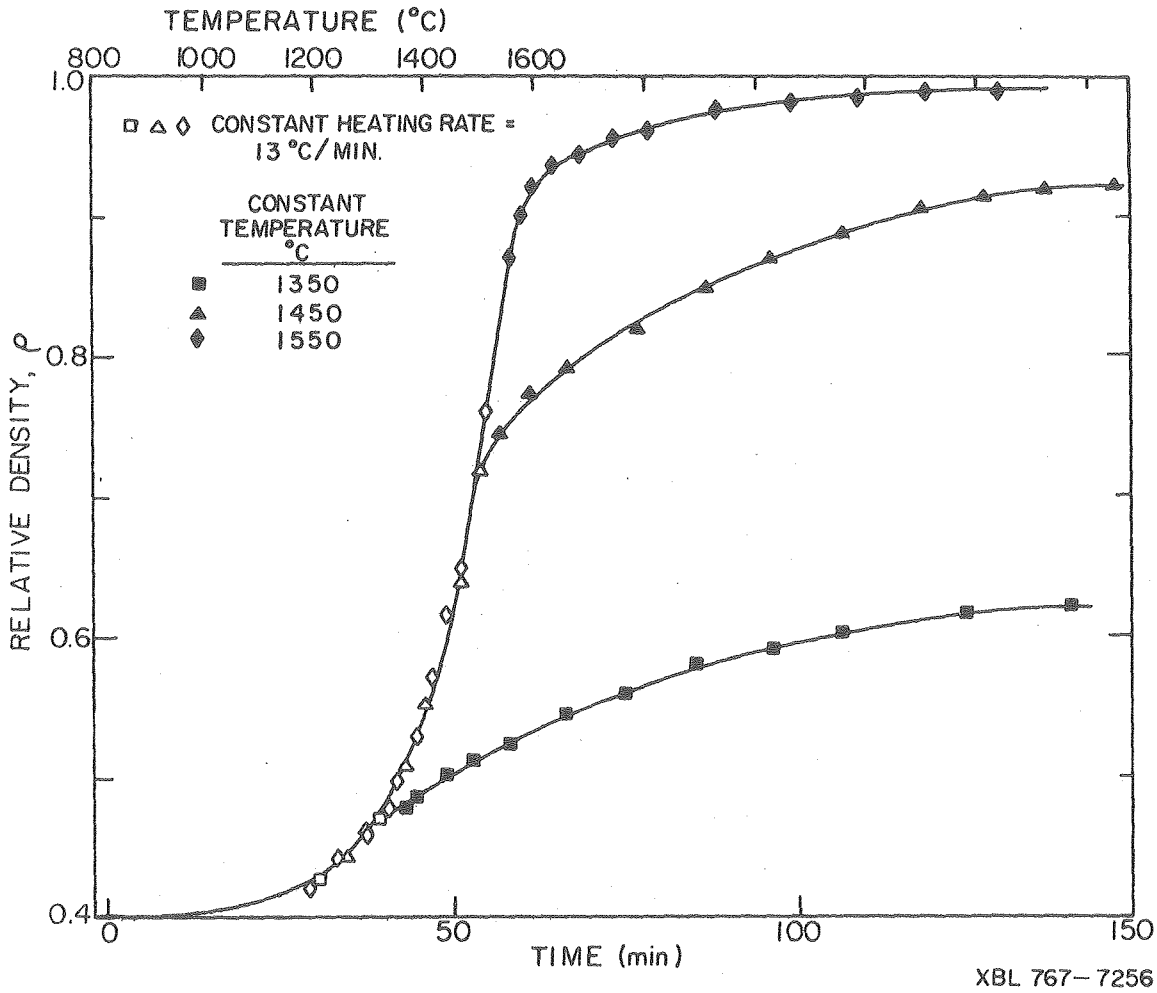

Fig. 56. Relative density vs. time for MgO-doped Al_2O_3 compacts heated at a constant rate to temperatures and held at respective temperatures.

0 0 0 0 4 7 0 0 3 0 3

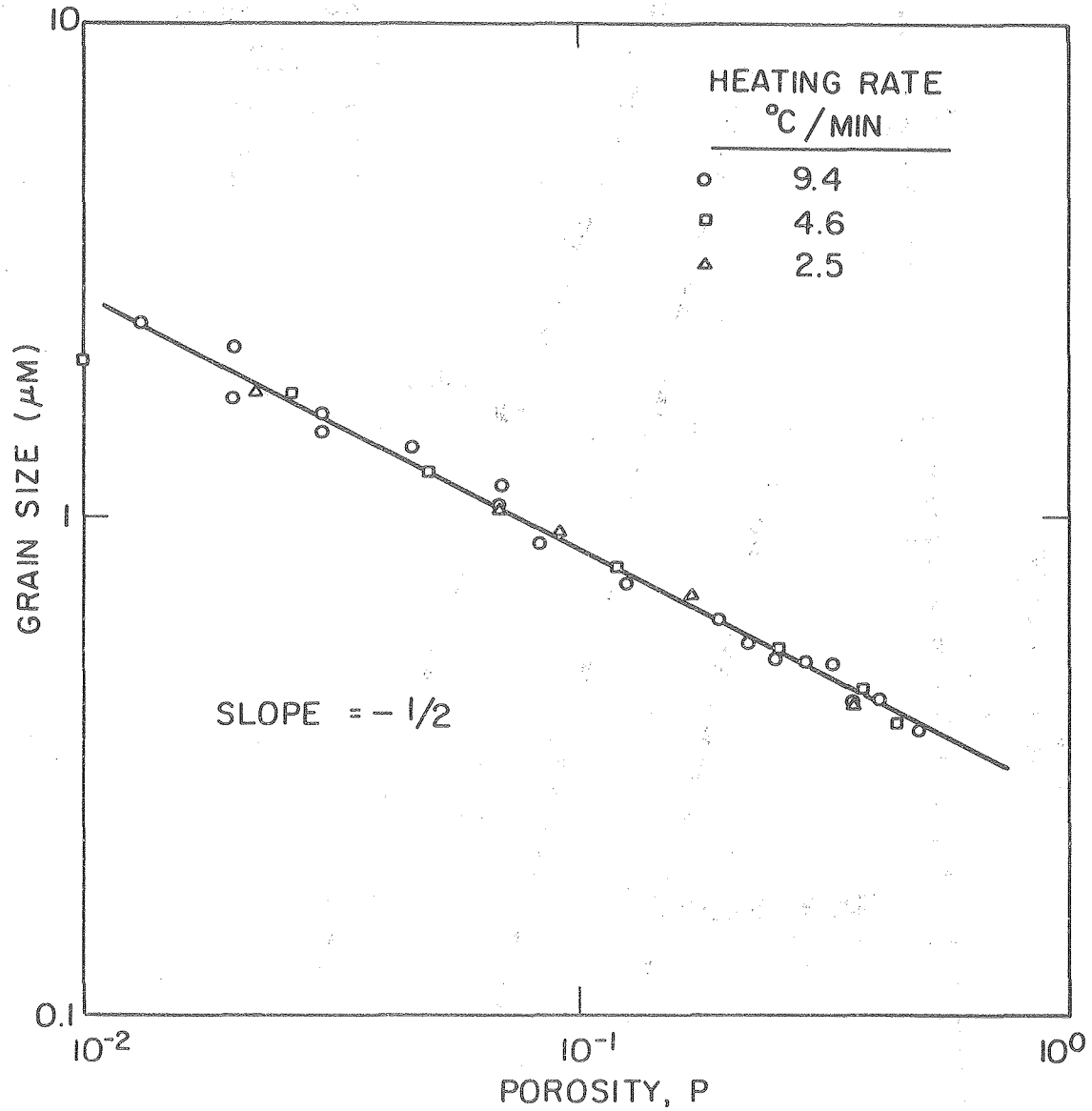

XBL 764-6778

Fig. 57. ln grain size vs. ln porosity for MgO-doped G. E. Al_2O_3 compacts of 40% green density heated at various rates.

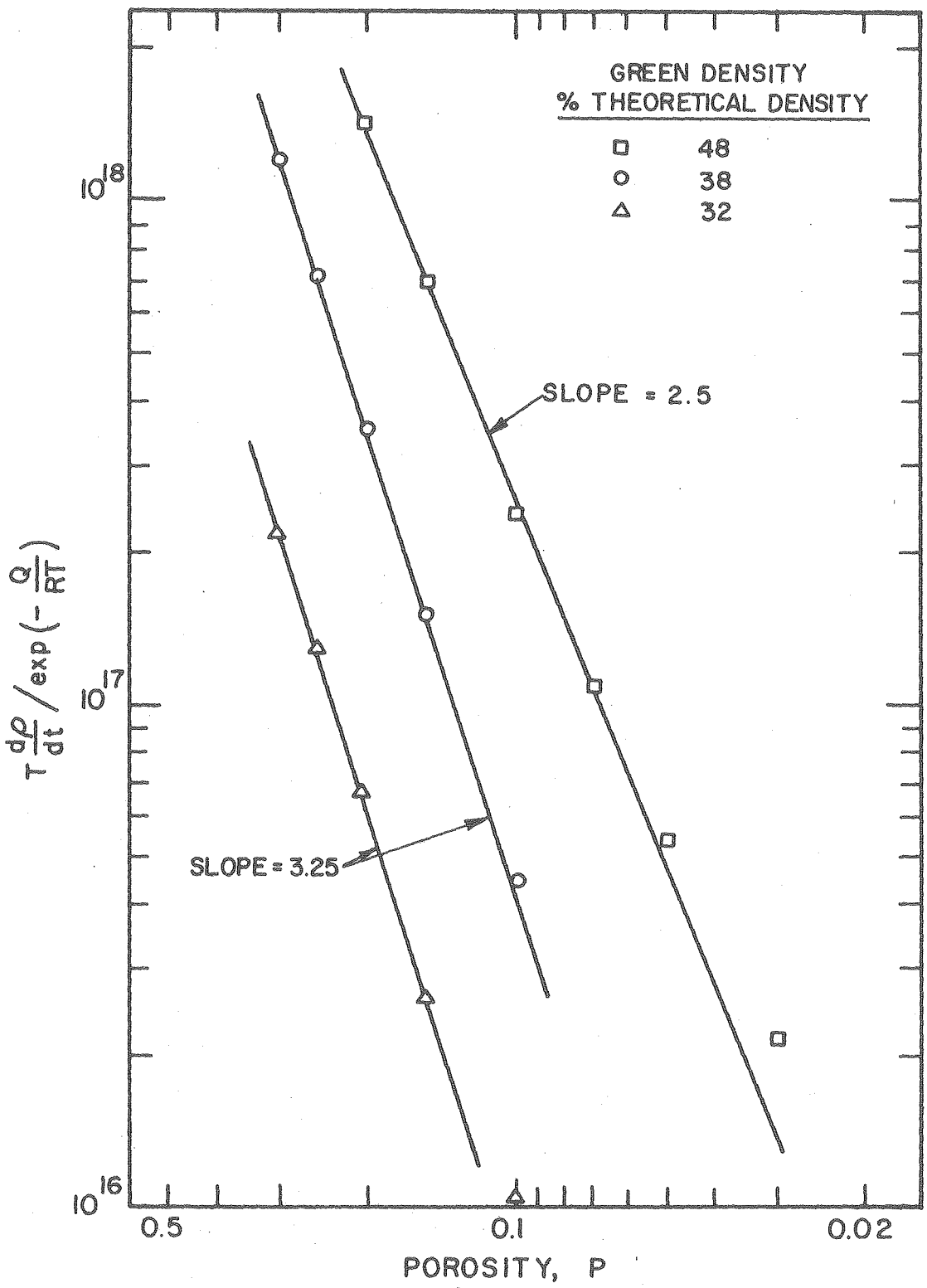

XBL 767-7255

Fig. 58. $\ln T \frac{d\rho}{dt} / \exp\left(-\frac{Q}{RT}\right)$ vs. lnP plot for MgO-doped Union Carbide Al_2O_3 compacts with various green densities heated at a rate of 4.6°C/min, and using Q = 150 kcal/mole.

0 0 0 0 4 7 7 0 0 2 3 9 4

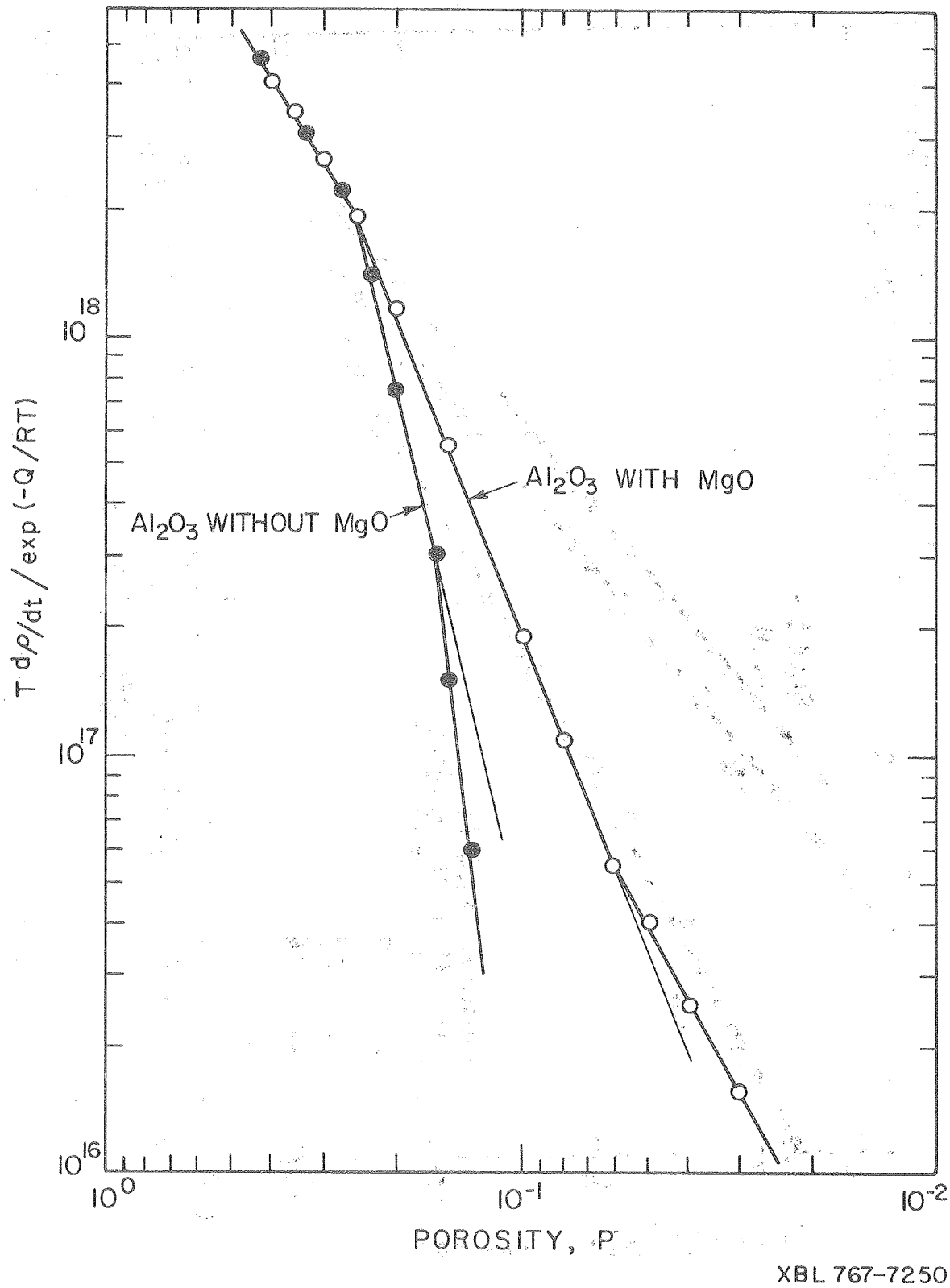

Fig. 59. Plot of $\ln T\frac{d\rho}{dt}/\exp\left(-\frac{Q}{RT}\right)$ vs. lnP for MgO-doped and undoped Al_2O_3 compacts by using Q equivalent to 150 kcal/mole.

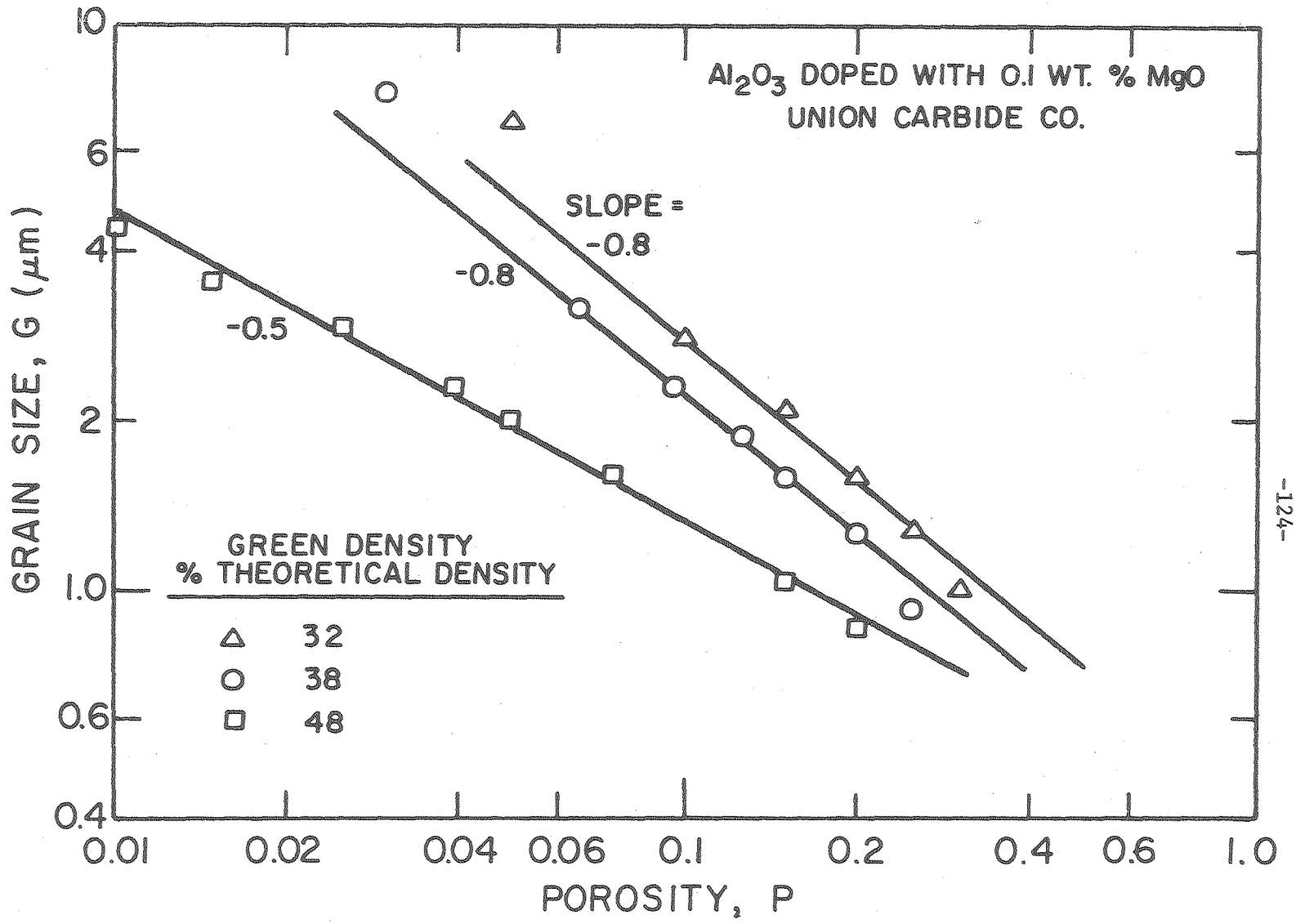

XBL 767-7245

Fig. 60. In grain size vs. ln porosity for MgO-doped Union Carbide Al_2O_3 compacts of various green densities heated at 4.6°C/min.

A more general form of equation (19) can be deduced by integrating at constant temperature. The equation is

$$\frac{1}{P^N} - \frac{1}{P_i^N} = K\left[\exp\left(-\frac{Q}{RT}\right)\right](t-t_i) \tag{33}$$

where P is the fractional porosity after sintering, t is the sintering time, P_i and t_i are the porosity and time at the beginning of each of the stages, T is the isothermal sintering temperature, N and K are constants which vary for each stage, and Q is the activation energy for the process. This equation has the same form as the one derived by Kuczynski[15] who used a statistical approach in which a distribution in size and location of pores was considered. However, the values of N determined in the present work do not agree with those predicted by Kuczynski's theory. A possible explanation for this discrepancy is the oversimplified assumption pertaining to the pore shape geometry (cylindrical and spherical) which can not properly represent the complex shape of pores as they exist in a real powder compact. In addition, the assumption that there is always Ostwald ripening accompanying pore shrinkage is not valid in the present investigation. The agreement in the form of both equations implies that the sintering kinetics is not only a function of grain size but also a function of porosity.

Equation (33) has been tested by using data of Coble,[17] and Jorgensen,[18] and Bruch.[22] Logarithmic plots of their data have been made and are shown in Figs. 61-64. Lines with slopes equal to one have been drawn for each set of data. This indicates that the time dependence of the sintering process as deduced from the present non-isothermal study can describe the behavior of the process under

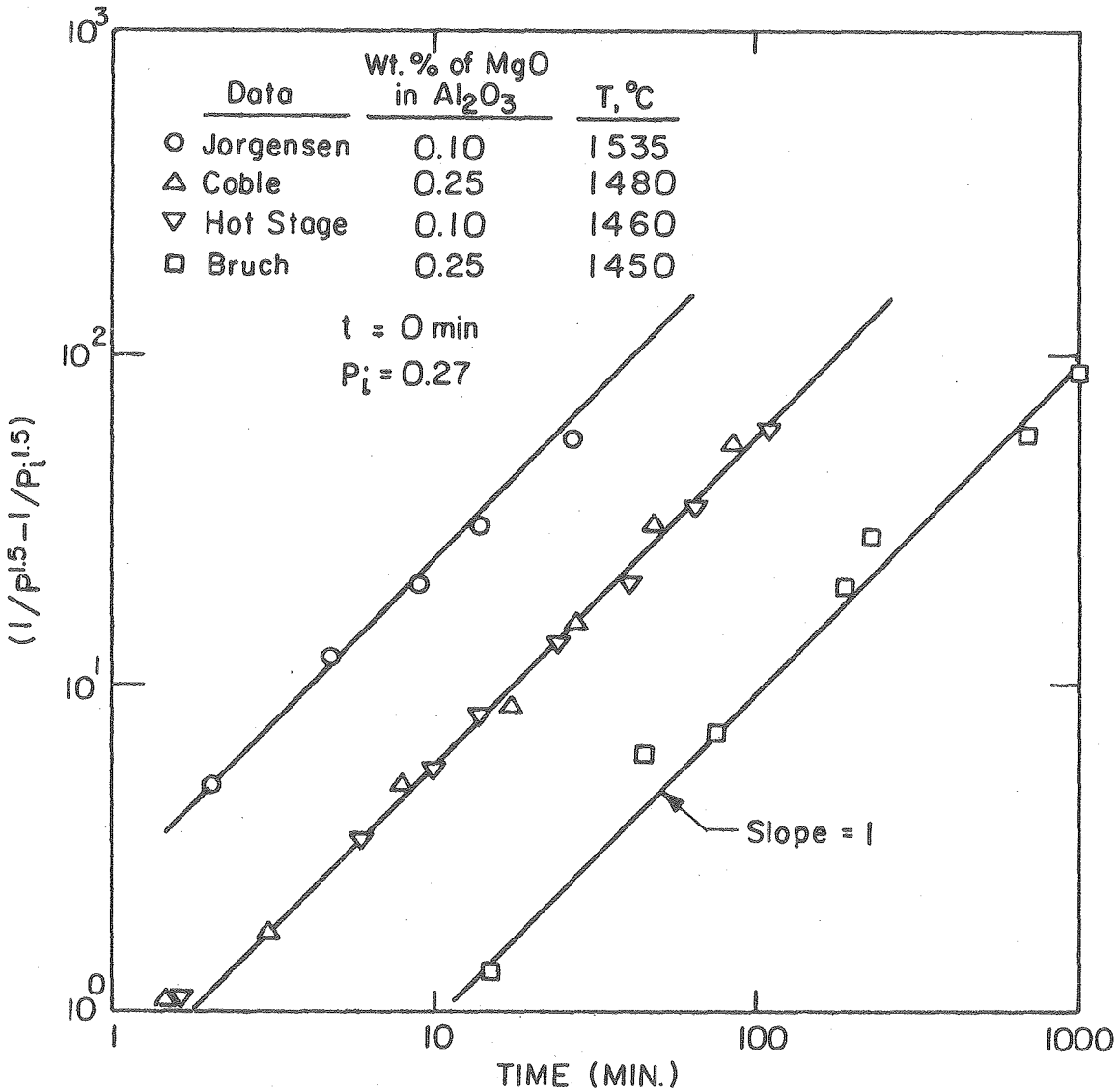

XBL 7511-7649

Fig. 61. Densification data by previous investigators for Linde-A Al_2O_3 with MgO dopant (Refs. 17, 18, and 22).

0 0 0 0 4 7 0 0 3 9 6

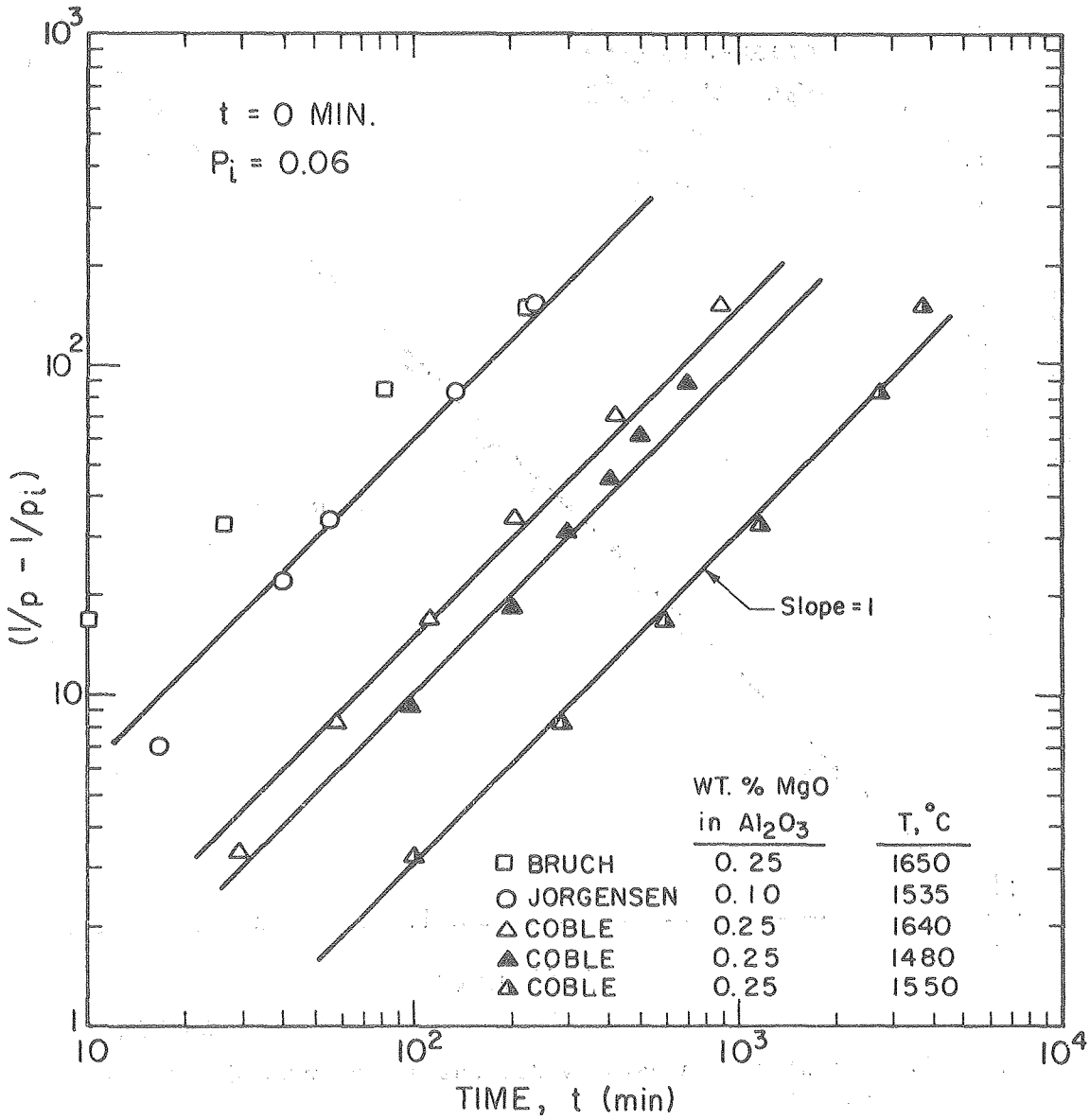

XBL 768-7342

Fig. 62. Densification data by previous investigators for Linde-A Al_2O_3 with MgO dopant (Ref. 17, 18, and 22).

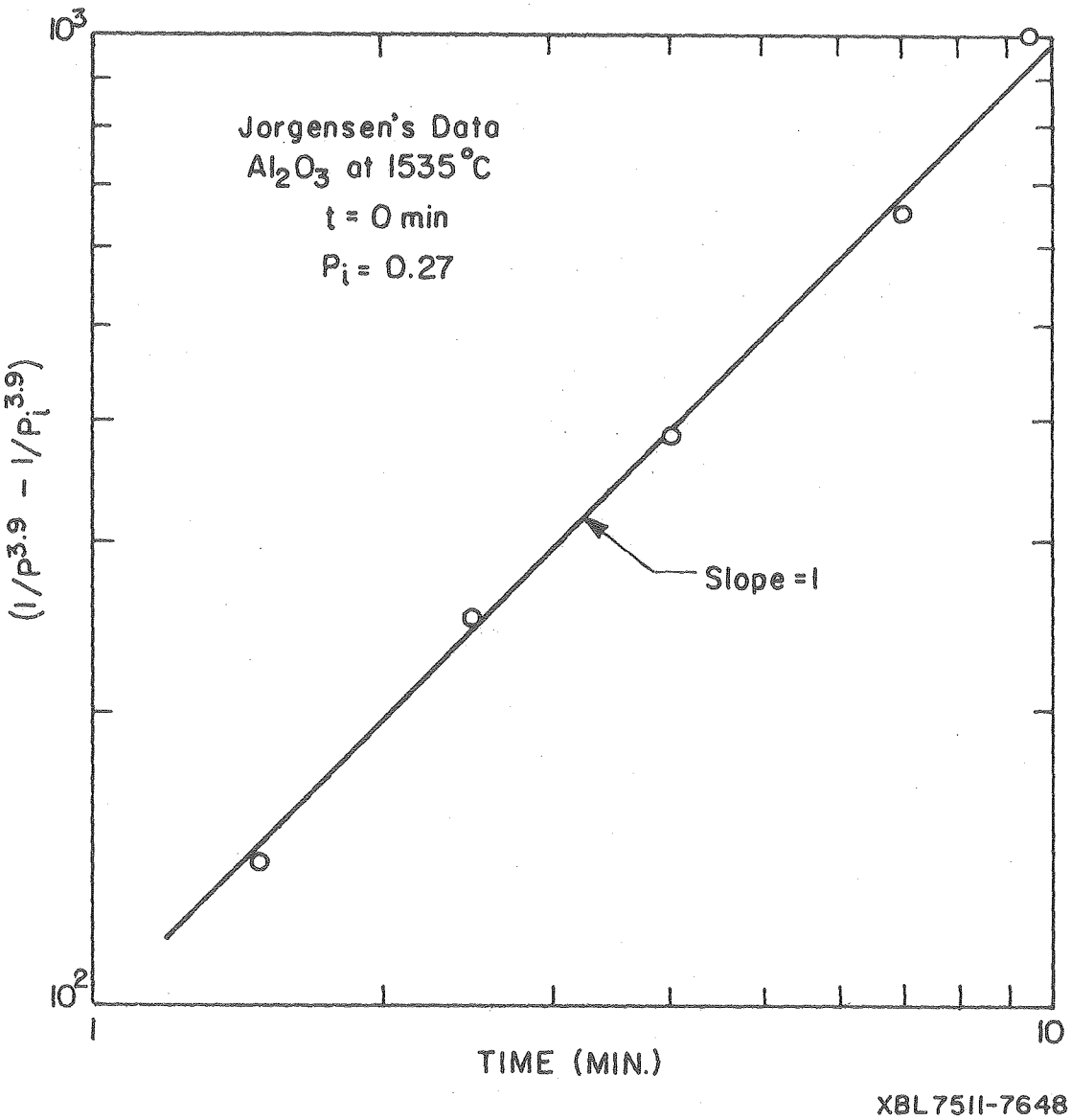

Fig. 63. Densification data by Jorgensen for undoped Linde-A Al_2O_3 (Ref. 18).

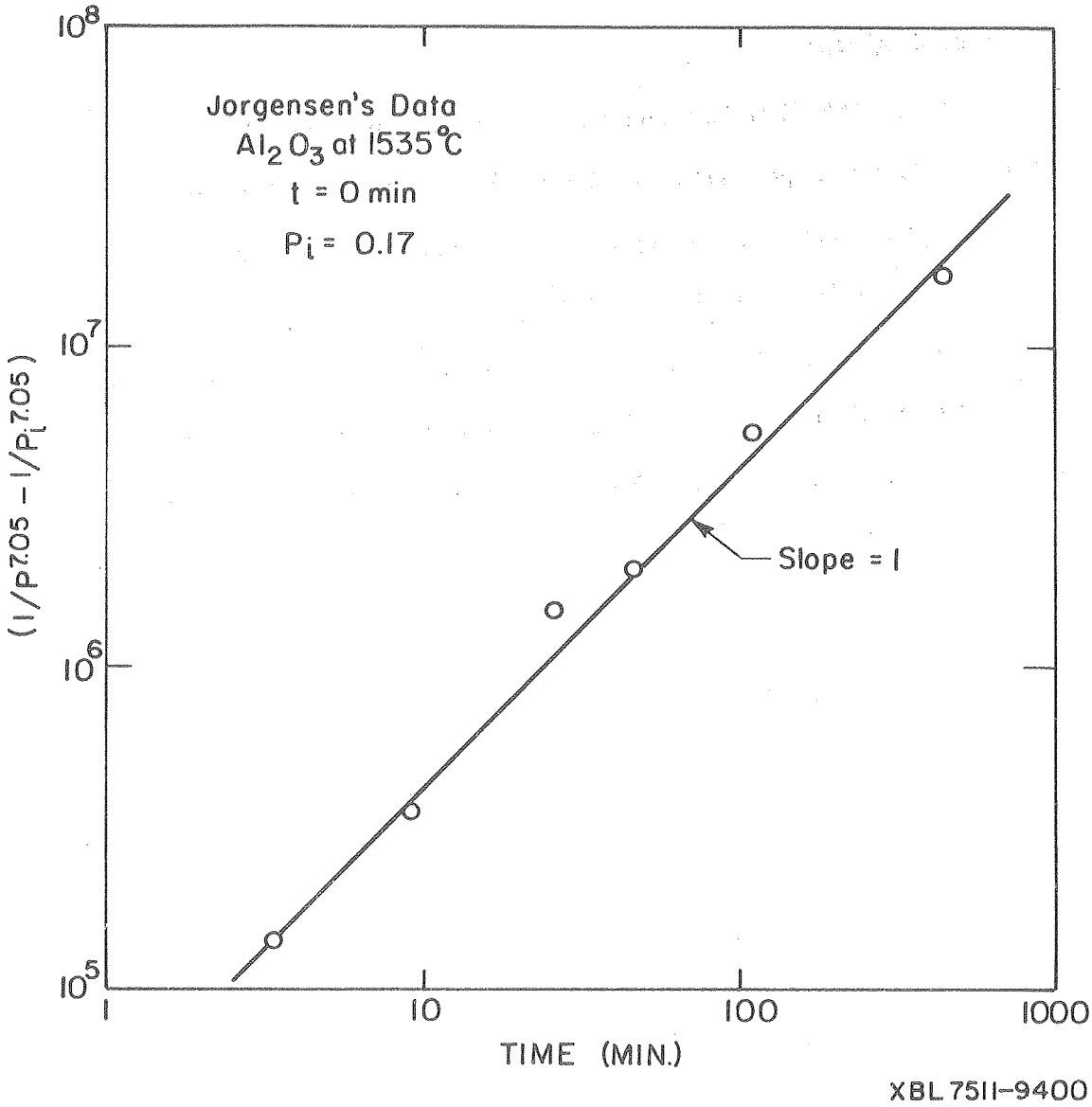

Fig. 64. Densification data by Jorgensen for undoped Linde-A Al_2O_3 (Ref. 18).

isothermal sintering.

Since equation (19) has the same form as equation (9), a relationship between porosity and heating rate at specific temperatures can then be deduced by following the same procedure as has been done for the derivation of equation (16). The results obtained from G. E. compacts with four heating rates are presented in Fig. 65 in the form of lnP vs. ln heating rate. The results indicate that the sintering process can be divided into four stages in accordance with the change of compact porosity.

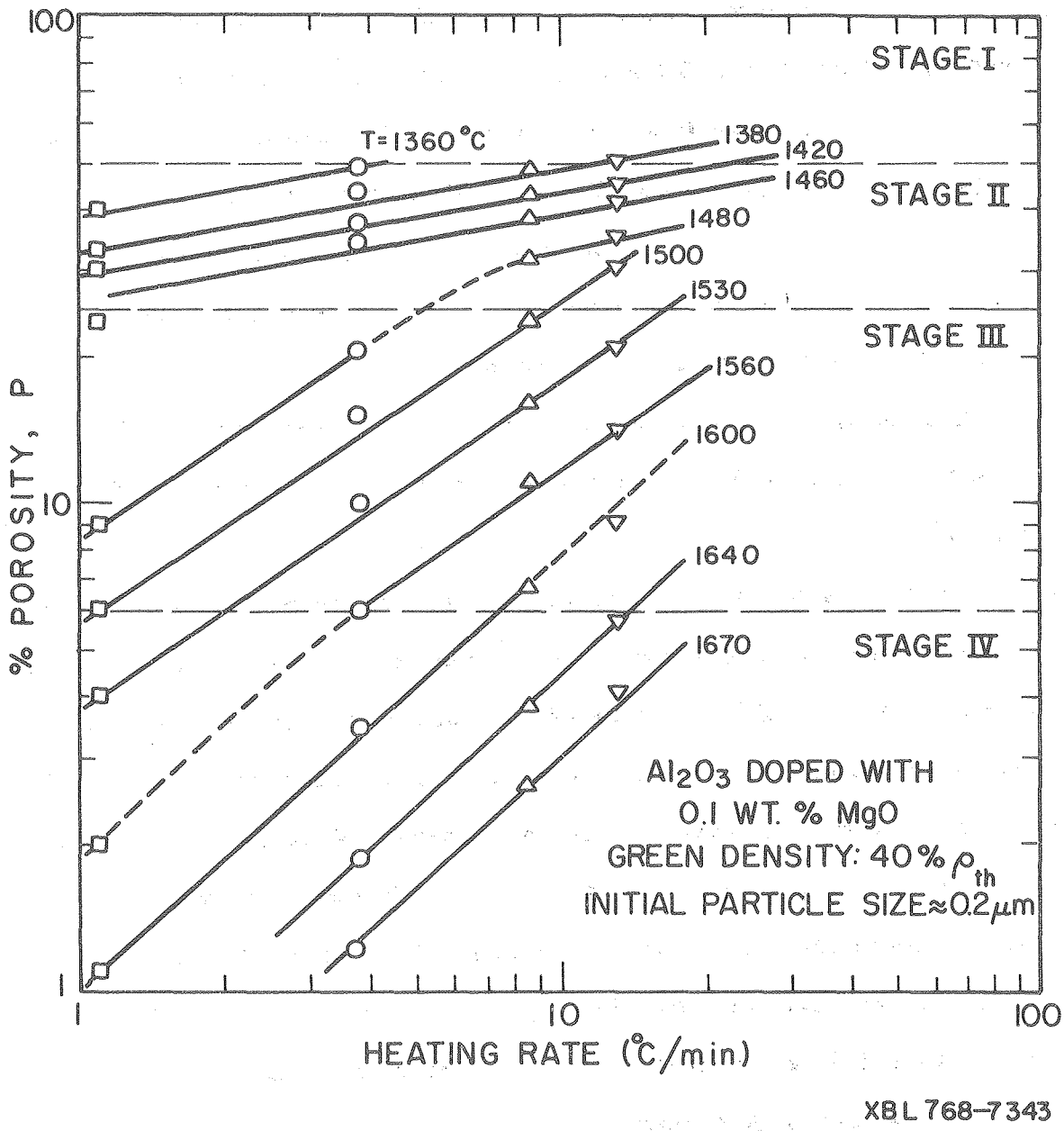

Fig. 65. Effect of heating rate on porosity change at a specific temperature for post initial stage CRH sintering of MgO-doped G. E. Al_2O_3 powder compacts.

IV. CONCLUSIONS

Utilizing a constant heating rate technique, densification and grain growth processes for Al_2O_3 powder compacts from the green state to nearly theoretical density have been studied. Analysis of the densification process for MgO-doped Al_2O_3 has shown that the process can be divided into four stages in accordance with the porosity changes.

In the initial stage, there is essentially no grain growth and the activation energy obtained for the sintering of submicron particles is about 90 Kcal/mole. Assuming the validity of current models, the kinetics of sintering in this stage is controlled by grain boundary diffusion.

The second stage is accompanied by grain growth which is linearly dependent on density. The activation energies for densification and grain growth are 150 Kcal/mole and 95 Kcal/mole, respectively. In this stage there is no effect of MgO dopant on either the densification or grain growth kinetics. The temperature dependence of the grain boundary mobility is characterized by boundary self-diffusion. This stage terminates at a critical density which is strongly dependent on the green density. Critical density, i.e., the density at which the maximum densification rate occurs, was correlated with a transition in the microstructural evolution.

In the third stage, the total number of pores decreases and the average pore size increases due to the elimination of small pores. In contrast to the previous stage, the densification rate is highly porosity (density) dependent as a result of the local variations in pore concentration. The densification kinetics and the grain growth kinetics were

0 0 0 0 4 7 0 0 3 0 0

found to be interdependent and characterized by the same activation energy (150 Kcal/mole).

In the final stage, the densification process is essentially the shrinkage of closed pores. Microstructural observations indicate there is no characteristic geometry for pore shapes and the densification rate is strongly dependent upon the particle packing in the green compact. During the last two stages, the grain growth rate is limited by the size and the volume fraction of pores in accordance with Zener's criterion. Coalescence of pores was not observed during sintering due to the low mobility of pores in a vacuum environment.

ACKNOWLEDGMENT

The author wishes to thank Professor Richard M. Fulrath for his continued support and advice through the course of this work. Additional appreciation is expressed to Michael D. Sacks and Professors Alan W. Searcy and Michael C. Williams for their helpful comments, suggestions, and editing of the thesis.

I am also grateful to Bob Powell and Daniel J. Miller for their interest and enlightening discussions. Further thanks are extended to Richard Lindberg, Gloria Pelatowski and Gay Brazil for their excellent assistance.

Finally, I would like to express my countless thanks to my wife, Aileen A. P. Wang for her encouragement and support.

This work was carried out under the auspices of the United States Energy Research and Development Administration through the Materials and Molecular Research Division of the Lawrence Berkeley Laboratory.

0 0 0 0 4 7 0 4 3 0 0

REFERENCES

1. J. Frenkel, "Viscous Flow of Crystalline Bodies Under the Action of Surface Tension," J. Phys. (USSR), 9[5], 385-91 (1945).

2. Pines, B., J. Tech. Phys., (USSR), 16, 737 (1946).

3. Kuczynski, G. C., "Self-Diffusion in Sintering Metal Powders," Trans. Amer. Inst. Min. (Metall.) Engrs., 185, 169 (1949).

4. Kingery, W. D. and Berg, M., "Study of the Initial Stages of Sintering Solids by Viscous Flow, Evaporation-Condensation, and Self-Diffusion," J. Appl. Phys., 26, 1205 (1955).

5. Alexander, B. H. and Balluffi, R. W., "Mechanism of Sintering of Copper," Acta Met. 5 [11] 666-77 (1957).

6. Kuczynski, G. C., "Measurement of Self-Diffusion of Silver Without Radioactive Tracers," J. Appl. Phys., 21, 632 (1950).

7. Coble, R. L., "Initial Sintering of Alumina and Hematite," J. Amer. Cer. Soc., 41, No. 2 (1958).

8. Johnson, D. L. and Cutler, I. B., "Diffusion Sintering: I, Initial Stage Sintering Models and Their Application to Shrinkage of Powder Compacts," J. Amer. Cer. Soc., 46, No. 11, 541-545 (1963).

9. Johnson, D. L., "New Method of Obtaining Volume, Grain-Boundary, and Surface Diffusion Coefficients from Sintering Data," J. Appl. Phys., 40, No. 1, 192-200 (1969).

10. Bannister, M. J., "Shape Sensitivity of Initial Sintering Equations," J. Amer. Cer. Soc., 51, No. 10, 548-553 (1968).

11. Coble, R. L., "Effects of Particle-Size Distribution in Initial-State Sintering," J. Am. Cer. Soc., 56 No. 9, 461-466 (1973).

12. Coble, R. L., "Sintering Crystalline Solids, I. Intermediate and

Final Stage Diffusion Models," J. Appl. Phys., 32, No. 5, 787-792 (1961).

13. Kingery, W. D. and Francois, B., "The Sintering of Crystalline Oxides, I. Interactions Between Grain Boundaries and Pores," in Sintering and Related Phenomena, Kuczynski, G. C., Hooten, N. A. and Gibbon, C. F., edg., Gordon and Breach, NY 471-498 (1967).

14. Coble, R. L., "Progress in Sintering Theory," Proc. 3rd Int. Conf. Sintering and Related Phenomena, (1973).

15. Kuczynski, G. C., "Pore Shrinkage and Ostward Ripening," in Sintering and Related Phenomena, Materials Sci. Res. [6], 217, Plenum Press, NY (1973).

16. Burke, J. E., "Role of Grain Boundaries in Sintering," J. Amer. Ceram. Soc., 40[3] 80-85 (1957).

17. Coble, R. L., "Sintering Crystalline Solids: II Experimental Test of Diffusion Models in Powder Compacts," J. Appl. Phys., 32[5] 793-99 (1961).

18. Jorgenson, P. J. and Westbrook, J. H., "Role of Solute Segregation at Grain Boundaries During Final-Stage Sintering of Alumina," J. Amer. Cer. Soc., 47, No. 7, 332-338 (1964).

19. Johnson, W. C. and Stein, D. F., "Additive and Impurity Distributions at Grain Boundaries in Sintered Alumina," J. Amer. Cer. Soc., 58, No. 11-12, 485-488 (1975).

20. Peelen, J. G. J., "Influence of MgO on the Evolution of the Microstructure of Alumina," in Sintering and Catalysis, ed. by Kuczynski, G. C. Plenum Press, NY, 443-453 (1976).

0 0 0 0 4 7 0 4 0 1
0 0 0 0 4 7 0 0 4 0 1

21. Jorgensen, P. J., Modification of Sintering Kinetics by Solute Segregation in Al_2O_3," J. Amer. Cer. Soc., 48[4], 207-210 (1965).

22. Bruch, C. A., "Sintering Kinetics for the High Density Alumina Process," Bull. Am. Ceram. Soc., 41[12] 799-806 (1962).

23. Greskovich, C. and Lay, K. W., "Grain Growth in Very Porous Al_2O_3 Compacts," J. Amer. Cer. Soc., 55, No. 3, 142-146 (1972).

24. Turnbull, D., "Theory of Grain-Boundary Migration Rates," Trans. AIME 191[8], 661-65 (1951).

25. Greenwood, G. W., "Growth of Dispersed Precipitates in Solution," Acta Met., 4[3] 243-48 (1956).

26. Cahn, J. W., "Impurity-Drage Effect in Grain Boundary Motion," Acta Met., 10[9] 780-98 (1962).

27. Nichols, F. A., "Theory of Grain Growth in Porous Compacts," J. Appl. Phys., 37[13], 4599-4602 (1966).

28. Brook, R. J., "Pores and Grain Growth Kinetics," J. Amer. Cer. Soc., 52[6] 339-40 (1969).

29. Kingery, W. D., and Francois, B., "Grain Growth in Porous Compacts," J. Amer. Cer. Soc., 48[10] 546-47 (1965).

30. Fulrath, R. M., "Scanning Electron Microscopy to 1600°C," Proceedings of the Fifth Annual Scanning Electron Microscope Symposium (ITT Research Institute, 17, 1972).

31. Shumaker, C. B. and Fulrath, R. M., "Initial Stages of Sintering of Copper and Nickel," Materials Science Research Vol. 6, Sintering and Related Phenomena, 191-199, Plenum Press, NY (1973).

32. Miller, D. J., "SEM Hot-Stage Sintering of UO_2," M.S. Thesis, LBL-5173, University of California, June, 1976.

33. Froshauer, L. and Fulrath, R. M., "Direct Observation of Liquid-Liquid Phase Sintering in the System Iron-Copper," J. Met. Sci., 10, 2146-2155 (1975).

34. Froshauer, L. and Fulrath, R. M., "Direct Observation of Liquid-Phase Sintering in the System Tungsten Carbide-Cobalt," J. Mat. Sci. 11, 142-149 (1976).

35. Nielsen, T. H. and Leipold, M. H., "Thermal Expansion in Air of Ceramic Oxides to 2200°C," J. Am. Cer. Soc., 46[8] 381-387 (1963).

36. Fullman, R. L., "Measurement of Particle Sizes in Opaque Bodies," Trans. AIME, 197[3] 447-52 (1953).

37. Johnson, D. W. and Nitti, D. J. and Berrin, L., "High Purity Reactive Alumina Powders: II, Particle Size and Agglomeration Study," Bull, Am. Ceram. Soc., 51[12] 896-900 (1972).

38. Iwase, Takada and Hayashi, "Sintering and Crystallographic Characteristic of Very Fine Oxide Particles Produced by Calcination of Salts," in Powder Metallurgy.

39. Whittemore, O. J. and Sipe, J. J., "Pore Growth During the Initial Stages of Sintering Ceramics," Pwd. Tech., 9, No. 4, 159-164 (1947).

40. Greskovich, C., and Woods, K. N., "Fabrication of Transparent ThO_2 Doped Y_2O_3," Bull. Am. Ceram. Soc., 52[5] 473-478 (1973).

41. Young, W. S. and Cutler, I. B., "Initial Sintering with Constant Rates of Heating," J. Am. Cer. Soc., Vol. 53[12], 659-663 (1970).

42. Woolfrey, J. L. and Bannister, M. J., "Nonisothermal Techniques for Studying Initial-Stage Sintering," J. Am. Ceram. Soc., Vol. 55[8], 390-394 (1972).

43. Cutler, I. B., "Sintering of Glass Powders During Constant Rates of Heating," J. Amer. Ceram. Soc., 52[1] 14-17 (1969).

44. Young, S., Rasmussen, S. and Cutler, I. B.; pp. 185-202 in Ultra-fine Grain Ceramics. Edited by J. J. Burke, N. L. Reed, and Volker Weiss. Syracuse University Press, Syracuse, NY (1970).

45. Johnson, D. L., "Interpretation of Sintering Kinetics Data," in Sintering and Related Phenomena, Materials Sc. Res. [6], 363-368, Plenum Press, NY (1973).

46. Johnson, D. L. and Berrin, L.; pp. 445-69 in Sintering and Related Phenomena. Edited by G. C. Kuczynski, N. A. Hooton, and C. F. Gibbon. Gordon and Breach, Science Publishers, Inc., NY (1967).

47. Paladino, A. E. and Kingery, W. D., "Aluminum Ion Diffusion in Aluminum Oxide," J. Chem. Phys., 37[5] 957-62 (1962).

48. Oishi, Y. and Kingery, W. D., "Self-Diffusion of Oxygen in Single-Crystal and Polycrystalline Aluminum Oxide," ibid., 33[2] 480-86 (1960).

49. Chang, C., "Diffusion-Controlled Deformation and Shape Changes in Nonfissionable Ceramics," Proceedings of the Conference on "Nuclear Applications of Nonfissionable Ceramics," pp. 101-112, edited by Alvin Boltax and J. H. Handwerk, Washington, DC (1966).

50. Coble, R. L. and Gupta, T. K., "Intermediate Stage Sintering," in Sintering and Related Phenomena, Kuczynski, G. C., Hooton, N. A. and Gibbon, C. F. eds., Gordon and Breach, NY 423-443 (1967).

51. Burke, J. E., "Grain Growth," in Ceramic Microstructures, ed. R. M. Fulrath and J. A. Pask, Wiley, NY p. 681 (1968).

52. Beck, P. A. Towers, J. and Mauly, W. D., "Grain Growth in 70-30

Brass," Trans. AIME, 175, 162 (1948).

53. Lücke, K. and Detert, K. , "A Quantitative Theory of Grain-Boundary Motion and Recrystallization in Metals in the Presence of Impurities," Acta Met. [5], 628, (1957).

54. Gordon, P., "Rationalization of Data on Grain Boundary Migration in Zone-Refined Metals as Influenced by Dissolved Impurities," Trans. AIME [227], 699-705 (1963).

55. Beck, P. A., Holzworth, M. L. and Sperry, P. R., "Effect of Dispersed Phase on Grain Growth in Al-Mn Alloys," Trans. AIME[180], 163 (1949).

56. Zener, C., "Private Communication to C. S. Smith," Trans. AIME[175] 15 (1948).

57. Hillert, M., "On Theory of Normal and Abnormal Grain Growth," Acta Met.[13] 227 (1965).

58. Roy, S. K. and Coble, R. L., "Solubility of Magnesia, Titania, and Magnesium Titanate in Aluminum Oxide," J. Amer. Cer. Soc., Vol. No. 1, pp. 1-6 (1968).

59. Drolet, J. P., and Galibois, A., "Altering the Time Cycle of Heat Treatment by Preannealing Prior to Grain Growth," Met. Trans.[2], pp. 53-64 (1971).

60. Mullin, W. W., "Magnetically Induced Grain-Boundary Motion in Bismuth," Acta Met. [4] 421, (1956).

61. Vandernreer, R. A., "Transient Effect in Grain-Boundary Migration During Recrystallization in Aluminum," Acta Met.,[15] 447-458 (1967).